FREQUENCY-DOMAIN SYSTEM IDENTIFICATION OF F-16 LONGITUDINAL DYNAMICS

A THESIS SUBMITTED TO
THE GRADUATE SCHOOL OF NATURAL AND APPLIED SCIENCES
OF
MIDDLE EAST TECHNICAL UNIVERSITY

BY

EGE ERGAZI

IN PARTIAL FULFILLMENT OF THE REQUIREMENTS
FOR
THE DEGREE OF MASTER OF SCIENCE
IN
AEROSPACE ENGINEERING

MARCH 2022

Approval of the thesis:

FREQUENCY-DOMAIN SYSTEM IDENTIFICATION OF F-16 LONGITUDINAL DYNAMICS

submitted by **EGE ERGAZI** in partial fulfillment of the requirements for the degree of **Master of Science in Aerospace Engineering Department, Middle East Technical University** by,

Prof. Dr. Halil Kalıpçılar
Dean, Graduate School of **Natural and Applied Sciences** _____

Prof. Dr. Serkan Özgen
Head of Department, **Aerospace Engineering** _____

Assoc. Prof. Dr. İlkay Yavrucuk
Supervisor, **Aerospace Engineering, METU** _____

Dr. Gönenç Gürsoy
Co-supervisor, **Aerotim Engineering LLC** _____

Examining Committee Members:

Prof. Dr. Ozan Tekinalp
Aerospace Engineering, METU _____

Assoc. Prof. Dr. İlkay Yavrucuk
Aerospace Engineering, METU _____

Prof. Dr. Kemal Leblebicioğlu
Electrical and Electronics Engineering, METU _____

Assist. Prof. Dr. Ali Türker Kutay
Aerospace Engineering, METU _____

Assist. Prof. Dr. Yakup Özkazanç
Electrical and Electronics Engineering, Hacettepe University _____

Date: 10.03.2022

I hereby declare that all information in this document has been obtained and presented in accordance with academic rules and ethical conduct. I also declare that, as required by these rules and conduct, I have fully cited and referenced all material and results that are not original to this work.

Name, Surname: Ege Ergazi

Signature :

ABSTRACT

FREQUENCY-DOMAIN SYSTEM IDENTIFICATION OF F-16 LONGITUDINAL DYNAMICS

Ergazi, Ege
M.S., Department of Aerospace Engineering
Supervisor: Assoc. Prof. Dr. İlkay Yavrucuk
Co-Supervisor: Dr. Gönenç Gürsoy

March 2022, 103 pages

The longitudinal dynamics of F-16 aircraft in a level trim, unaccelerated flight are identified using frequency-domain system identification techniques. The nonlinear system is excited by sine sweep elevator input, and angle of attack and pitch rate responses are collected. Detrending and windowing are applied to time-domain data and are converted to the frequency-domain by applying Fast Fourier Transform (FFT). The smooth spectral estimates are found from the transformed data, allowing frequency responses and coherence to be calculated. Under the guidance of coherence, transfer functions are estimated to the frequency response data. Then, nondimensional derivatives are extracted from these identified transfer functions. Finally, the identified model is verified in the time domain.

Keywords: frequency-domain system identification, fighter aircraft, transfer function modelling, frequency-response estimation, short-period approximation, parameter estimation

ÖZ

F-16 BOYLAMSAL DİNAMİKLERİNİN FREKANS UZAYINDA SİSTEM TANIMLAMASI

Ergazi, Ege
Yüksek Lisans, Havacılık ve Uzay Mühendisliği Bölümü
Tez Yöneticisi: Doç. Dr. İlkay Yavrucuk
Ortak Tez Yöneticisi: Dr. Gönenç Gürsoy

Mart 2022 , 103 sayfa

Denge halindeki F-16 hava aracının boylamsal dinamiklerinin frekans uzayı yöntemleri kullanılarak sistem tanımlaması yapılmıştır. Doğrusal olmayan sistem irtifa dümenine verilen sinüs tarama girdisiyle uyarılarak hücum açısı ve yunuslama momenti cevapları toplanmıştır. Zaman uzayındaki veriler yönsemeyi giderme ve pencereleme teknikleri uygulandıktan sonra hızlı Fourier dönüşümü (FFT) uygulanarak frekans uzayına çevrilmiştir. Dönüştürülmüş verilerden pürüzsüz spektral tahminler elde edilmesiyle birlikte frekans cevapları ve uyumluluk değerleri hesaplanmıştır. Uyumluluk değerleri rehberliğinde, frekans cevaplarına uygun aktarma fonksiyonları tahmin edilmiştir. Tanımlanmış aktarma fonksiyonlarından boyutsuz aerodinamik türevler çekilmiştir. Son olarak, zaman uzayında tanımlanmış sistemin doğrulaması yapılmıştır.

Anahtar Kelimeler: Frekans uzayında sistem tanımlaması, savaş uçağı, transfer fonksiyon modelleme, frekans cevabı tahmini, kısa-periyot yaklaşımı, parametre tahmini

To my parents

Gülçin & Ümit

In the memory of my dear uncle Timuçin and my lovely grandfather Mustafa

ACKNOWLEDGMENTS

I want to express my most profound gratitude to my supervisor, Assoc. Prof. Dr. İlkay Yavrucuk for his guidance, support and patience. What I have learned from his unique, serene and vivid attitude towards engineering and life is priceless. I want to extend my sincere appreciation to my co-advisor, Dr. Gönenç Gürsoy, for his helpful feedbacks and strongly supporting me with his knowledge and experience. I would like to thank the committee members for their valuable comments that significantly enhanced this study. Not to mention how thankful I am to Assoc. Prof. Dr. Utku Kanoğlu for always seeing me through.

I am grateful to Dr. Mark Tischler for his comments that have carried my horizon to another level and for his belief in my work, which highly motivated me. I am very thankful to Turkish Aerospace for paving the way, and all the memories belonging here have a special place in me.

I cannot thank enough Assoc. Prof. Dr. Tayfun Çimen, I would not complete this work without his guidance and tolerance. I also would like to thank Derya Gürak for supporting me, especially while presenting my thesis. Special thanks to Orkun Şimşek, who introduced system identification during my internship.

Thank you a million times from the bottom of my heart, my colleague, Metin Kuş, for your unlimited support, enormous contributions and esteemed comments. I gratefully acknowledge Uğur Karaman for opening his doors fully to help me while I struggle with the model. Warmest thanks to Dr. Murat Millidere and Sinem Uluocak for sharing their experience and knowledge with me. Additionally, I acknowledge my colleagues Hakan, Evren, Cihan, Elif, Nilsu and Berkan for supporting me during the presentation specifically and all the team members of FDSC. I am so happy to be a part of this fantastic team.

I am out of words to describe how glad and lucky I feel to have such a family. Diye-bileceğim tek şey, iyi ki varsınız.

Finally, thank you to those who taught me anything and to simply everyone who somehow has been a part of the journey.

TABLE OF CONTENTS

LIST OF TABLES

TABLES

LIST OF FIGURES

FIGURES

LIST OF ABBREVIATIONS

CIFER	Comprehensive Identification from FrEquency Responses
DFT	Discrete-Fourier Transformation
FFT	Fast-Fourier Transformation
LEF	Leading Edge Flap
LOES	Low-Order Equivalent System
SCAS	Stability and Control Augmentation System
A	Amplitude
b	Wing Span
$\overline{c}$	Wing Mean Aerodynamic Chord
$C_{m,ds}$	Deep Stall Non-dimensional Pitching Moment
H_e	Engine Angular Momentum
I_X, I_Y, I_Z	Moments of Inertia about X, Y and Z body axes
I_{XZ}	Product of Inertia with respect to X and Z body axes
n_z	Linear Acceleration Component along the z-body axis
q	Body Pitch Rate
$\overline{q}$	Dynamic Pressure
S	Wing Area
s	Laplace Variable
t	Time
T_{min}, T_{max}	Minimum and Maximum Time Period of Interest
T_{rec}	Time Duration of Flight-Test Record
T_{win}	Window Length
v	Velocity Component along y-body axis
V_{T_e}	Trim Airspeed

V_{TAS}	True Airspeed
α	Angle of Attack
δ_{e_c}	Elevator Command Input Signal to Elevator Actuator
δ_e	Elevator Deflection
δ_{sweep}	Frequency Sweep Input
η_{δ_e}	Elevator Effectiveness Factor
ω	Angular Frequency
$\omega_{min}, \omega_{max}$	Minimum and Maximum Frequency of Interest (and of Excitation)
ω_n	Natural Frequency
θ	Pitch Attitude
ζ	Damping Ratio

CHAPTER 1

INTRODUCTION

1.1 Background and Motivation

Building reliable mathematical models that represent real-life dynamics is one of the most fundamental and sometimes challenging engineering applications. Mathematical models are a set of mathematical equations in which the relationship between inputs and outputs of a physical system is embedded. Usually, the structure of the mathematical models is based upon physical laws and the model parameters which characterise the system are obtained from observations or experiments [10].

"System identification is the art and science of building mathematical models of dynamic systems from observed input–output data. It can be seen as the interface between the real world of applications and the mathematical world of control theory and model abstractions."[11]. An example of an input-output system is an aircraft, and mathematical models that represent its dynamics can be obtained via system identification techniques. Aircraft system identification is an efficient and powerful process to extract an accurate aircraft model based on the measured response to specific control inputs.

Extraction of such mathematical models by system identification also helps to

- Understand the cause–effect relationship that underlies a physical phenomenon,
- Investigate system performance and characteristics,
- Verify wind-tunnel and analytical predictions,
- Develop high-fidelity aerodynamic databases for flight simulators,

- Support flight envelope expansion during prototype testing,
- Derive high-fidelity and high-bandwidth models for in-flight simulators,
- Design flight control laws, including stability augmentation systems,
- Analyse handling qualities specification compliance [4].

Application of system identification process can be carried out in both domains, time-domain or frequency-domain. While numerous works are related to time-domain methodologies in the literature, such as [4, 12], frequency-domain methods are employed in this study. The frequency-domain analysis offers particular advantages, such as holding physical insight of frequency content, direct applicability to control system design methods and flying qualities modelling, handling the noisy data and lower dimensionality for model parameter estimation. In addition, unlike time-domain methods, frequency-domain methods are risk-free of numerical divergence as integration is not required [13, 14]. On the other hand, frequency-domain methods have their drawbacks, too. For instance, transforming time-domain data to the frequency-domain is likely to suffer from leakage errors. In other words, noise-free time-domain data may yield noisy frequency response function measurements [15]. The solutions for such difficulties are already available in the literature broadly [9, 16] and are easy to implement, as done in this thesis.

Frequency-domain methods based on spectral estimation [17, 18], output error [19, 20], and equation error [19, 21] have been applied to flight-test data for aircraft system identification. Spectral estimation covers frequency response estimation, which is performed in this study. Frequency response is the ratio of the response (e.g., pitch rate) per unit of control input (e.g., elevator) over a frequency range. Frequency response is obtained by applying Fourier transform and windowing methods to flight-test data in the time domain. Then, a parametric model to estimated frequency-response model based on empirical data is fitted where parameters, such as stability and control derivatives, can be extracted [17]. The main steps of identifying a dynamic aircraft model can be summarised as follows:

- Step 1: Apply frequency sweeps to single inputs
- Step 2: Estimate frequency responses using spectral techniques
- Step 3: Identify model parameters by fitting a postulated model to Bode plots using nonlinear optimisation. [22]

The product of the system identification in the frequency-domain is a describing function. Describing functions can be defined as linear approximations that best represent the nonlinear responses. Therefore, since the product is an approximation, verifying it in the time domain is essential after identifying the model using frequency-domain techniques. The verification can be done by exciting the system again with different inputs such as steps or doublets. Most of the time, the identified models accurately predict movements with high amplitude, which makes them more than small-perturbation models, and the power of this method comes from this. Identifying the models at a couple of conditions with a common model structure might be sufficient to mimic the existing system for flight-control design. Combining the identified models with physics-based simulations can yield the high-fidelity full-flight envelope predictions needed for flight control and handling-qualities applications [17].

1.2 Related Work

The first paragraph of this section is about the early history of system identification and is adapted from [4] and [17]. Recognising the importance of obtaining aircraft parameters from flight records as early as the 1920s, the works in this field grew steadily up to the fifties. In 1945, Cornell Aeronautical Laboratory conducted frequency-response identification based on flight-test data, the earliest reported research in this field. Another significant research about dynamic stability and control during this early period is available in [23], and Greenberg [24] surveyed methods in 1951 regarding the determination of aerodynamic derivatives from dynamic flight data. Yet another essential work done in the early fifties belongs to Shinbrot [25], who had introduced the response curve fitting. This is an equivalent approach to the output-error method used nowadays. However, at the time being, Shinbrot's work was found impracticable due to the inadequacy of the required digital computational power. To sum

up the techniques of the 1940s to early 1960s, they mainly were frequency response methods. Since only a few coefficients or only simple motions can be identified due to limited estimation capability, frequency response methods also suffered inadequate computational power.

Despite being computationally demanding, frequency-domain methods dominated the theory and system identification practice in the control engineering field until the sixties. From the end of the sixties, due to the increased interest in time-domain methods, the identification in control literature is mainly shifted to time-domain methods in the eighties. On the other hand, significantly improved computing capabilities in the sixties and the FFT algorithm's development led to great success in frequency-response identification, while the fundamental system identification theory remained essentially unchanged [17, 26].

Åström and Bohlin [27] the implemented maximum-likelihood method on a digital computer and applied it to an industrial plant represented by difference equations in 1965. This can be considered the start of modern system identification, according to Jategonkar [4]. Klein [28] also studied the same method in the frequency domain later, followed by many flight-vehicle programs, including the X-31 fixed wing application [29]. In addition, the roots of the transfer function fitting algorithm used in this work which is presented in[30], belong to this era.

Coming to the seventies, Twisdale and Ashurst [31] developed early comprehensive work in frequency-response analysis for system identification. Having many applications on, such as simulators, manned-powered aircraft and research aircraft, Systems Technology, Inc. (STI) was the pioneer in the frequency-response aircraft system identification using prescribed frequency-sweep inputs. Concordantly, lower-order transfer-function modelling gained momentum with the development of an updated handling qualities specification for military fixed-wing aircraft [32], as stated in [17].

Since the eighties, many works have contributed to the understanding and development of frequency-domain methods in system identification. Practical insights on dealing with non-periodic data and the utilisation of frequency domain data to estimate continuous-time models are the most important ones, according to Ljung [33]. More about modern practical aspects can be found in Morelli and Grauer's work [14].

For many years, various authors have worked on similar applications to the system identification procedure followed in this study, as given in the references [18, 22, 34, 35].

Finally, having solid theory and countless applications in many fields, system identification in the aviation industry has become easier to apply with the help of dedicated software tools such as SIDPAC (System IDentification Programs for AirCraft), CIFER(Comprehensive Identification from Frequency Responses) and FITLAB.

1.3 Thesis Objective and Outline

This chapter intends to introduce the system identification concept with a brief history and highlight the motivation by clarifying the goal of this work. The ultimate goal of this thesis is to identify the short-period mode of F-16 aircraft using frequency-domain methods. The system identification procedure explained by Tischler and Remple [17] is utilised to reach this goal. The design of the thesis is composed of two main parts. First, the aircraft model and the method are introduced, and then the application is given in detail with the results.

Chapter 2 is dedicated to the aircraft model and the behaviour of the aerodynamic database. General specifications of F-16, including the actuators, are presented. Then, the details about the aerodynamic database are introduced, and observations on bare-airframe dynamics are shared. Having intuition about bare-airframe dynamics prior to identification is helpful to understand the problem and is essential for successful identification. The entire procedure followed in this study is explained in detail from start to finish in Chapter 3. The chapter begins with input design and elaborates on the post-processing of the collected time history. The frequency-response and transfer function estimations are presented with the Fourier transform. Then, from the identified transfer functions, parameter estimation is performed. The identified model is tested in the time domain as the last step. The application of the procedure explained in Chapter 3 is given in Chapter 4. It is repeated in the specified flight envelope, and consistent results are obtained. Concluding remarks are made in Chapter 5, and possible ways to improve the identification method and algorithm are discussed.

CHAPTER 2

AIRCRAFT MODEL

2.1 Aircraft and Actuator Model Specifications

The nonlinear F-16 simulation model in MATLAB - Simulink environment provided by [2] is used in this study. Specifications of the F-16 aircraft used in the simulation are given in Table 2.1. The aerodynamic database of the simulation is the aerodynamic data obtained from the wind tunnel. 16% scale model of the F-16 with the landing gear retracted and without external stores is used in the wind tunnel test. The experiments are conducted for Mach numbers lower than 0.6 and out of ground effect [1, 3]. The same model of F-16 is also used by Morelli and Grauer [14] to demonstrate some practical aspects of frequency-domain system identification techniques.

Table 2.1: F-16 Aircraft Model Specifications [1]

Property	Value
Weight	91188 N
Ix	12875 kg m^2
Iy	75674 kg m^2
Iz	85552 kg m^2
Ixz	1331 kg m^2
Wing Span (b)	9.144 m
Wing Area (S)	87.87 m^2
Wing Mean Aerodynamic Chord ($\overline{c}$)	3.45 m
Reference Center-of-Gravity Location	0.35 $\overline{c}$
Center-of-Gravity Location	0.30 $\overline{c}$

The model includes elevator, thrust, aileron, rudder and LEFs (optional) as controls, and the actuator dynamics are added with position and rate limits. Their specifications are presented in Table 2.2. Actuators of elevators, ailerons and rudders are modelled as 0.0495 seconds of first-order lags, while the lag of the LEF actuators is 0.136 seconds, and the thrust actuator has a time constant of 1 second.

Table 2.2: F-16 Model Actuator Specifications [2]

Control	Lower Limit	Upper Limit	Rate Limit
Thrust	4450 N	84515 N	44480 N/s
Elevator	-25 deg	25 deg	$\pm$ 60 deg/s
Aileron	-21.5 deg	21.5 deg	$\pm$ 80 deg/s
Rudder	-30 deg	30 deg	$\pm$ 120 deg/s
LEF	0	25	$\pm$ 25 deg/s

The model offers users "high-fidelity" and "low-fidelity" options depending on how LEFs are implemented in the model. LEFs are moving actively in the high-fidelity model, and actuator dynamics are also present. LEF movement is scheduled with respect to the angle of attack and Mach number, but according to Stevens, Lewis and Johson [36], the Mach-dependent variation of LEFs in this database is small. Thus, they rearranged the database and reduced the dimension of look-up tables first by removing the Mach dependency from LEFs and assuming they depend on alpha only. In addition, LEFs respond to changes in alpha and Mach very rapidly, so their actuator dynamics are also neglected. Then, they merged all of the independent LEF data tables into the rest of the tabular aerodynamic data. Therefore, the effect of LEF deflection is present in the reduced database, excluding the actuator dynamics.

Low-fidelity option is preferred for this study since the active movement of LEFs together with the angle of attack causes correlation problems during identification. They interfere with the short-period mode to be identified given in 3.1, which includes only elevators as the control surfaces. Therefore LEF motion will distort the identification process for such a case, as being scheduled with the angle of attack can lead to a correlation with the elevator. Hence, the "low-fidelity" database where the effect of LEFs is already embedded is preferred to eliminate the correlation problem.

As a result, the response of angle of attack and pitch rate to elevator input will also inherently include LEF effects.

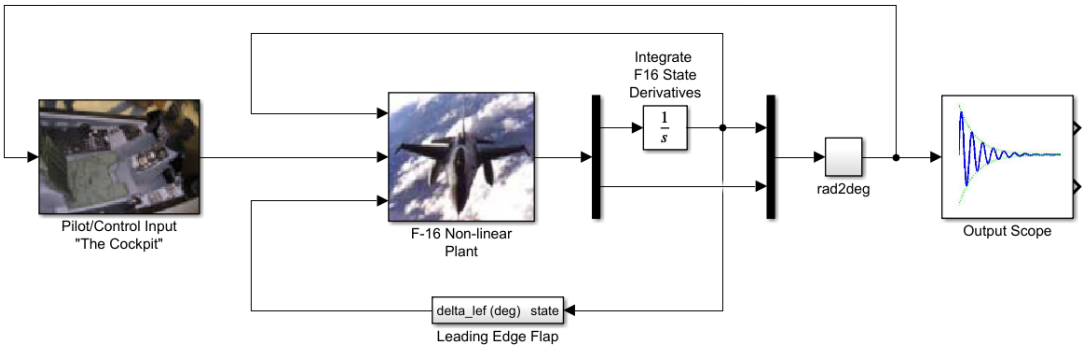

Figure 2.1: Simulink Model View

Moving to the control's sign convention, the positive deflection of the control surfaces illustrated in Figure 2.2 creates a negative moment along the body axes. For instance, trailing edge down deflection for the elevator is positive deflection, which reduces the body pitch rate q. Thrust acts along the x-body axis, and the increase of thrust leads to acceleration in the positive x-body direction.

Figure 2.2: The positive control deflections for the control surfaces [2]

Like real flight test data, the simulation sampling time is adjusted to 100 Hz, and the RK4 solver, the classic Runge-Kutta, is used. Gaussian white noise is introduced to collected time responses artificially.

2.2 Equations of Motion

The nonlinear force and moment equations in the body-axes system are used to simulate the rigid-body motions of the aircraft with six degrees of freedom. The set of equations is given in Equation 2.1 [1].

$$
\begin{aligned}
&Forces: \\
&\dot{u} = rv - qw - g\ sin\theta + \frac{\bar{q}S}{m}C_{X,t} + \frac{T}{m} \\
&\dot{v} = pw - ru - g\ cos\theta\ sin\phi + \frac{\bar{q}S}{m}C_{Y,t} \\
&\dot{w} = qu - pv - g\ cos\theta\ cos\phi + \frac{\bar{q}S}{m}C_{Z,t} \\
&Moments: \\
&\dot{p} = \frac{I_Y - I_Z}{I_X}\ qr + \frac{I_{XZ}}{I_X}\ (\dot{r} + pq) + \frac{\bar{q}Sb}{I_X}C_{l,t} \\
&\dot{q} = \frac{I_Z - I_X}{I_Y}\ pr + \frac{I_{XZ}}{I_Y}\ (r^2 - p^2) + \frac{\bar{q}S\bar{c}}{I_Y}C_{m,t}\ - H_e\ r \\
&\dot{r} = \frac{I_X - I_X}{I_Z}\ pq + \frac{I_{XZ}}{I_Z}\ (\dot{p} - qr) + \frac{\bar{q}Sb}{I_Z}C_{n,t}\ - H_e\ q
\end{aligned}
\tag{2.1}
$$

where u, v, w are components of the aircraft's translational velocity along X, Y and Z body axes and p, q, r are angular velocity components in the body frame. ϕ and θ are roll angle and pitch angle. g is the gravitational acceleration, and m is the mass of the aircraft. T is total instantaneous engine thrust, and H_e is the angular momentum of the engine. Finally, the total force and moment coefficients in the body frame are $C_{X,t}$, $C_{Y,t}$, $C_{Z,t}$ and $C_{l,t}$, $C_{m,t}$, $C_{n,t}$. For the high-fidelity model, longitudinal dynamics are given in Equations 2.2 and 2.3 [1].

$$C_{X,t} = C_X(\alpha,\beta,\delta_e) + \Delta C_{X,_{LEF}}\left(1-\frac{\delta_{LEF}}{25}\right) + \frac{\bar{c}q}{2V}\left[C_{X_q}(\alpha) + \Delta C_{X_{q,LEF}}(\alpha)\left(1-\frac{\delta_{LEF}}{25}\right)\right]$$

$$C_{Z,t} = C_Z(\alpha,\beta,\delta_e) + \Delta C_{Z,_{LEF}}\left(1-\frac{\delta_{LEF}}{25}\right) + \frac{\bar{c}q}{2V}\left[C_{Z_q}(\alpha) + \Delta C_{Z_{q,LEF}}(\alpha)\left(1-\frac{\delta_{LEF}}{25}\right)\right]$$

$$C_{m,t} = C_m(\alpha,\beta,\delta_e)\,\eta_{\delta_e}(\delta_e) + C_{Z,t}(x_{cg,ref}-x_{cg}) + \Delta C_m(\alpha) + \Delta C_{m,ds}(\alpha,\delta_e) + \Delta C_{m,_{LEF}}\left(1-\frac{\delta_{LEF}}{25}\right) + \frac{\bar{c}q}{2V}\left[C_{m_q}(\alpha) + \Delta C_{m_{q,LEF}}(\alpha)\left(1-\frac{\delta_{LEF}}{25}\right)\right] \tag{2.2}$$

where

$$\begin{aligned}\Delta C_{X,_{LEF}} &= C_{X,_{LEF}}(\alpha,\beta) - C_X\left(\alpha,\beta,\delta_e=0^\circ\right)\\ \Delta C_{Z,_{LEF}} &= C_{Z,_{LEF}}(\alpha,\beta) - C_Z\left(\alpha,\beta,\delta_e=0^\circ\right)\\ \Delta C_{m,_{LEF}} &= C_{m,_{LEF}}(\alpha,\beta) - C_m\left(\alpha,\beta,\delta_e=0^\circ\right)\end{aligned} \tag{2.3}$$

The contribution of $C_{Z,t}$ to $C_{m,t}$ in Equation 2.2 is non-zero since the aircraft's centre of gravity is not at the reference in this study.

2.3 Aerodynamic Database

The aerodynamic database is available in non-dimensional form as look-up tables in the NASA report [1] for the high-fidelity model. This database is simplified by blending the static effect of LEFs into the databases as presented in [36]. This reduced database, called as the low-fidelity model, is used in the model. Also, in [3], Morelli approximates the non-dimensional aerodynamic force and moment coefficients belonging to the same low-fidelity database by nonlinear polynomials. The aerodynamic database embedded in the nonlinear Simulink model is available within the envelope given in Table 2.3.

Table 2.3: Envelope of the Low-Fidelity Model [2]

Variable	Minimum	Maximum
Altitude [ft]	5 000	40 000
Velocity [ft/s]	300	900
Angle of Attack [deg]	-10	45
Angle of Sideslip [deg]	-30	30

The force and moment equations for the high-fidelity model given in Equation 2.2 are simplified by removing the individual terms depending on LEFs as they are already embedded in the coefficients, and deep stall characteristics, which is achieved with active LEFs. The elevator efficiency factor, η_{δ_e}, is taken as one. Then, the total body X-axis force coefficient ($C_{X,t}$), total body Z-axis force coefficient ($C_{Z,t}$) and total body pitching-moment coefficient ($C_{m,t}$) for the low-fidelity model are obtained as follows:

$$C_{X,t} = C_X(\alpha, \beta, \delta_e) + \frac{\bar{c}}{2V}\, q\, C_{X_q}(\alpha) \tag{2.4}$$

$$C_{Z,t} = C_Z(\alpha, \beta, \delta_e) + \frac{\bar{c}}{2V}\, q\, C_{Z_q}(\alpha) \tag{2.5}$$

$$C_{m,t} = C_m(\alpha, \beta, \delta_e) + \frac{\bar{c}}{2V}\, q\, C_{M_q}(\alpha) + C_{Z,t}(x_{cg,ref} - x_{cg}) \tag{2.6}$$

As seen in Equation 2.6, the non-dimensional pitch-moment derivative with respect to the angle of attack ($C_{m_{\dot{\alpha}}}$) is not explicitly written because it is already included in the C_{m_q} due to how the data is collected in the wind tunnel. In addition, as there is complete decoupling between longitudinal and lateral directions [2], the angle of sideslip dependency in Equations 2.4, 2.5 and 2.6 is neglected.

Morelli [3] also approximated the aerodynamic database for the low-fidelity model by nonlinear polynomials as follows:

$$C_Z(\alpha, \beta, \delta_e) = \left(f_0 + f_1\alpha + f_2\alpha^2 + f_3\alpha^3 + f_4\alpha^4\right)\left(1 - \beta^2\right) + f_5\delta_e \tag{2.7}$$

$$C_m(\alpha, \delta_e) = m_0 + m_1\alpha + m_2\delta_e + m_3\alpha\delta_e + m_4{\delta_e}^2 + m_5\alpha^2\delta_e + m_6{\delta_e}^3 + m_7\alpha{\delta_e}^2 \tag{2.8}$$

$$C_{Z_q}(\alpha) = g_0 + g_1\alpha + g_2\alpha^2 + g_3\alpha^3 + g_4\alpha^4 \tag{2.9}$$

$$C_{m_q}(\alpha) = n_0 + n_1\alpha + n_2\alpha^2 + n_3\alpha^3 + n_4\alpha^4 + n_5\alpha^5 \tag{2.10}$$

where

f_0	−1.378278e−01
f_1	−4.211369e+00
f_2	4.775187e+00
f_3	−1.026225e+01
f_4	8.399763e+00
f_5	−4.354000e−01

m_0	−2.029370e−02
m_1	4.660702e−02
m_2	−6.012308e−01
m_3	−8.062977e−02
m_4	8.320429e−02
m_5	5.018538e−01
m_6	6.378864e−01
m_7	4.226356e−01

g_0	−3.054956e+01
g_1	−4.132305e+01
g_2	3.292788e+02
g_3	−6.848038e+02
g_4	4.080244e+02

n_0	−5.159153e+00
n_1	−3.554716e+00
n_2	−3.598636e+01
n_3	2.247355e+02
n_4	−4.120991e+02
n_5	2.411750e+02

Figure 2.3: Polynomial Coefficients [3]

To be consistent with the decoupling assumption, the angle of sideslip dependency in the Equation 2.7 are also neglected.

Since bare-airframe dynamics are already stable, controller activation to stabilise the aircraft is not necessary. If SCAS is engaged, its effects on the identification should be taken into account as it may suppress the low-frequency excitation. Provisions for SCAS-on identification and guidance on open-loop identification of unstable plants are available in [17]. Furthermore, no controller is working off-axis to reduce the unwanted off-axis effects neither because the longitudinal and lateral dynamics of the low-fidelity F-16 model are already decoupled within the flight envelope covered in this study. The main results of this study are obtained from the open-loop responses, but in Section 4.3.2, the SCAS-on case is also studied where the bare-airframe identification is performed using closed-loop data.

CHAPTER 3

PROCEDURE

To identify the short-period mode of the aircraft, the system identification procedure suggested in Tischler and Remple's book [17] is followed, and the entire work is performed in MATLAB and Simulink environment.

The short-period approximation given in [36] is considered, and the dynamics are simplified by neglecting the axis force derivative with respect to the angle of attack rate $Z_{\dot{\alpha}}$ since it is usually small compared to V_T. Furthermore, the effect $M_{\dot{\alpha}}$ is included in M_q, as stated in the previous chapter. Finally, since α is a small angle, it can be said that the difference between the lift axis and the z-body axis is also small. Accordingly, it is assumed that $C_{L\alpha} = -C_{Z_\alpha}$, $C_{L_q} = -C_{Z_q}$ and $C_{L_{\delta_e}} = -C_{Z_{\delta_e}}$.

Based on these assumptions and simplifications, the final short-period approximation in state-space form is shown in 3.1. The dimensional derivatives are taken in SI units, and control deflections are in degrees.

$$\begin{bmatrix} \dot{\alpha} \\ \dot{q} \end{bmatrix} = \begin{bmatrix} Z_\alpha/V_{T_e} & 1 + Z_q/V_{T_e} \\ M_\alpha & M_q \end{bmatrix} \begin{bmatrix} \alpha \\ q \end{bmatrix} + \begin{bmatrix} Z_{\delta_e}/V_{T_e} \\ M_{\delta_e} \end{bmatrix} \begin{bmatrix} \delta_e \end{bmatrix} \tag{3.1}$$

In this short-period approximation, the pure relationship between elevator, α and q without the interference of LEFs is observed. Therefore, the low-fidelity model is used to remove the correlation effects of LEFs, as stated in Chapter 2. Hence, the quality of the identification process is not degraded by the correlation of multiple control surfaces, and the identified model will represent what is present in the low-fidelity aerodynamic database.

The procedure followed can be summarised as follows:

- Excitation of the system (F-16 nonlinear model) by elevator sweep inputs
- Collection of the responses and detrending of time-history data
- Windowing of the detrended time-domain data
- Calculation of frequency-response and construction of coherence function
- Transfer function estimation and parameter estimation
- Verification of the identified transfer function in the time domain by using dissimilar inputs

3.1 Input Design and Collection of Time-History Data

The success of the identification highly depends on the sufficient excitement of the system, and this can be easily ensured by giving proper inputs to the system. Different inputs excite systems differently, depending on their spectral content, as shown in Figure 3.1.

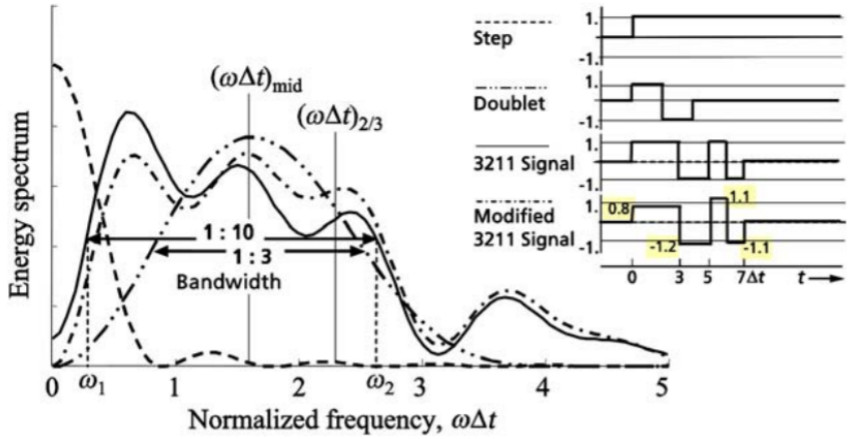

Figure 3.1: Frequency-Domain Comparison of Standard Input Signals [4]

Input plays a crucial role in sufficient excitation of the mode of interest. Morelli and Grauer [14] note that since frequency-response shows the steady-state response of a linear time-invariant dynamic system to sinusoidal inputs, it also requires steady-state

data. Therefore, transient content in the responses will bias the frequency-response estimate. To prevent the system from being affected by the transient effects, it can be excited with a single sine wave at a time, and the very last portion of the data can be used. Another solution is to use frequency-sweep inputs for excitation. Increasing the frequency at a sufficiently slow rate, the effects of transients become negligible compared to steady-state response, and steady-state response of the system at multiple frequencies can be obtained in a single run. The design guides presented in [17] also mention that the recommended input for system identification in the frequency domain is a frequency sweep. The frequency sweep refers to a class of control inputs with a quasi-sinusoidal shape of increasing frequency. Having fairly distributed spectral excitation over the desired frequency range makes frequency sweep inputs suitable for frequency-response identification, and frequency sweeps are robust to uncertainties. They can be given by pilots or might be computer-generated. In this application, computer-generated sweeps are used with suggested parameters in [17].

A sweep input δ_{sweep} can be easily implemented as a sine wave with amplitude A, which is typically 10% of the maximum deflection limits, and angular frequency ω where ω is a function of time, t:

$$\delta_{sweep} = A\, sin(\omega(t)\, t) \tag{3.2}$$

For an optimum input design, the argument of the sin term in Equation 3.2 is replaced with a tuned function. The resultant sweep input becomes as follows:

$$\delta_{sweep} = A\, sin\left[\int_0^{Trec}\left[\omega_{min} + \mathrm{C}_2\left(e^{\frac{\mathrm{C}_1 t}{Trec}} - 1\right)(\omega_{max} - \omega_{min})\right] dt\right] \tag{3.3}$$

The values C_1 = 4.0 and C_2 = 0.0187 in Equation 3.3, which are taken from [17], are experience-based numbers and suggested typical values for other parameters are:

$$T_{rec} = 90s \qquad \omega_{min} = 0.3\, rad/s \qquad \omega_{max} = 12\, rad/s \tag{3.4}$$

In addition to careful design of sweep input, there are other essential aspects to consider to excite the system sufficiently. First, the flight test should be started and ended in trim condition, and trim should be maintained for at least three seconds. Second, the deviation of the responses from the trim point should be as symmetrical as possible. Moreover, responses should be at significant amplitude so that noise effects in

the recorded data are kept minimum. The acceptable noise level can be quantified as a 10% magnitude of bias at most. Therefore, for angular attitudes and angular rates, $\pm$ 10 degrees or degrees per second is the suggested amplitude to prevent noise contamination. At the same time, the responses should not be extremely high so that the aircraft does not depart from the linear region and the initial trim condition [17].

Moving to the application part, the aircraft is trimmed at steady-wings level flight first, and sine sweep input in Equation 3.3 is fed to the elevator command (δ_{e_c}). Then, the actual elevator position (δ_e), angle of attack (α) and pitch rate (q) responses of the aircraft are collected. The block diagram is presented in Figure 3.2. The elevator sweep command and the resultant elevator deflection from trim are given in Figure 3.3. The α and q responses to elevator actuator command input are shown in Figure 3.4.

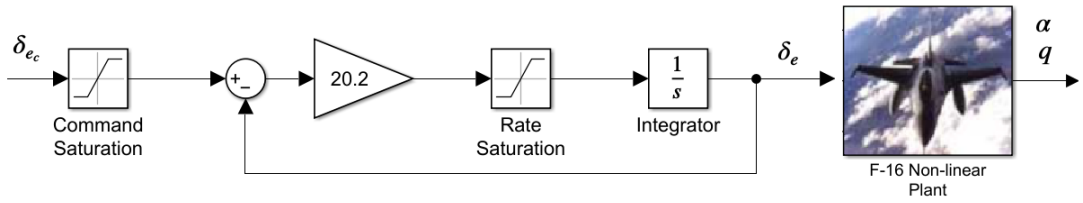

Figure 3.2: Block Diagram

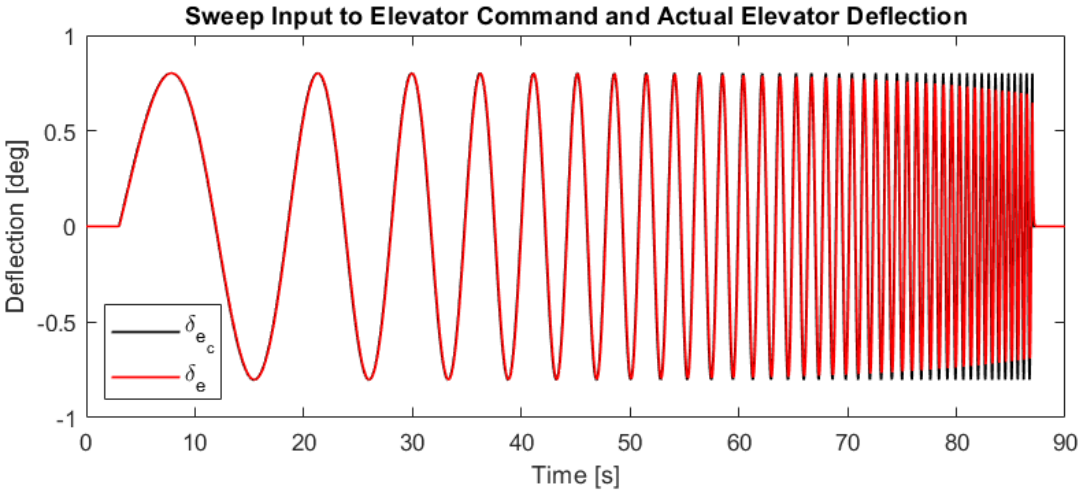

Figure 3.3: Sweep Input to Elevator Command and Actual Elevator Deflection

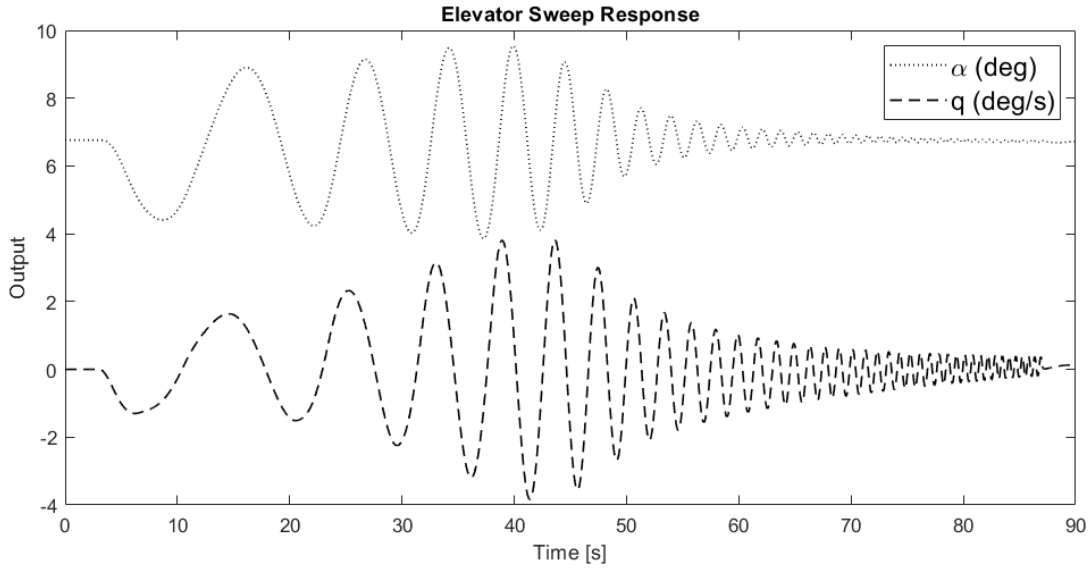

Figure 3.4: Outputs

After completing the collection of data, the amount of nonlinearity in the time-history data is examined, and response amplitudes are checked visually such that they are not extremely high or low. If the time-history plots seem unsatisfactory, excitation amplitude is readjusted, and the same procedure is repeated. As obtaining good results, detrending is applied to the time-history data. Detrending means removing low-frequency signal components with relatively high amplitude like constant part (bias) and the component related with time linearly (the linear trend or drift). Detrending is performed on time-domain data, and its application is essential before converting it to the frequency domain. Detrending aims to restrain the leakage due to low-frequency components at considerably high amplitudes, which can pollute the frequency-domain data at the lower frequencies [14]. Therefore, trim values of the input and output signals are removed before the transformation, within the scope of the detrending process.

3.2 Transformation of Time-Domain Data to the Frequency Domain

A linear system's response to a sine wave will also be a sine wave with a different amplitude and phase shift. Frequency-response is defined as the steady-state response of a system to sinusoidal inputs. One of the advantages of the frequency-response approach is that the experimental data can be used to obtain frequency-response without knowing the mathematical model of the physical system [37] as in this application. Frequency-response is constructed by data points and shows the ratio of the angle of attack and pitch rate responses per unit of control input, δ_e, as a function of the control input frequency. It is obtained by transforming observed time-domain data into frequency-domain by applying the Fourier transform [17].

3.2.1 Fourier Transform

The Fourier transform takes non-periodic signals in the time domain and converts them into equivalent frequency-based signals [17]. The Fourier transform of a time-based signal $x(t)$ is given as:

$$X(\omega) = \int_{-\infty}^{\infty} x(t)\, e^{-j\omega t}\, dt \tag{3.5}$$

The frequency-response function $H(\omega)$ is mathematically defined as the ratio of the Fourier transform of output, $Y(\omega)$, to the input transform, $X(\omega)$:

$$H(\omega) = \frac{Y(\omega)}{X(\omega)} \tag{3.6}$$

The transformation in Equation 3.5 requires a continuous signal $x(t)$ with an infinite extent, unlike actual flight-test data. Signals recorded in flight tests have a certain sampling time, making them discrete signals, and they only last for a limited amount of time. Therefore, Discrete Fourier Transform DFT is suitable for flight test data, as shown in Figure 3.5.

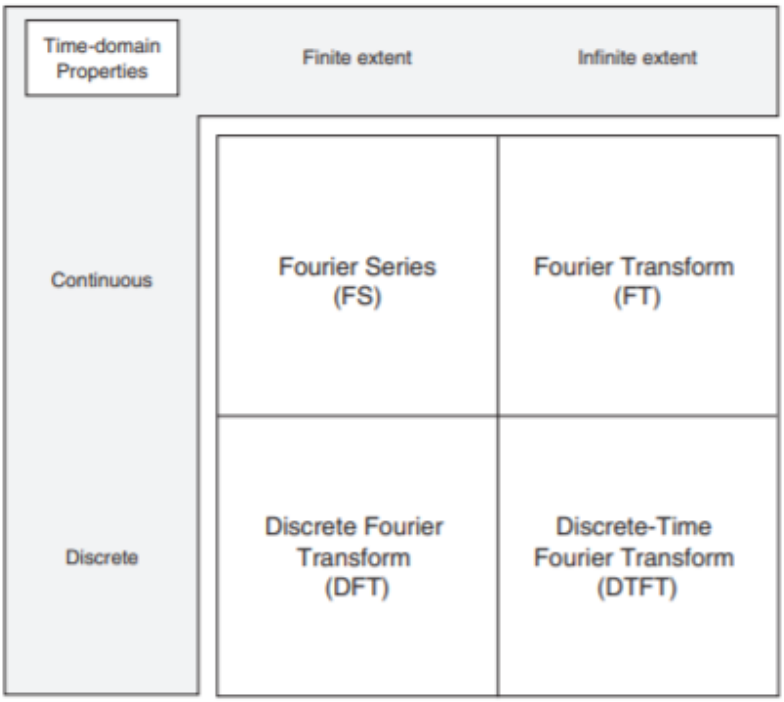

Figure 3.5: Fourier Transforms Broken Down by time-domain Properties [5]

The Discrete Fourier Transform of a signal $x(t)$ is denoted as $X(f)$ at discrete frequencies f_k, from a finite record of sampled data and is given in [17] as:

$$X(f_k) = X(k\ \Delta f) = \Delta t \sum_{n=0}^{N-1} x_n\, e^{[-j\,2\pi\,(kn)]/N} \tag{3.7}$$

where

$X(f)$ = Fourier cofficients, for $k = 0, 1, 2, ..., N-1$

$x_n = x(n\Delta t)$ = time-domain data record, for $n = 0, 1, 2, ..., N-1$

Δt = time increment

Δf = $1/N\Delta t$ = frequency resolution

N = number of discrete frequency points

$X(f)$ = Fourier cofficients, for $k = 0, 1, 2, ..., N-1$

In the DFT calculation equation 3.7, the number of discrete frequency points in the identified Fourier transform $X(f)$, N, equals to the number of discrete time points in the time-history data record x_n. The frequency points are distributed evenly from f_{min} = Δf to the sample rate f_s = $1/\Delta t$.

In this study, the application of DFT is performed by using FFT, which is a computationally more efficient algorithm.

The computational advantages of the FFT have a significant impact on the application of the spectral methods, although the basic theory is essentially unchanged. Cooley-Tukey (1965) and Bendat and Piersol (1971) are early examples of FFT aplications. Bendat and Piersol (1971), reduce the estimates' variance by dividing the data into segments. Then, FFT is applied to each data segment separately, and the average of the resulting spectral estimates is taken. However, splitting time-domain data into segments is not sufficient to compensate for spectral leakage issues like bias problems (side lobes). The mitigation of these issues is realised by tapering each segment before the transformation. Weighting each time segment by multiplying them with a tapering function, which is also a function of time, is called windowing [26].

3.2.2 Windowing

Windowing functions are weighting functions multiplied with time-domain data to reduce the spectral leakages due to finite observation intervals [38]. Before explaining the spectral leakage, the periodicity of the observed signal will be introduced first. Signals may be periodic or non-periodic, as shown in Figure 3.6. As seen in Figure 3.6, when periodic signals are added from end to end, they will form a continuous wave identical to the original signal.On the other hand, the same addition process will produce a discontinuous signal when applied to non-periodic signals, and the frequency content of the original signal will be lost due to discontinuity. The loss of accuracy in the frequency domain due to discontinuity which stems from non-periodicity, is illustrated in Figure 3.7.

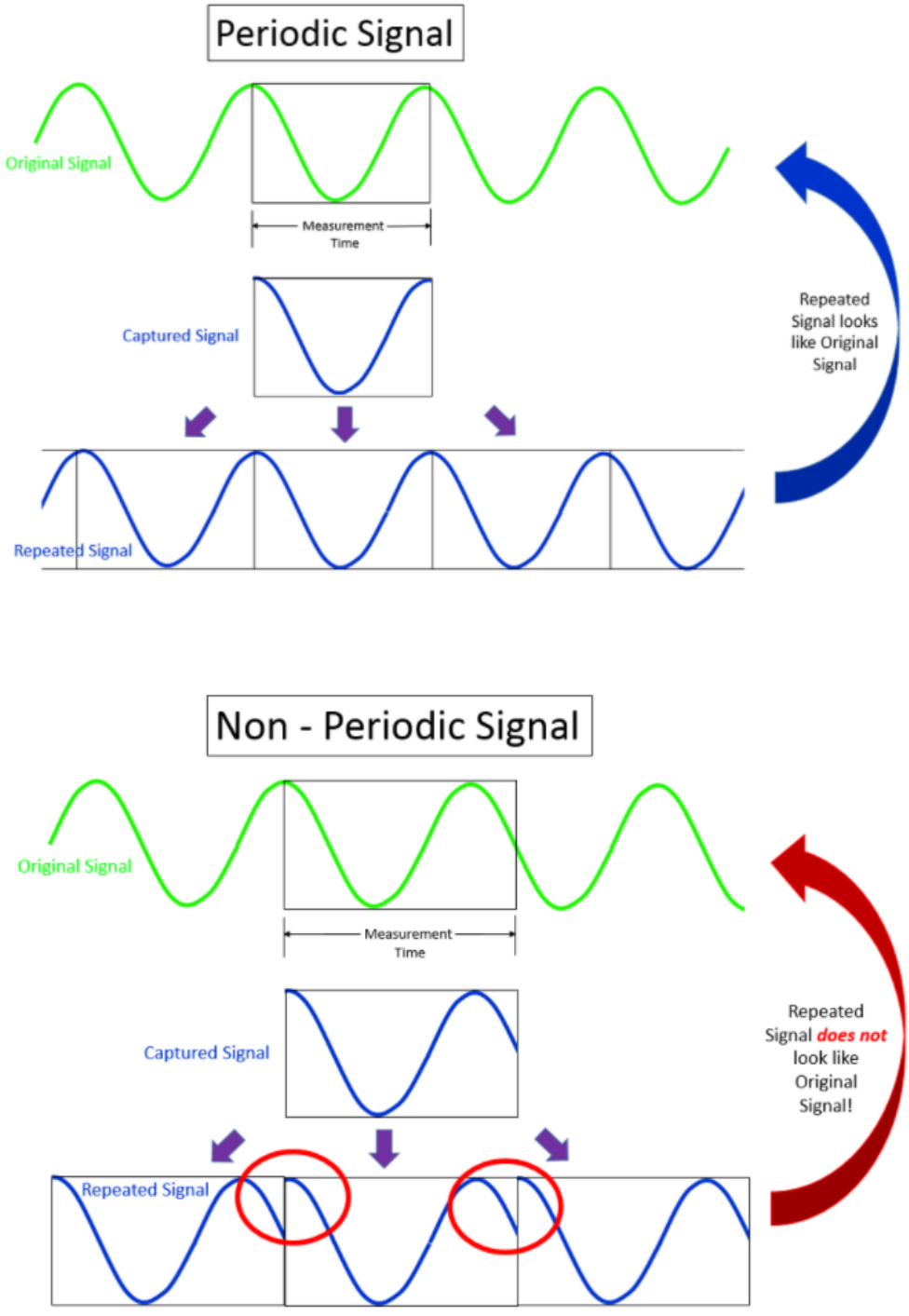

Figure 3.6: Periodic and Non-Periodic Signals [6]

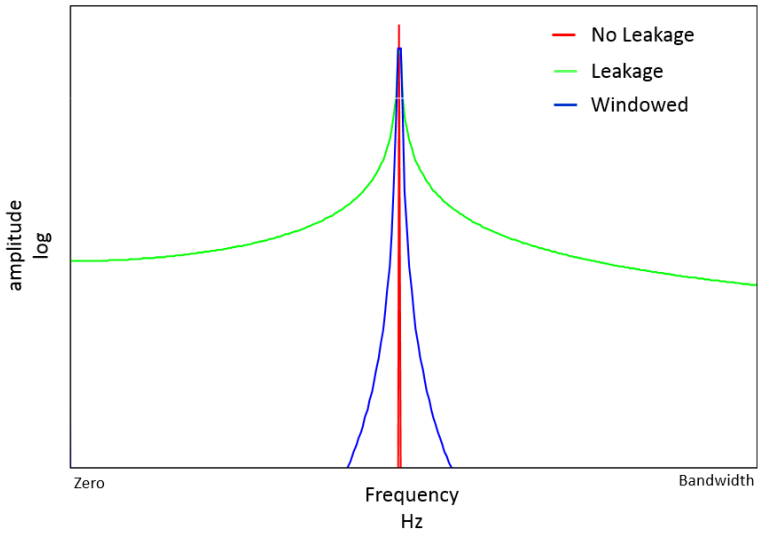

Figure 3.7: Spectral leakage [6]

The spectral leakages occur because the Fourier transform theoretically requires a signal to be periodic. In other words, the captured signal should be exactly an integer number of its cycle. If not, spectral leakage is inevitable because of the discontinuity. Windowing is applied to minimise the leakage due to the non-periodicity of the observed data. However, windowing modifies the original time signal and introduces its own errors to the estimation [9]. The transformation from the time domain to the frequency domain can be directly done by taking FFT without applying any windowing. "Without applying any windowing" or "doing nothing" on the collected time-history data imply that a rectangular window (Boxcar window or Dirichlet window) is applied to the time-domain data. A rectangular window multiplies the observed data by one and the unobserved data by zero. The rectangular window and its impact on leakage are shown in Figure 3.8 for a sine wave with 10 Hz angular velocity. Since the observed portion of the data is non-periodic, which is usually the case for real-life applications, spectral leakage occurred. This transformation yields the rough estimate of the spectral functions defined in Section 3.2.3, but the quality of the estimation may be degraded by leakage.

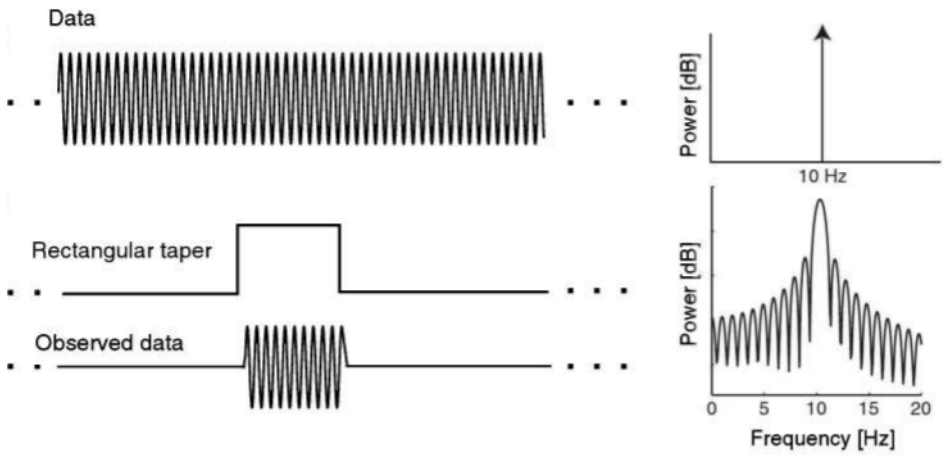

Figure 3.8: Rectangular Window [7]

The leakage due to the non-periodic nature of the observed data is evident in Figure 3.8, and the rectangular window is more leakage-prone than other window types. There are sudden jumps at the edges of the rectangular window when the signal is non-periodic, which causes dramatic discontinuities and, therefore, leakage. To mitigate leakage, there are two ways. The signal should be periodic, which is rarely the case in real life, or the severe discontinuities at the window edges should be softened. The gradual change from zero to one or one to zero is possible by applying a tapered window rather than a rectangular window [14]. The transition from zero to one or one to zero at the window edges is much softer when a tapered window is applied, as in Figure 3.9.

For example, consider a signal $y(t)$ composed of sine waves with the angular velocity of 1 Hz and 8 Hz with magnitudes of 4 and 3, respectively. Thus, $y(t)$ can be written as:

$$y(t) = 4sin(2\pi t) + 3sin(2\pi 8t) \tag{3.8}$$

Assume that the signal $y(t)$ is observed for two seconds with a sampling of 100 Hz. Since 2 seconds is an integer multiple of the cycle of $y(t)$, the observed signal is periodic, and no leakage will occur regardless of what window type is selected. In this example, the effect of the rectangular and Hanning windows is compared. The observed data and window comparison in the time domain is shown in Figure 3.10.

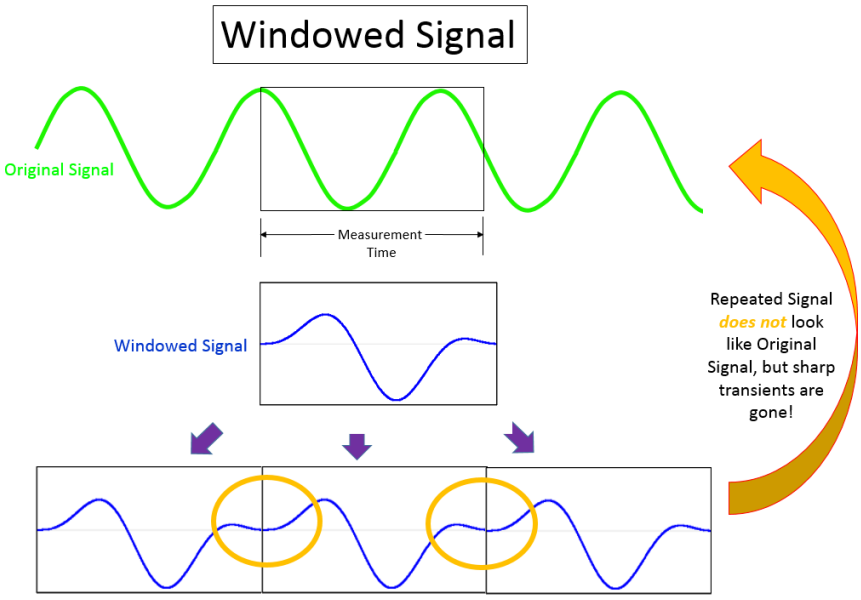

Figure 3.9: Effect of Tapered Window in Time-domain [8]

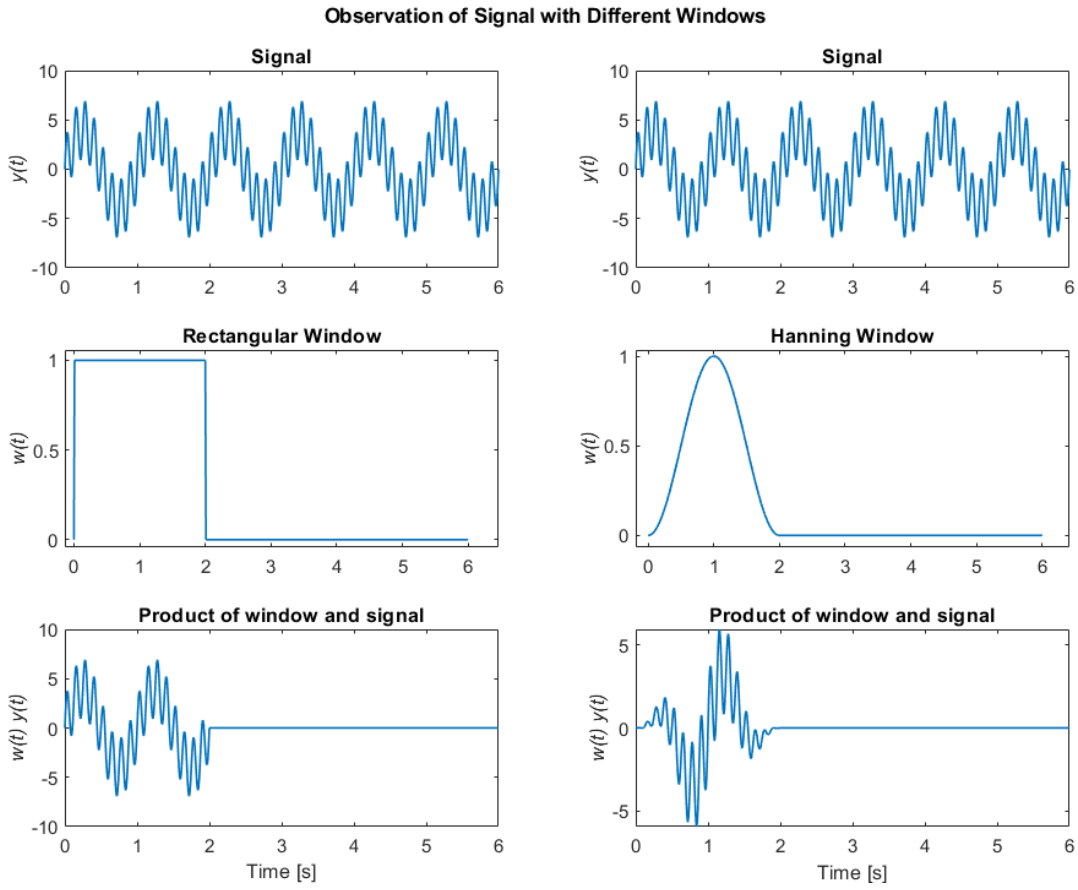

Figure 3.10: Comparison of Rectangular Window and Tapered Window in the Time Domain

The soft transition at the edges of the Hanning window compared to the rectangular window is visible in Figure 3.10. The effect of this tapering function in the frequency-domain is shown in Figure 3.11. As the observed signal is periodic, there is no leakage in the amplitude spectrum plot, and spikes are at the correct frequencies (1 Hz and 8 Hz) with correct amplitudes. Note that, unlike the rectangular window, the Hanning window reduces the signal amplitude by half so that the power magnitudes seem to be half of their actual values. The halving factor comes from Equation 3.9.

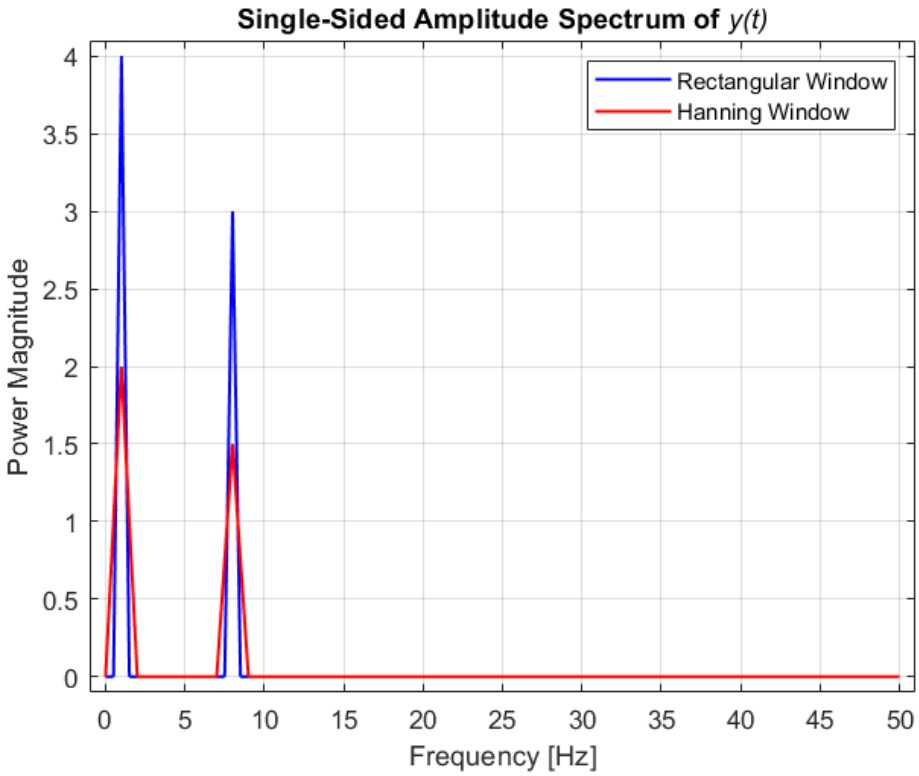

Figure 3.11: Comparison of Rectangular Window and Tapered Window in the Frequency Domain for Periodic Signal

It is shown that periodic data does not require tapering as accurate results with rectangular window can be obtained easily. Now, assume that the observation lasts not for 2 seconds but 2.56 seconds, making the observed data non-periodic. The leakage due to non-periodicity is shown in Figure 3.12.

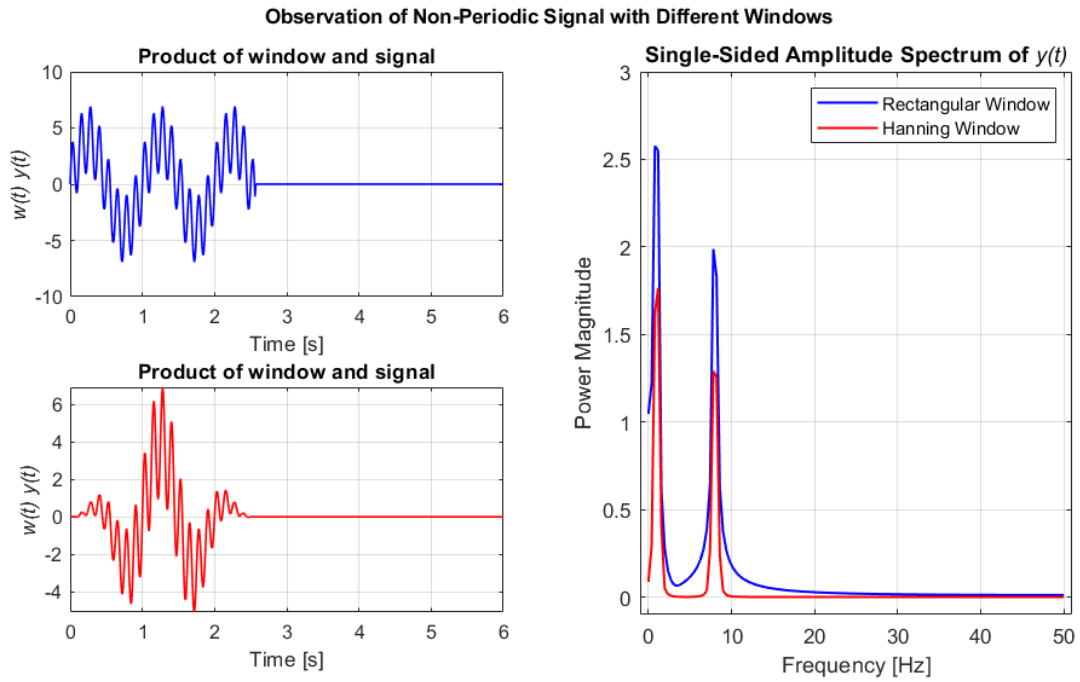

Figure 3.12: Comparison of Rectangular Window and Tapered Window in the Time and Frequency Domains for Non-Periodic Signal

The spikes in the spectrum plot are not at the correct frequencies, and the magnitude is inaccurate for both windows. However, the amount of lost information is minor in the Hanning window compared to the rectangular window. This can be understood from the amplitude at side frequencies in a rectangular window. In other words, leakage through other frequencies is less in the Hanning window. Therefore, the nature of the signal cannot be captured precisely if the observed data is not periodic, but a tapered window will be beneficial to reduce the distorting effect.

The role of tapering the segments with a smooth data window (as opposed to the rectangular window) was already demonstrated by Bendat and Piersol [39] and by many others, but no unique answer can be given to the question of what optimal window is like [16]. In the literature, several tapering functions for different purposes exist, and their suitability depends on the application. Some of the common window shapes such as Boxcar, Hanning, flat-top, Hamming, Kaiser-Bessel, Gauss and Blackman are given in Figure 3.13. Their comparison in detail, including frequency-domain comparison, is available at [40].

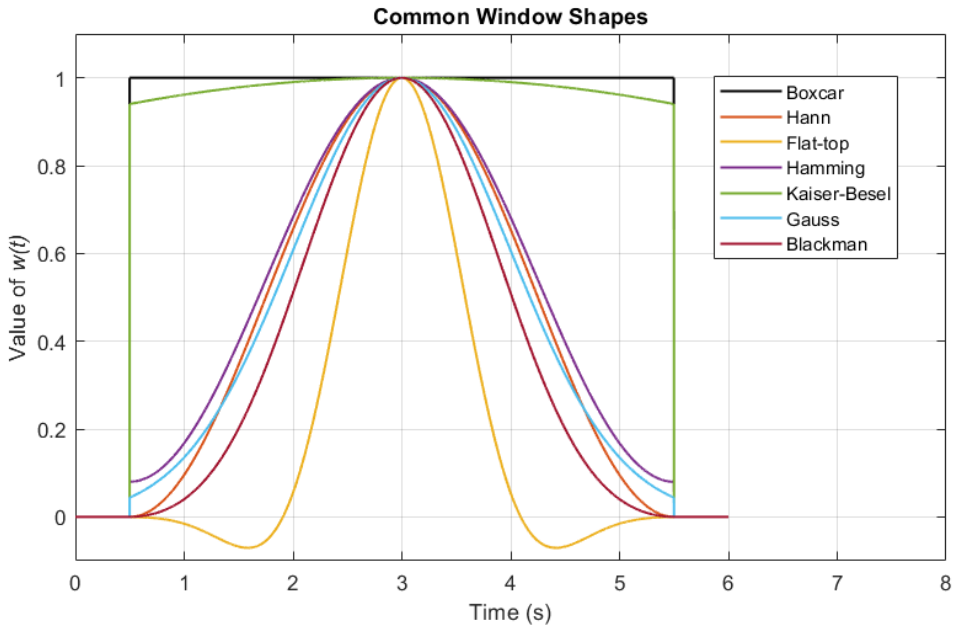

Figure 3.13: Different Window Shapes, time-domain View

Among the common window shapes, Hanning window, sometimes also called as Hann window, is suggested by Tischler and Remple [17] for aircraft system identification, and they give Hanning window function as:

$$w\left(t\right)_{Hann} = \begin{cases} \frac{1}{2}\left(1 - cos\left(\frac{2\pi t}{T_{win}}\right)\right) & \text{for } 0 \leq t \leq T_{win} \\ 0 & \text{otherwise} \end{cases} \tag{3.9}$$

The detrended time-history record is divided into time segments with a window length of T_{win}, and the data in each window is multiplied with Hanning window function $w(t)_{Hann}$ before applying FFT.

Dividing time-history data into multiple window segments is essential to obtain the smooth spectral estimates given in Equation 3.13 because smooth spectral estimates are obtained by averaging the rough estimates for multiple data segments. Furthermore, the coherence function explained in Section3.2.5, also requires multi-windowing since it is defined as a function of smooth spectral estimates [17]. While applying windowing, overlap ratio of the windows is also important. If there is no overlap between the windows, as shown in Figure 3.14, missing the information in the signal becomes a possibility. The first plot in Figure 3.14, is the sampled signal and the

second plot has four Hanning window segments with no overlap. The product of the original signal with the windowing function is given in the bottom plot of Figure 3.14, which obviously shows that the nature of the signal could not be captured. Therefore, windowing with non-zero overlap is essential for accuracy.

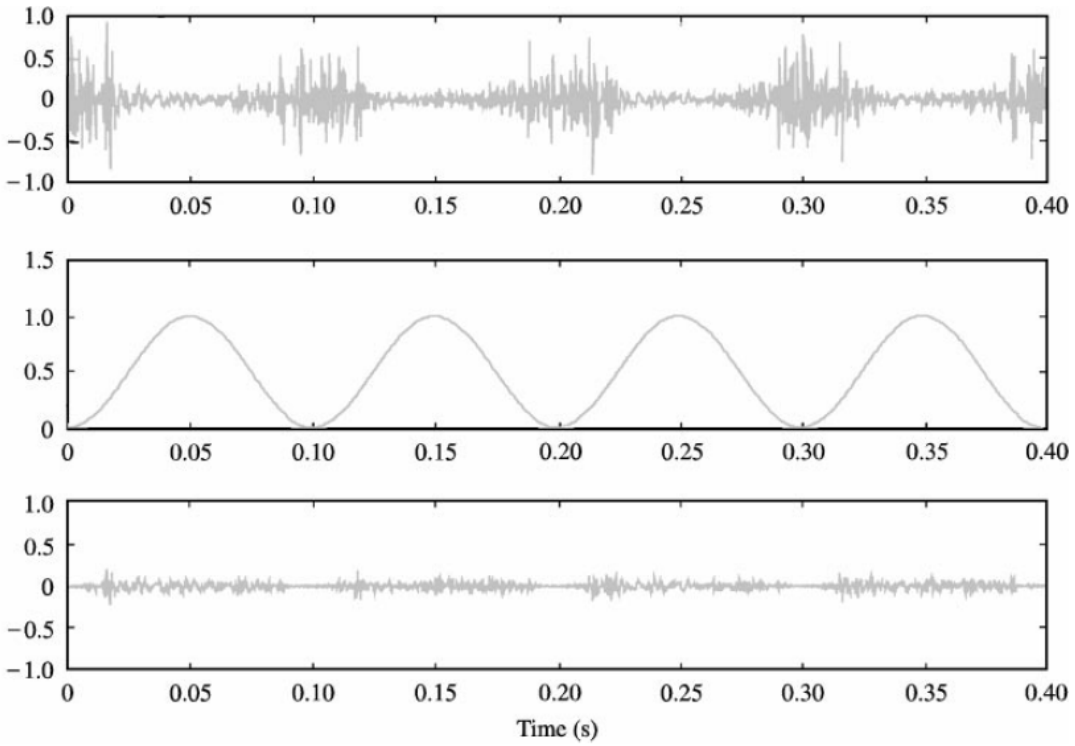

Figure 3.14: Hanning data capture window without overlap [9]

Tischler and Remple [17] state that 50% overlap reduces random error significantly, but the benefit of a higher overlap ratio comes with a computational burden. Therefore, the trade-off between higher accuracy and an increased number of calculations becomes necessary. According to their experience, 80% overlap is the sweet spot for aircraft system identification. Thus, the Hanning window with 80% overlap is applied to detrended time-domain data before taking FFT in this study.

To sum up, computing the FFT by using one rectangular window with the same length of flight-test data is possible if rough spectral estimates have desired accuracy and calculation of the coherence is not needed. However, in this application, overlapped windowing with proper taper function is required because smooth spectral estimates given in Equation 3.13 are needed for improved accuracy and to obtain coherence.

3.2.3 Spectral Functions

The spectrum of the data x is the magnitude squared of the Fourier transform of x. The spectrum indicates the amplitude of rhythmic activity in x as a function of frequency [7]. Naming the DFT of input signal x_t as $X(f)$ and DFT of the output signal y_t as $Y(f)$, $rough\ estimate$ of the $input\ autospectrum$ for a single flight record $T = T_{rec}$ is given as [17]:

$$\tilde{G}_{xx}(f) = \frac{2}{T}|X(f)|^2 \tag{3.10}$$

The input auto spectrum, also called the input power spectral density (PSD), is represented as G_{xx} and shows the distribution of the squared input x^2 or excitation power as the function of frequency f. In addition, G_{xx} stands for the one-sided spectral function in this application [17]. As a side note, double-sided spectral functions are not used since the information at negative frequencies is redundant and does not hold any physical meaning.

Similar to Equation 3.10, the rough estimate of the output auto spectrum (output PSD) can be shown as [17]:

$$\tilde{G}_{yy}(f) = \frac{2}{T}|Y(f)|^2 \tag{3.11}$$

In the same fashion, the rough estimate of the cross spectrum (cross PSD) is written as [17]:

$$\tilde{G}_{xy}(f) = \frac{2}{T}\left[X^*(f)\,Y(f)\right] \tag{3.12}$$

where * stands for the complex conjugate. Unlike input and output spectrum, cross-spectrum is a complex-valued function.

3.2.4 Frequency-Response Estimation of Windowed Time-Domain Data

As overlapped windowing is applied to the detrended time-history data, the transformation from time-domain to frequency-domain can be executed at this stage. Smooth estimates can be obtained as follows [17] by using the overlapped windowing technique:

$$\begin{aligned}
\hat{G}_{xx}(f) &= \left(\frac{1}{Un_r}\right)\sum_{k=1}^{n_r}\tilde{G}_{xx,k}(f) \\
\hat{G}_{yy}(f) &= \left(\frac{1}{Un_r}\right)\sum_{k=1}^{n_r}\tilde{G}_{yy,k}(f) \\
\hat{G}_{xy}(f) &= \left(\frac{1}{Un_r}\right)\sum_{k=1}^{n_r}\tilde{G}_{xy,k}(f)
\end{aligned} \tag{3.13}$$

where U is a correction factor applied to the overall spectral density magnitude because of the energy loss associated with the taper function $w(t)$. The correction is given as U = 0.612 = $\sqrt{3/8}$ for the Hanning window[39].

The frequency-response function estimation can be obtained from smooth spectral function estimates [17]:

$$\hat{H}_1(f) = \frac{\hat{G}_{xy}(f)}{\hat{G}_{xx}(f)} \quad or \quad \hat{H}_2(f) = \frac{\hat{G}_{yy}(f)}{\hat{G}_{yx}(f)} \tag{3.14}$$

Both definitions in Equation 3.14 will return the same values for noise-free cases. If the noise effects are present, the estimates will differ, and the selection of $\hat{H}_1(f)$ or $\hat{H}_2(f)$ depends on the noise source. In this work, it is known that input is noise-free, so the frequency-repose function estimation $\hat{H}_1(f)$ is employed as suggested in [17]. Noise is only present at the output channels: angle of attack and pitch rate.

3.2.5 Coherence Function

Another essential function is coherence function estimate $\hat{\gamma}_{xy}^2$, a product of smooth spectral estimates and a measure of linearity of the input-output relationship. Coherence function is defined as:

$$\hat{\gamma}_{xy}^2(f) = \frac{\left|\hat{G}_{xy}(f)\right|^2}{\left|\hat{G}_{xx}(f)\right|\left|\hat{G}_{yy}(f)\right|} \tag{3.15}$$

The coherence function γ_{xy}^2 can be interpreted physically as the fraction of the output spectrum G_{yy} that is linearly attributable to the input spectrum G_{xx} at frequency f [39]. For the perfectly linear processes, γ_{xy}^2 will be 1, the ideal value, which indicates that all of the output spectra are attributable to all of the input spectrum. The lowest value of γ_{xy}^2 is zero, implying that the relationship is fully nonlinear. In practice, γ_{xy}^2 can never be exactly one due to several reasons. First, the noise in the measured output signal causes contamination in the linearity of the relationship. In addition, there are nonlinearities in the nature of the system which cannot be captured by the frequency response and therefore, the system is approximated by a linear (first harmonic) describing function. There also may be process noise due to unknown or unmeasured inputs. Active controller at off-axis or gusts may be listed as some of the potential sources of such process noise, which are uncorrelated to the measured input [17].

A critical remark about the coherence function is that it requires averaging multi-windowed data to make sense. If only one window section is used, the γ_{xy}^2 value will return to 1 for the entire frequency range, regardless of whether noise or nonlinearities are present. This situation makes coherence to be meaningless and, therefore, useless. Since the coherence function is a product of the averaging data along multiple windows, it is written in terms of smooth spectral function estimates rather than rough spectral function estimates [17]. If the coherence function is calculated by using the previously given equations 3.10, 3.12, and 3.11 for a single window (rough spectral estimates, no averages), it becomes clear that its value is always one at all frequencies.

Providing a rapid interpretation of the frequency response identification process's quality makes the coherence function an essential guide. The frequency region where the value of γ_{xy}^2 is greater than 0.6 and not oscillating is accepted as a reliable region [17].

For instance, in Figure 3.15, the coherence for the angle of attack response to elevator input is high and is constant, starting from minimum frequency up to roughly 8 rad/s, and it drops off quickly after this frequency. Similarly, for the pitch rate response, γ_{xy}^2 seem to be constant with high values as desired until 10 rad/s. The transfer function estimation will be performed on the data covered by this selected frequency range.

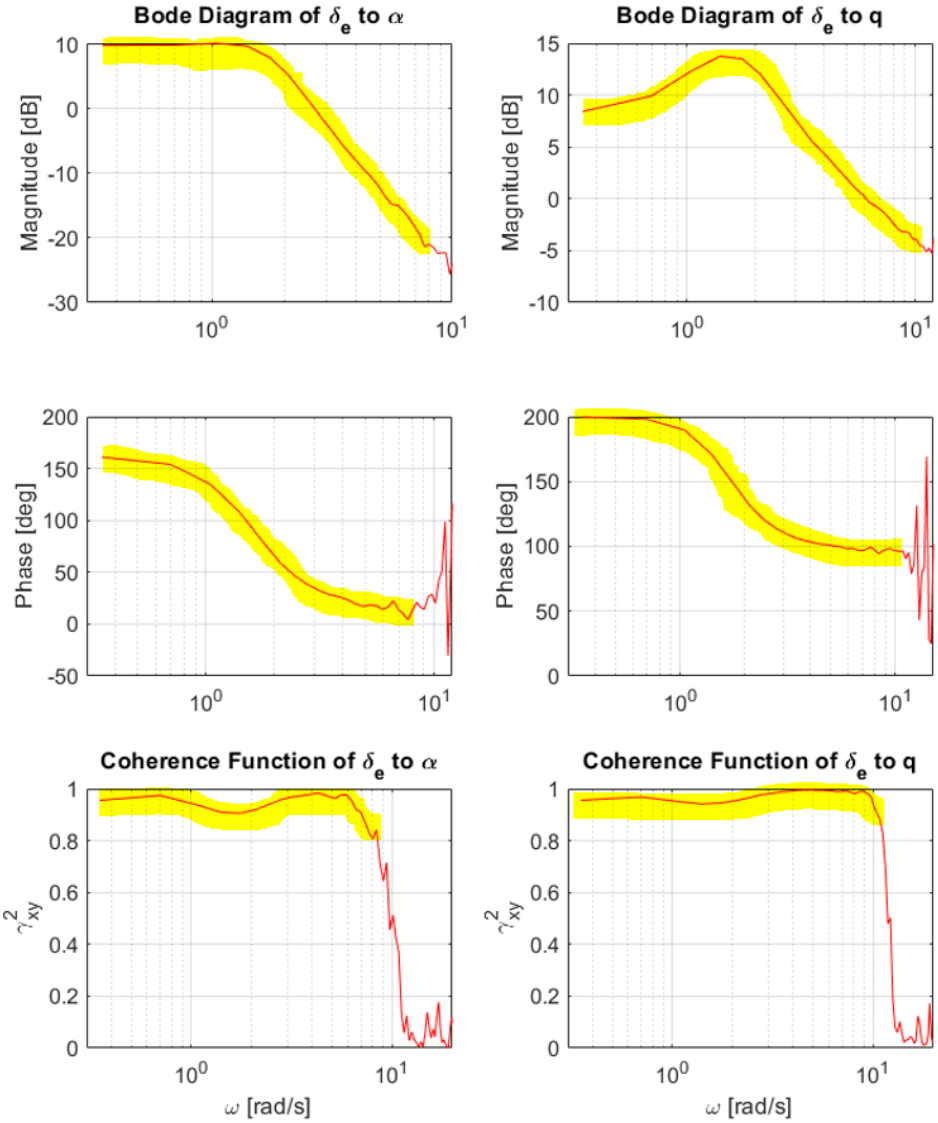

Figure 3.15: Example Use of Coherence Function with Bode Plot

3.3 Transfer Function Estimation to the Frequency-Response Data

By applying the steps up to this section, frequency-response is now in hand. The next step is to estimate a transfer function that suits the frequency-response for a bounded frequency interval. The coherence function is utilised as guidance to determine the proper frequency range in which transfer function estimation can be done healthfully. The mode of aircraft to be identified also gives the clue of the frequency range where high coherence (i.e. $\gamma_{xy}^2 > 0.6$) can be expected.

Furthermore, the order of transfer function, determined before the fitting process, also affects the identification results. The selection of a proper model structure requires various aspects to be considered. First, the ultimate application of the model has to be unambiguous (controller design, wind tunnel test verification, ...). The frequency range of interest and the quality of the available frequency-response data also play a vital role in what kind of model can be identified with the data in hand. Finally, an understanding of fundamental flight dynamics and linear systems is essential. For instance, the dynamics of fixed-wing aircraft can be accurately represented by fourth-order (or less) transfer function models (LOES modelling) [17]. In this application, a transfer function of order two is a plausible choice for F-16 aircraft because the aerodynamic database of the F-16 model does not exhibit any untypical behaviour, which needs to be taken care of. Hence, the short-period mode is approximated with the following transfer functions:

$$\frac{\alpha}{\delta_e} = \frac{Z_{\delta_e}/V_{T_e}\, s + (1 + Z_q/V_{T_e})M_{\delta_e} - (M_q Z_{\delta_e}/V_{T_e})}{s^2 - (Z_\alpha/V_{T_e} + M_q)\, s + (M_q Z_\alpha/V_{T_e}) - (1 + Z_q/V_{T_e})M_\alpha} \tag{3.16}$$

$$\frac{q}{\delta_e} = \frac{M_{\delta_e}\, s + (M_\alpha Z_{\delta_e} - Z_\alpha M_{\delta e})/V_{T_e}}{s^2 - (Z_\alpha/V_{T_e} + M_q)\, s + (M_q Z_\alpha/V_{T_e}) - (1 + Z_q/V_{T_e})M_\alpha} \tag{3.17}$$

The transfer functions 3.16 and 3.17 are obtained from the short-period approximation in Equation 3.1. Estimation of the second-order transfer functions to the frequency response data is performed by using the Sanathanan and Koerner (S-K) iteration [30] based algorithm explained in [41]. Original S-K iterations are performed to solve the nonlinear least-squares problem, which is the minimisation of the following cost function J [42]:

$$J = \sum_{i=1}^{n_f} \left| W(\omega_i) \left(y(\omega_i) - \frac{Num(\omega_i)}{Den(\omega_i)} u(\omega_i) \right) \right|^2 \tag{3.18}$$

where

n_f = number of frequencies

W = frequency-dependent weight function

u and y = measured input and output

Num and Den = numerator and denominator of the transfer function to be estimated

The difference between experimental frequency-response data and the estimated transfer function is calculated, and its magnitude is minimised in the cost function. Since the estimated transfer function is multiplied with the measured input and the difference between the product of these two is compared with the experimental output, the mismatch in magnitude and phase are both taken into account in J.

Ozdemir and Gumussoy [41] enhanced the original S-K algorithm in 3.18 by applying a second set of iterations for refinement and reduction of numerical errors. The enhanced version is employed in this study as the transfer function estimation algorithm by using $tfest$ command of MATLAB [42].

The normalised root mean squared error ($NRMSE$) in Equation 3.19 is used to evaluate the goodness of fit.

$$NRMSE = \frac{|y(\omega_i) - y(\omega_i)_{id}|}{|y(\omega_i) - y_{mean}|} \tag{3.19}$$

where

y = frequency-response magnitude

y_{id} = magnitude of the transfer function to be estimated

y_{mean} = mean of frequency-response magnitude

It is observed that the transfer function estimations with $NRMSE$ < 10% provide acceptable accuracy for both channels, α and q. For the estimations with NRMSE > 10 %, the frequency range of fit is updated by considering the coherence values until a good fit ($NRMSE$ < 10 %) is achieved. If a good estimation is not achievable by tuning the frequency range, it is suspicious that the system is properly and

adequately excited or that the plant can be represented with a second-order transfer function. The other possibility is that the transfer function estimation algorithm may also fail to find a great fit due to its search method, but this was never the case in this study. Considering the aerodynamic characteristics of the F-16, it is expected that the second-order system should be capable of representing the short-period dynamics accurately. Therefore, most likely, a poor fit is due to the poor excitation of the system. Most of the time, when such cases are encountered, it is found that there are two main underlying reasons. First, the nonlinear model is perturbed too much, so the linearity is lost. Second, actuators hitting the rate limit degraded the quality of the identification process. The remedy to such nonlinearities is the same for both cases. The input amplitude is decreased to reduce the time spent at the rate limit and prevent the model from diverging from the reference conditions.

The transfer function estimations to the frequency responses of the angle of attack and pitch rate to the elevator are performed separately. However, they need to share common denominators, as seen in equations 3.16 and 3.17. Therefore, the denominator of the α / δ_e transfer function is taken as the common denominator. The final identified model in state-space form is given in Equation 4.1.

The identified model is also compared with the output of CIFER software. FRESPID and NAVFIT modules are used for this comparison. First, the same time-history data is loaded into FRESPID and frequency-response is obtained by using the same fixed window length, T_{win}. Then, the NAVFIT module estimates the transfer function to the frequency-response data. The same frequency range with the same amount of data points is selected for the estimation. Although this is not the suggested way of using the software, it is helpful for comparison purposes.

3.3.1 Parameter Estimation from Identified Transfer Function

Since the transfer functions α / δ_e and q / δ_e are written in terms of aerodynamic derivatives, parameter estimation from the identified transfer functions can be performed. Therefore, dimensional derivatives Z_{δ_e}, M_{δ_e}, M_q, Z_α, M_α and Z_q are identified. Then, they are non-dimensionalised to make them comparable with the original aerodynamic database of the nonlinear F-16 model. The non-dimensionalisation is taken from the NASA report [1], consistent with the convention in [36]. The non-dimensional derivatives are:

$$\begin{aligned} C_{Z_{\delta_e}} &= \frac{Z_{\delta_e} m}{\bar{q} S} \qquad C_{m_{\delta_e}} = \frac{M_{\delta_e} I_y}{\bar{q} S \bar{c}} \quad C_{m_q} = \frac{2 M_q I_y V_{T_e}}{\bar{q} S \bar{c}^2} \\ C_{Z_\alpha} &= \frac{Z_\alpha m}{\bar{q} S} \qquad C_{m_\alpha} = \frac{M_\alpha I_y}{\bar{q} S \bar{c}} \quad C_{Z_q} = \frac{2 Z_q m V_{T_e}}{\bar{q} S \bar{c}} \end{aligned} \tag{3.20}$$

where the value of $\bar{q}$ is taken as the reference trim condition value. The natural frequency and the damping of the short-period mode can be calculated from the identified transfer functions by writing the denominator of α / δ_e and q / δ_e in terms of ω_n and ζ as in Equation 3.21.

$$\begin{aligned} & s^2 + 2\omega_n \zeta s + {\omega_n}^2 = s^2 - \left(Z_\alpha / V_{T_e} + M_q\right) s + \left(M_q Z_\alpha / V_{T_e}\right) - \left(1 + Z_q / V_{T_e}\right) M_\alpha \\ & yields \\ & \omega_n = \sqrt{\frac{M_q Z_\alpha - M_\alpha \left(V_{T_e} + Z_q\right)}{V_{T_e}}} \qquad \zeta = -\frac{M_q + Z_\alpha / V_{T_e}}{2\sqrt{\left(M_q Z_\alpha - M_\alpha \left(V_{T_e} + Z_q\right)\right) / V_{T_e}}} \end{aligned} \tag{3.21}$$

3.4 Verification of Identified Transfer Function in time-domain

It is advised to verify the identified model by returning to the time domain and exciting the system with dissimilar inputs. Dissimilar inputs are the inputs that are not in the form of those used for identification. As the system was excited by frequency sweeps for identification purposes, steps and doublets are examples of dissimilar input forms in this case. Therefore, doublet input is fed into the elevator command channel for verification. Then, the response of identified model and nonlinear model to the doublet input are compared in the time domain by calculating the time domain least-squares error, J_{rms}, between them:

$$J_{rms} = \left(\frac{1}{n}\right)\sqrt{\sum_{i=1}^{n}\left(y_{data,i} - y_{id,i}\right)^2} \tag{3.22}$$

Acceptable accuracy for flight mechanics application is suggested in the book [17] as:

$$J_{rms} \leq \ 0.5 \ to \ 1.0 \tag{3.23}$$

for fixed-wing aircraft, and the unit of the responses are in degrees or degrees per second.

CHAPTER 4

RESULTS

The procedure explained in Chapter 3 is applied to the F-16 nonlinear model described in Chapter 2 in this study, and the identification process is repeated at different trim conditions in the flight envelope. One flight condition in this envelope is selected for demonstration purposes, and the application on this demo point is presented in this chapter.

4.1 Results for Demo Flight Condition

The nonlinear F-16 model is trimmed by using the trim algorithm embedded in the simulation model by [2] with minor enhancements for more precise values. For the aircraft in steady wings-level flight at 10000 ft altitude with 500 ft/s (0.46 Mach) trim airspeed V_T, the trim values are given in Table 4.1.

Table 4.1: Trim Values of F-16 in steady wings-level flight at 10000 ft altitude with 500 ft/s trim airspeed

Parameter	Trim Value
Thrust	2080.9182 lb
Elevator	-2.2520 deg
Angle of Attack	3.5973 deg
Aileron	2.3360e-13 deg
Rudder	-1.2124e-12 deg
Angle of Sideslip	-8.4887e-15 deg

Before exciting the aircraft at trim, the bare-airframe dynamics to be identified are observed, and suitability of the conventional short-period approximation in Equation 4.1 with previously stated assumptions had been evaluated. The primary aircraft states of interest are the angle of attack and pitch rate, while an additional state, elevator deflection, has to be introduced due to the elevator actuator. Therefore, the state-space representation with actuator dynamics becomes:

$$\begin{bmatrix} \dot{\alpha} \\ \dot{q} \\ \dot{\delta}_e \end{bmatrix} = \begin{bmatrix} Z_\alpha/V_{T_e} & 1 + Z_q/V_{T_e} & Z_{\delta_e}/V_{T_e} \\ M_\alpha & M_q & M_{\delta_e} \\ 0 & 0 & -20.2 \end{bmatrix} \begin{bmatrix} \alpha \\ q \\ \delta_e \end{bmatrix} + \begin{bmatrix} 0 \\ 0 \\ 20.2 \end{bmatrix} \begin{bmatrix} \delta_{e_c} \end{bmatrix} \tag{4.1}$$

Once the structure is determined, the sweep input for elevator command is designed and fed to the aircraft with trim values in Table 4.1. The sweep input equation is given in Equation 3.3, and the parameters used in the equation are shown in 3.4. The amplitude of the sweep input is adjusted such that perturbations of α and q are significant and the responses are in the linear range at the same time, while the rate saturation at high frequencies is avoided as much as possible. Various time-history plots of α and q obtained from the same F-16 model in the reference [14] were also used as guidance while tuning the input amplitude. The elevator command sweep input and elevator deflection are given in Figure 4.1, together with the rate to see if they are saturated. In this case, no saturation is observed since the rate is lower than 60 deg/s all the time.

The responses to elevator sweep input are presented in Figure 4.2. It is observed that the oscillations at all the channels are around the initial trim point as desired.

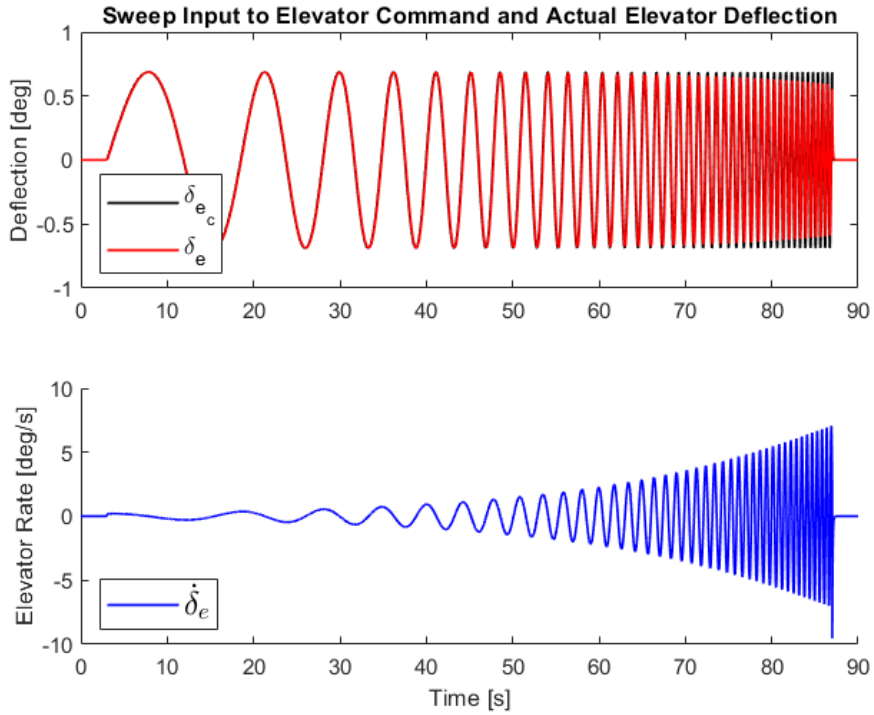

Figure 4.1: Elevator Activity

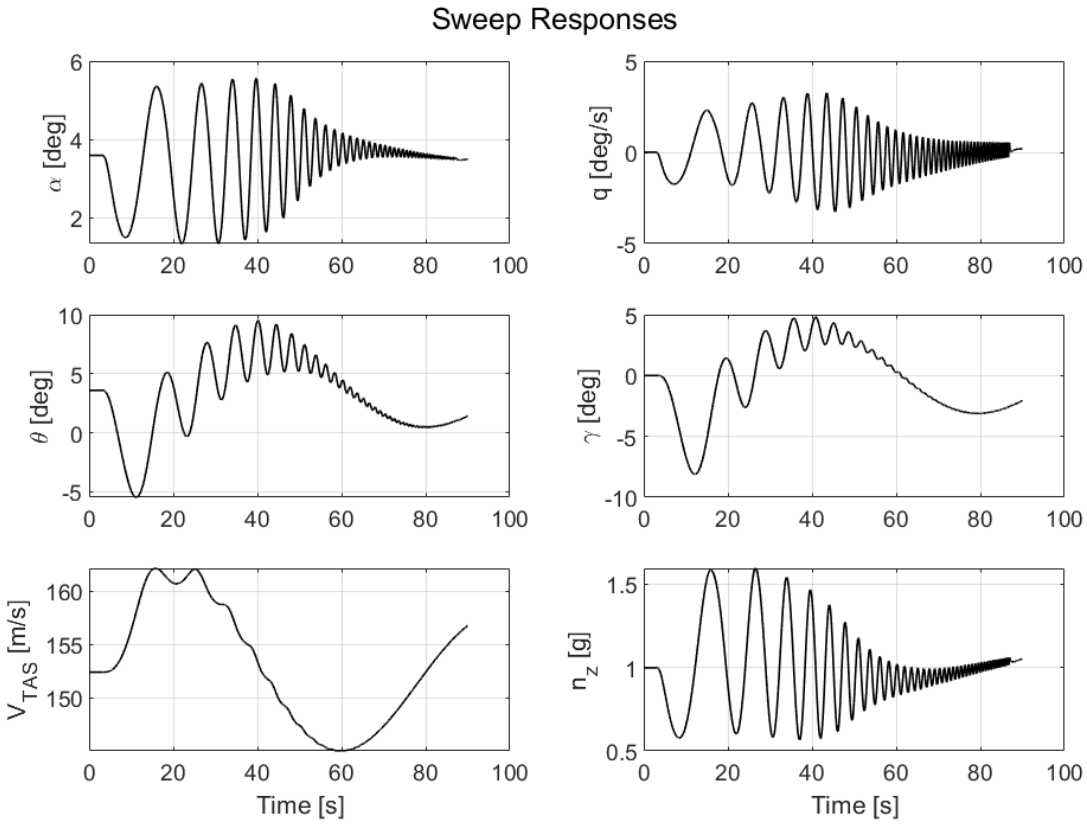

Figure 4.2: Aircraft Response to Sweep Input

Then, elevator surface deflection, α and q responses are collected, and Gaussian white noise is introduced to the responses. They are detrended before transforming into the frequency domain. Data with noise and detrended time histories are given in Figure 4.3.

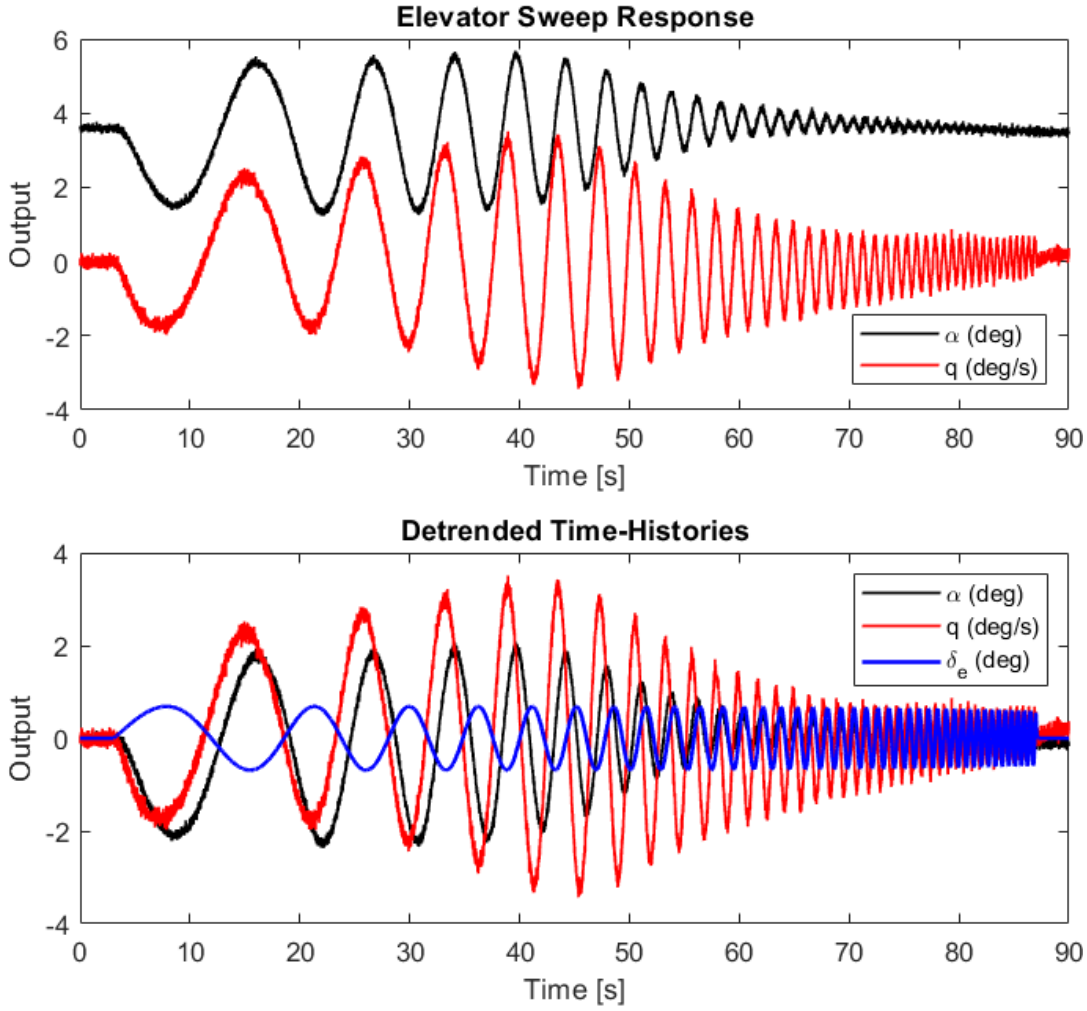

Figure 4.3: Detrended Time Histories

After detrending, windowing is applied. Determination of window length requires a trade-off. For flight mechanics applications, longer window lengths are more suitable to obtain data at lower frequencies. However, having longer windows will reduce the overall number of windows to be averaged. This will increase the random error in the estimation of smooth spectrums. Having as many windows as possible is beneficial while calculating the average. The healthy evaluation of this trade-off requires experience. Therefore, the guidelines about determining window length given by Tis-

chler and Remple in detail [17] are followed to adjust the window length. Using the guidance and experimenting with the results, the Hanning window is chosen with a window length of 18 seconds and 80% overlap, which yields 21 windows overall for the 90 seconds of the time-history record. As an example, the detrended angle of attack data, window function and their product are shown in Figure 4.4. Since the overlap ratio is given in terms of the window length, the time shift between the windows is 3.6 seconds, corresponding to the 20% of T_{win}, 18 seconds.

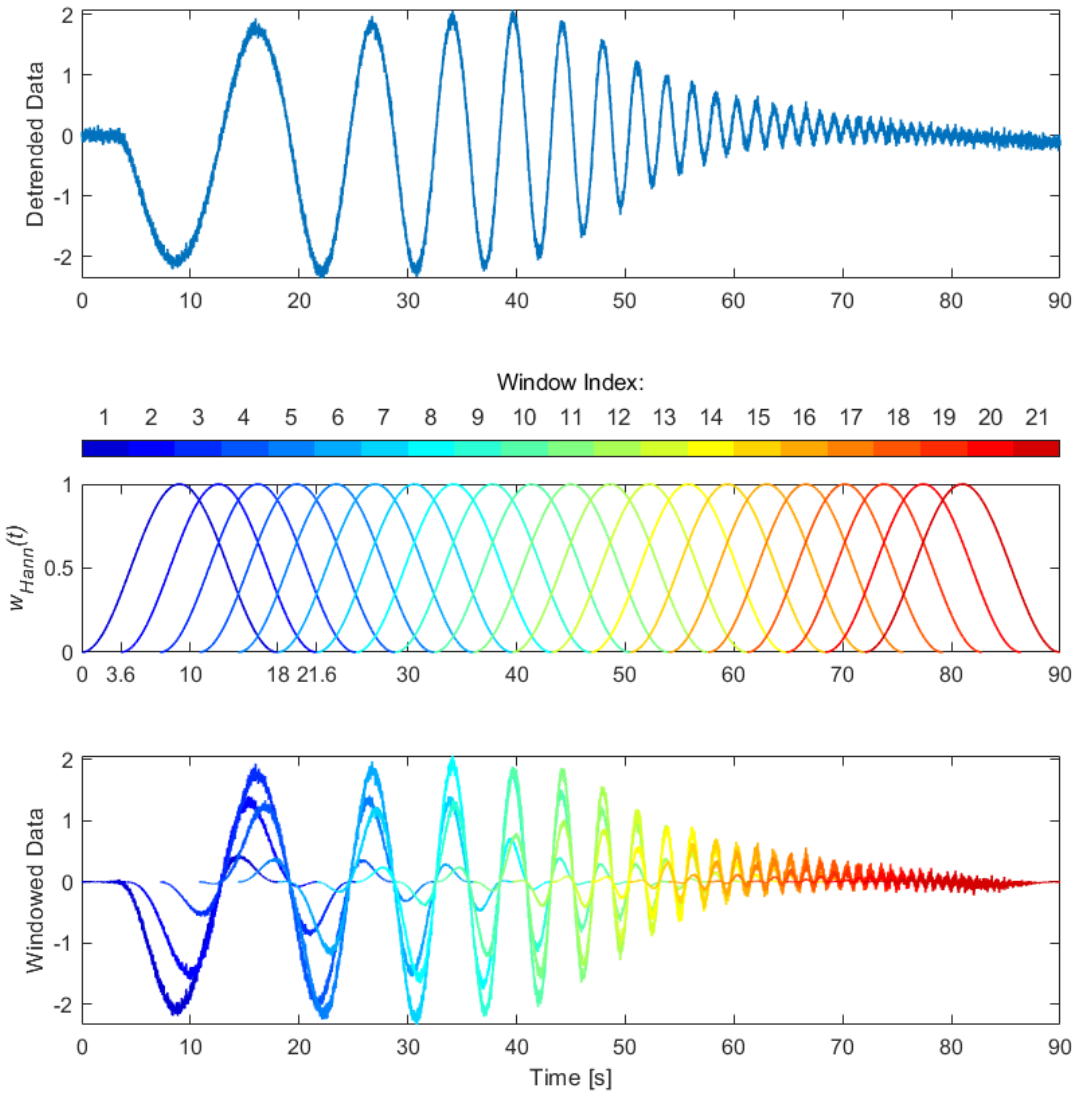

Figure 4.4: Windowed Angle of Attack Response

This window setting corresponds to a minimum identifiable frequency of 0.3491 rad/s and a maximum frequency of 314.1593 rad/s. There are 900 data points in this frequency interval for the single-sided spectrum with frequency sampling of 0.3491 rad/s, which is the inverse of window length (1/18 Hz).

FFT algorithm is applied at each window section, and rough spectrums $\tilde{G}_{\delta_e\delta_e}$, $\tilde{G}_{\alpha\alpha}$, $\tilde{G}_{qq}$, $\tilde{G}_{\delta_e\alpha}$, and $\tilde{G}_{\delta_e q}$ are calculated. The rough input auto spectrum for the elevator, $\tilde{G}_{\delta_e\delta_e}$, and the rough output auto spectrum for the angle of attack, $\tilde{G}_{\alpha\alpha}$, at each window are presented in Figure 4.5. In the same plot, the smooth auto spectrums $\hat{G}_{\delta_e\delta_e}$ and $\hat{G}_{\alpha\alpha}$ which are obtained by taking the average of the rough spectrums as shown in Equation 3.13, are also shown.

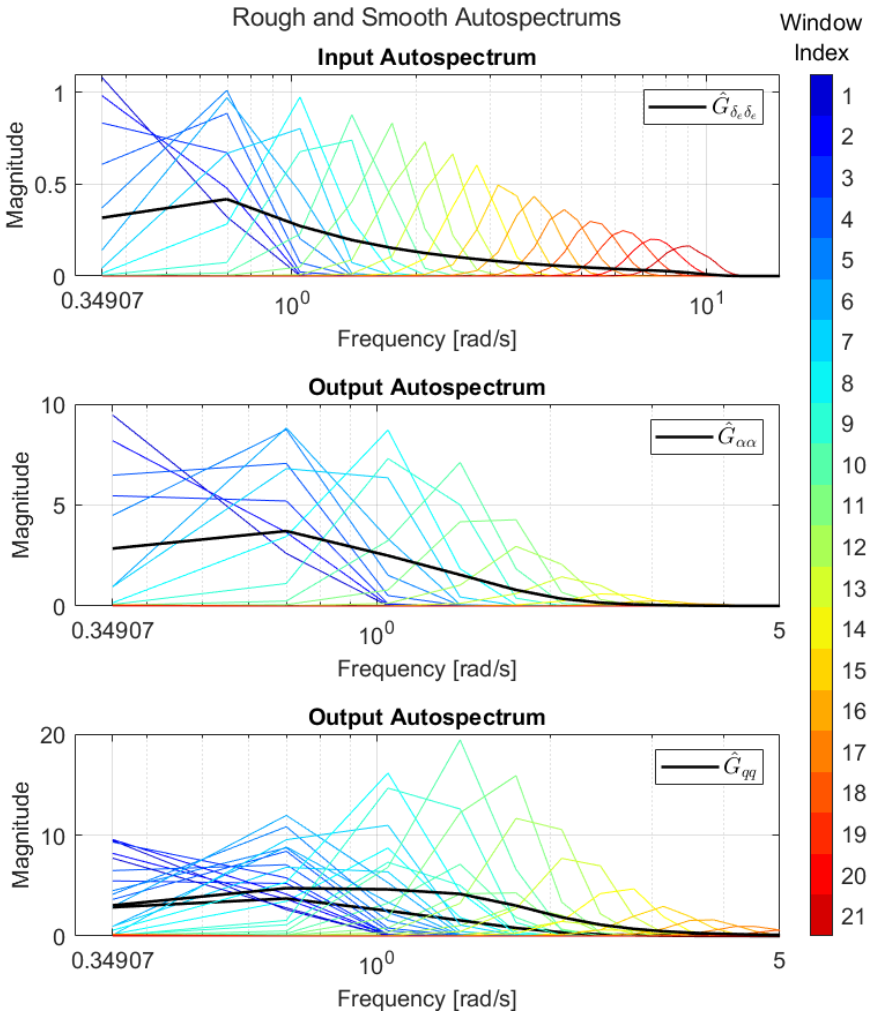

Figure 4.5: Rough Auto Spectrums $\tilde{G}_{\delta_e\delta_e}$, $\tilde{G}_{\alpha\alpha}$ and $\tilde{G}_{qq}$ together with Smooth Auto Spectrums $\hat{G}_{\delta_e\delta_e}$, $\hat{G}_{\alpha\alpha}$ and $\hat{G}_{qq}$

Similarly, the rough and smooth spectrums of for angle of attack channel are given in Figure 4.6. The cross-spectrums are complex numbers, unlike the auto spectrums. Thus, the cross-spectrum plot is given in terms of magnitude and phase.

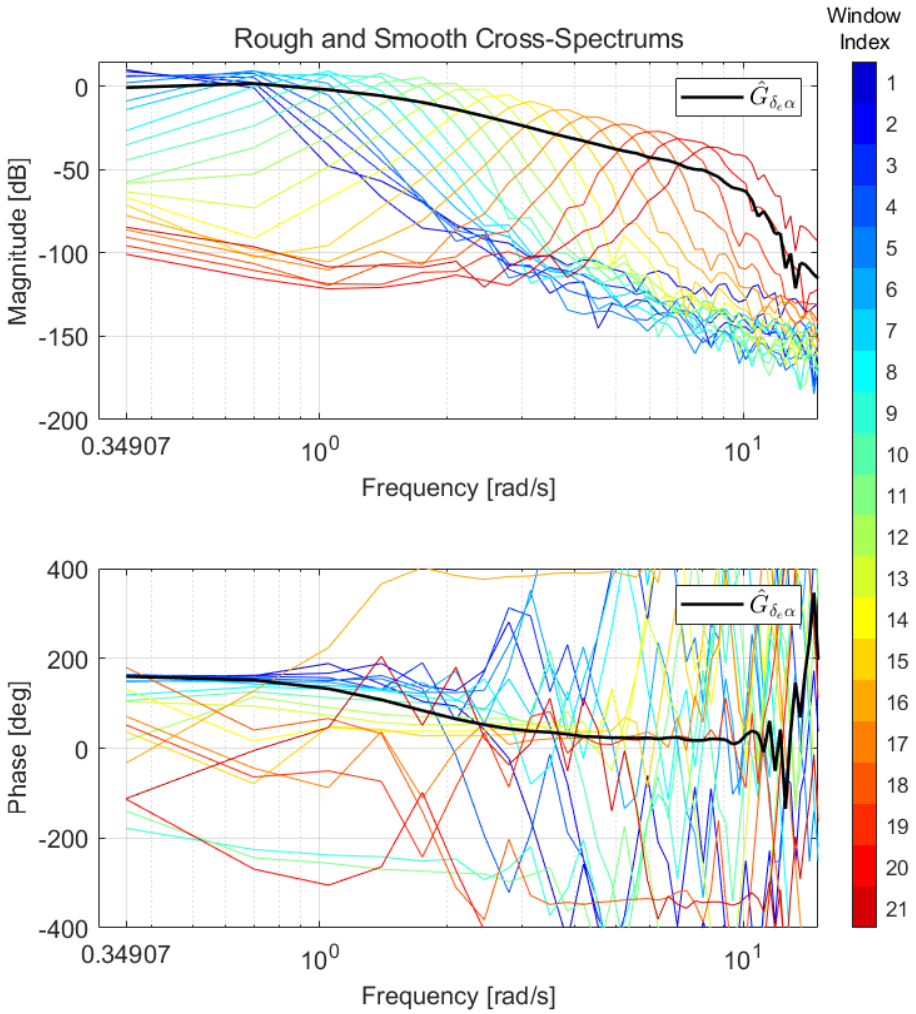

Figure 4.6: Rough Cross-Spectrums $\tilde{G}_{\delta_e\alpha}$ together with Smooth Cross-Spectrum $\hat{G}_{\delta_e\alpha}$

The frequency responses are obtained from the smooth spectrums using the relation given Equation 3.14, and they are given together with the coherence function, as shown in Figure 4.7

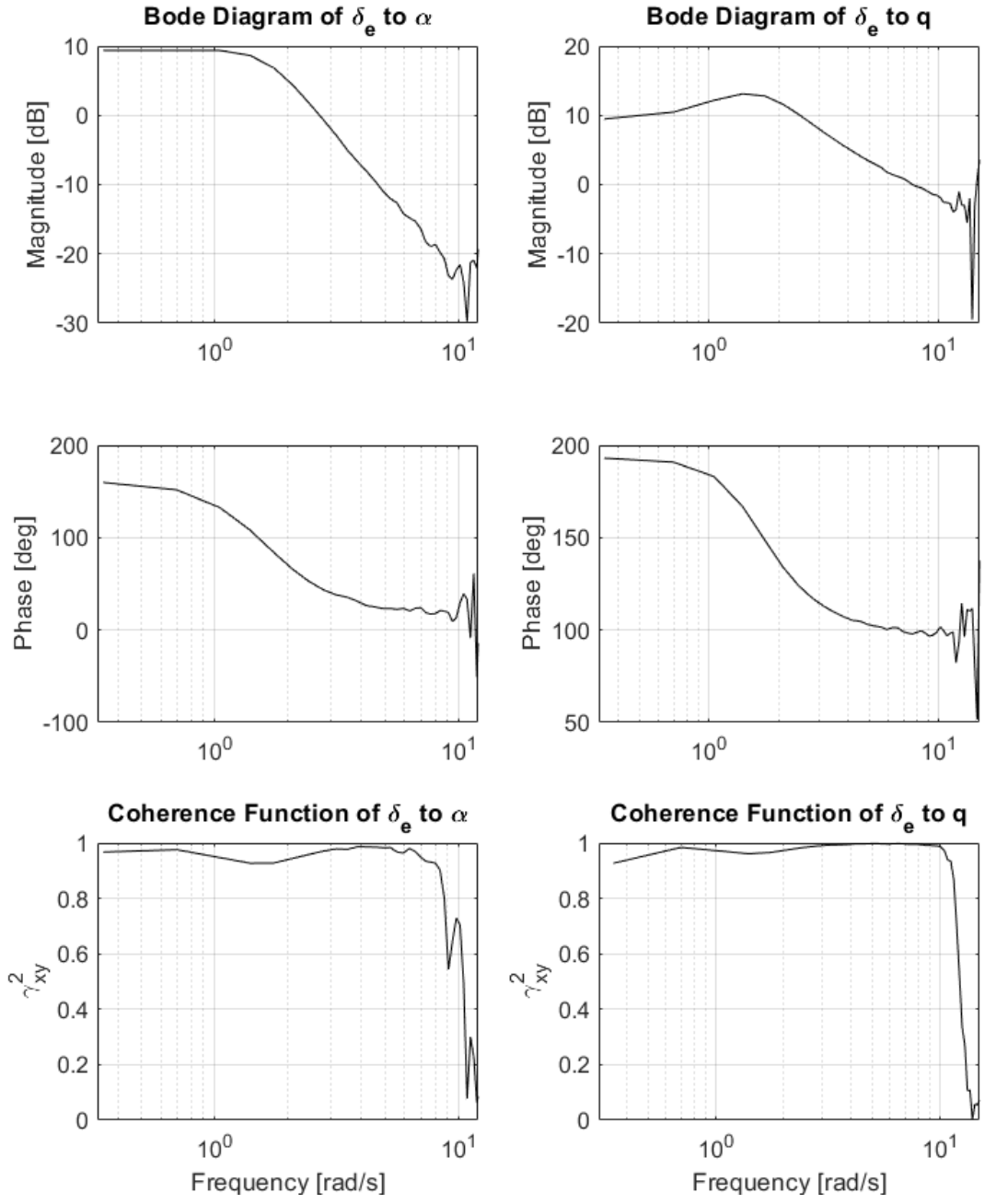

Figure 4.7: Bode Diagrams of the Frequency Responses and Coherences

The frequency interval where γ_{xy}^2 is greater than 0.6 should be selected as already stated in Section 3.2.5 for transfer function estimation. In addition to this criterion, there should not be oscillations for the coherence values to be reliable. Based on these evaluations, the frequency range selected for transfer function estimation is shown in Table 4.2.

Table 4.2: Frequency Interval with Reliable Coherence

Frequency Response	ω_{min} [rad/s]	ω_{max} [rad/s]
$\frac{\alpha}{\delta_e}$	0.3491	8.7266
$\frac{q}{\delta_e}$	0.3491	11.8682

Within the frequency intervals in Table 4.2, transfer function estimations are performed separately for the frequency-responses α/δ_e and q/δ_e. Table 4.2 indicates that 25 data points for α/δ_e and 34 for q/δ_e are considered for the estimation. Since the transfer function estimation is performed separately, $\alpha(s)/\delta_e(s)$ and $q(s)/\delta_e(s)$ have different denominators, which is physically unacceptable. Therefore, one of the denominators should be selected as the common denominator. Even though the number of data points used for the estimation is fewer, selecting the denominator of $\alpha(s)/\delta_e(s)$ as the common denominator provided more accurate results. Therefore, the denominator of the identified transfer function $\alpha(s)/\delta_e(s)$ is taken as the common denominator. The identified transfer functions are:

$$\frac{\alpha}{\delta_e} = \frac{-0.1725s - 7.021}{s^2 + 1.783s + 2.571} \tag{4.2}$$

$$\frac{q}{\delta_e} = \frac{-7.368s - 5.465}{s^2 + 1.783s + 2.571} \tag{4.3}$$

The match of the identified transfer functions to the frequency-response data shown in Figure 4.7 is presented in Figure 4.8. The blue line represents the identified transfer functions in Equations 4.2 and 4.3.The figure shows that the collected frequency-response data can be represented as second-order transfer functions with high accuracy.

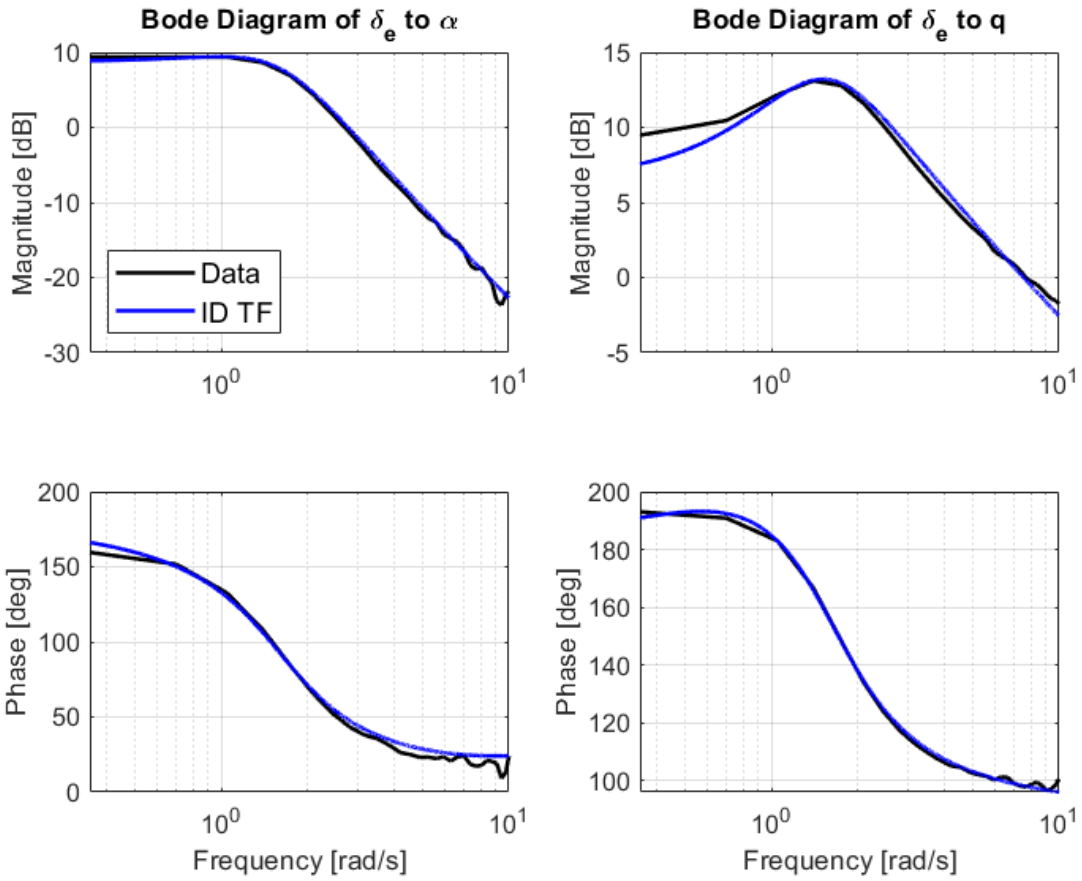

Figure 4.8: Bode Diagrams and Identified Transfer Functions

Having identified the transfer functions, the verification in time domain and parameter estimation is the next step normally. However, before that, sharing Bode plot comparisons of the identified transfer functions and the linearised model is beneficial. The identified transfer functions are multiplied by the actuator transfer function, $20.2/(s + 20.2)$, since the linearisation is done between the input δ_{e_c} to the responses α and q. Like the trim algorithm, the linearisation algorithm is also retrieved from Russell [2]. The comparisons for the angle of attack and pitch rate are shown in Figures 4.9 and 4.10.

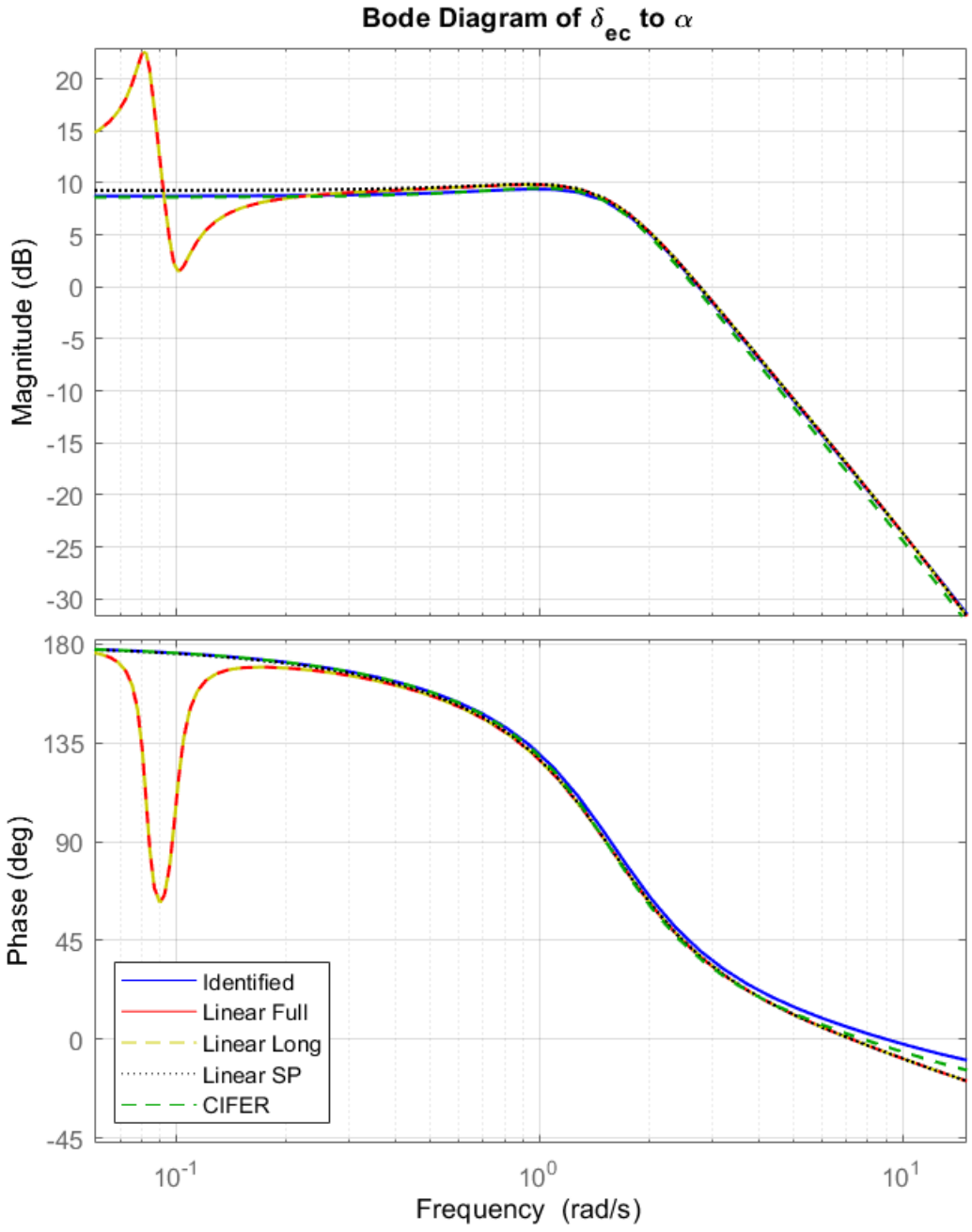

Figure 4.9: Comparison of the Identified Transfer Function and the Linear Model- Angle of Attack

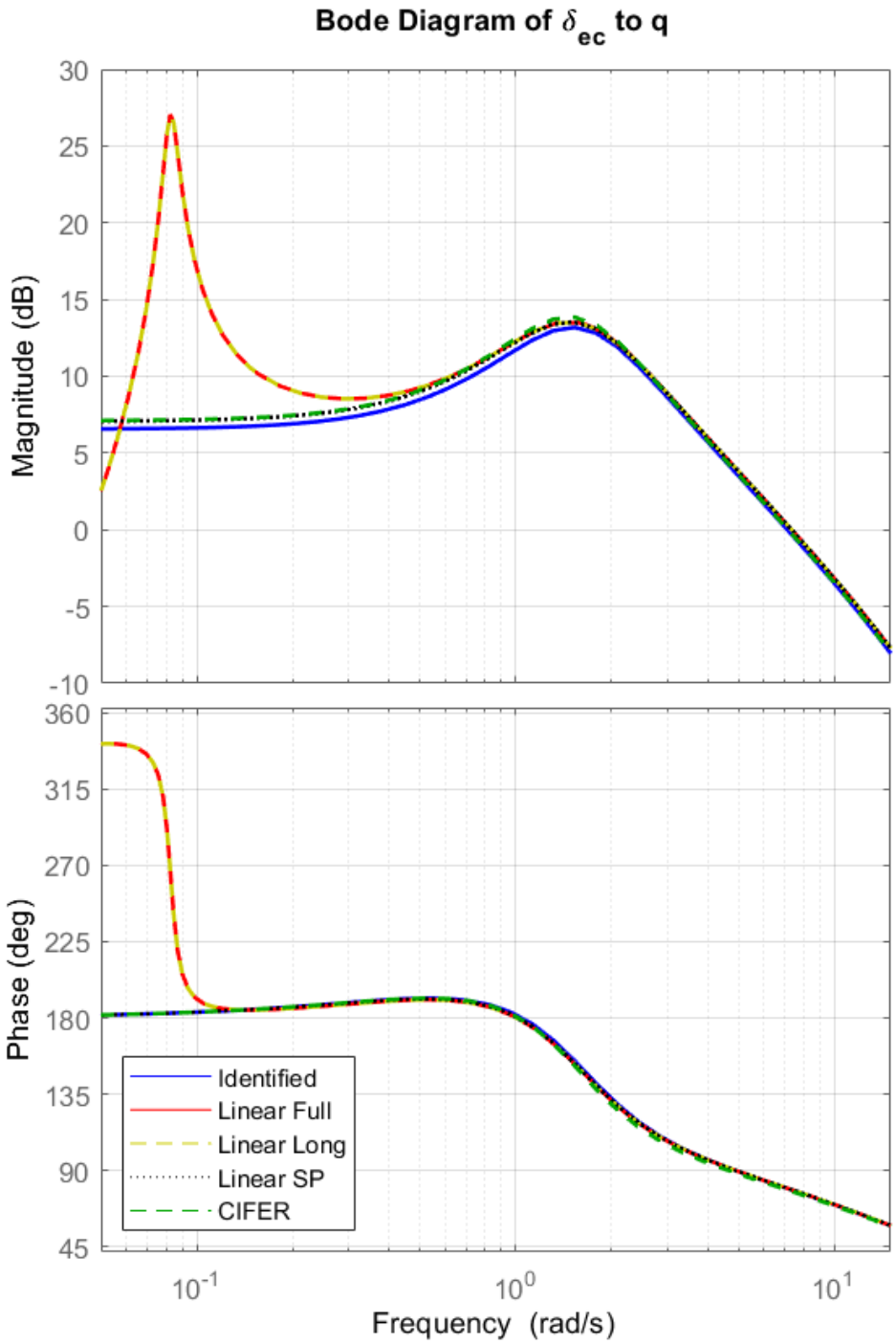

Figure 4.10: Comparison of the Identified Transfer Functions and the Linear Model-Pitch Rate

In Figure 2.3, the line labelled as Linear Full represents the linear model with all the states and controls h, θ, V, α, q, δ_{t_c}, δ_{e_c}, ϕ, ψ, β, p, r, δ_{a_c}, δ_{r_c}. The Linear Long line includes the longitudinal states and controls h, θ, V, α, q, δ_{t_c}, and δ_{e_c}. Linear SP has only the states α, q and the control δ_{e_c} as in the short-period approximation in Equation 4.1. Finally, the line "CIFER" represents the output of the CIFER software, which is obtained by using the same time-history data. The same amount of data points is used for the same frequency interval for the comparison with CIFER.

As expected, the Linear Full and Linear Long lines are on top of each other since there is decoupling between longitudinal and lateral dynamics. The difference between Linear Long and Linear SP shows the accuracy lost by short period approximation as other dynamics contributing to the longitudinal channel are excluded. Due to phugoid mode involvement, the discrepancy is high in the lower frequency range (0.1 rad/s to 0.5 rad/s). After the frequency of 0.5 rad/s, a strong agreement between Linear Long and Linear SP is observed as expected since the short-period mode becomes the dominant mode. The identified transfer function's behaviour should match Linear Long behaviour starting from the ω_{min} up to ω_{max}. It is also expected from the identified line to pass a very close Linear SP line throughout the entire frequency range, including the low-frequency interval. Based on the Bode plots in Figure 2.3, the behaviour of the identified transfer functions implies a satisfactory identification. However, accurate linear models may not be available, so the comparison between identified model and another linear model may be inapplicable in other applications. The identified model is also compared with the output of CIFER software. While the identified and CIFER models agree on the angle of attack, there is a slight offset in the pitch-rate magnitude plot at low frequencies, which is acceptable since CIFER employs a different fitting algorithm.

Then, the identified transfer functions are verified in the time domain by doublet inputs, and the J_{rms} is calculated for both α and q responses, as shown in Equation 3.22. The J_{rms} threshold for satisfactory identification is specified in Equation 3.23. The doublet input and the responses with J_{rms} values are presented in Figure 4.11. Since the doublet input is given when time is equal to one second, J_{rms} is calculated for the time interval of 1 second to 13 seconds.

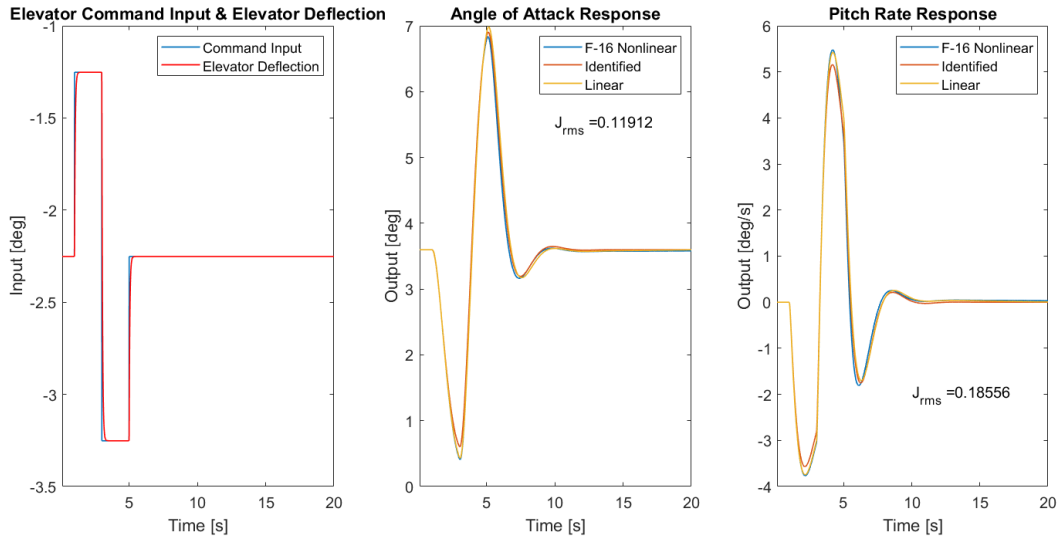

Figure 4.11: Identified Model Response to Doublet Input

Low J_{rms} values in Figure 4.11 and a close match between the nonlinear model indicate that the identified model has excellent accuracy.

Finally, the aerodynamic derivatives are extracted from the identified transfer functions since they are in the form of aerodynamic derivatives. Equating the coefficients of the identified transfer functions, Equations 4.2 and 4.3, to the related parameters in Equations 3.16 and 3.17 numerically gives the aerodynamic derivates in the dimensional form:

$$\begin{aligned} Z_{\delta_e} &= -26.2961 \qquad M_{\delta_e} = -7.3679 \quad M_q = -0.9962 \\ Z_\alpha &= -119.9073 \qquad M_\alpha = -1.9229 \quad Z_q = -10.7239 \end{aligned} \tag{4.4}$$

The relationship between dimensional derivatives and short-period natural frequency and damping ratio was given in Equation 3.21. By inserting the values in Equation 4.4 into this relationship, the natural frequency and damping ratio are found as:

$$\omega_n = 1.6036 \; rad/s \qquad \zeta = 0.5560 \tag{4.5}$$

Then, the derivatives are non-dimensionalised, as given in Equation 3.20. The aerodynamic derivatives in non-dimensional form become:

$$\begin{aligned} C_{Z_{\delta_e}} &= -0.8349 \qquad C_{m_{\delta_e}} = -0.5520 \quad C_{m_q} = -6.5938 \\ C_{Z_\alpha} &= -3.8068 \qquad C_{m_\alpha} = -0.1441 \quad C_{Z_q} = -30.0793 \end{aligned} \tag{4.6}$$

The derivatives are compared with those of F-16 aircraft given in the NASA Report [1] and the nonlinear polynomials by Morelli [3]. The derivatives are also calculated from the linearised model containing only α and q states and were shown with the label "Linear SP" in Figures 4.9 and 4.10. The only derivatives that can be explicitly compared are C_{Z_q} and C_{m_q}. The comparison for these two derivatives is given in Table 4.3 at the demo flight condition. The values of C_{Z_q} are in agreement even though it is usually dropped from the identification procedure due to high insensitivity, which indicates that it does not significantly impact aircraft dynamics [43]. Considering that C_{Z_q} stands for the change in lift force due to a change in pitch rate, it is reasonable to exclude it. However, it is kept in the model since its value is identified accurately. The identified value of C_{m_q} is very accurate compared to its value calculated from the linearised model. The accuracy of C_{m_q} is vital because if the amount of change in pitching moment due to change in pitch rate is not accurate, the model's overall quality obviously cannot be great.

Table 4.3: Comparison of the Derivatives C_{Z_q} and C_{m_q}

Derivative	Identified	F-16 Database	Polynomial	Linear SP Model
C_{Z_q}	-30.0793	-30.2195	-32.0092	-30.7519
C_{m_q}	-6.5938	-5.4584	-5.4747	-6.7978

Since the other derivatives are not explicitly available in the database, interpolation of look-up tables is necessary to compare. The nonlinear polynomial fit is an accurate approximation of the database, and therefore, there is no need to write another interpolation algorithm. As a result, other derivatives are compared with the values from the polynomial fit. Considering Equation 2.7, the derivatives C_{Z_α} and $C_{Z_{\delta_e}}$ can be driven by taking the partial derivative of the polynomial as follows:

$$C_{Z_\alpha} = f_1 + 2f_2\alpha + 3f_3\alpha^2 + 4f_4\alpha^3 \tag{4.7}$$

$$C_{Z_{\delta_e}} = f_5 \tag{4.8}$$

Similarly, considering Equation 2.8, the derivatives C_{m_α} and $C_{m_{\delta_e}}$ can be driven as:

$$C_{m_\alpha} = m_1 + m_3\delta_e + 2m_5\alpha\delta_e + m_7{\delta_e}^2 + (x_{cg,ref} - x_{cg})\, C_{Z_\alpha} \tag{4.9}$$

$$C_{m_{\delta_e}} = m_2 + m_3\alpha + 2m_4\delta_e + m_5\alpha^2 + 3m_6{\delta_e}^2 + 2m_7\alpha\delta_e + (x_{cg,ref} - x_{cg})\, C_{Z_{\delta_e}} \tag{4.10}$$

The difference between $x_{cg,ref}$ and x_{cg} is calculated from Table 2.1 as 0.05. Using these equations, identified derivatives can be compared with the polynomial outputs. The comparison of the identified derivatives and the values from the polynomials are given in Table 4.4 for the demo point. For the demo point, the trim angle of attack is 3.5973°, and the trim elevator deflection is -2.2520°, as given in Table 4.1. The values of the derivatives calculated from the linearised model, the Linear SP Model, are also included for the comparison.

Table 4.4: Comparison of the Derivatives C_{Z_α}, $C_{Z_{\delta_e}}$, C_{m_α} and $C_{m_{\delta_e}}$

Derivative	Identified	Polynomial	Linear SP Model
C_{Z_α}	-3.8068	-3.7248	-3.6317
$C_{Z_{\delta_e}}$	-0.8349	-0.4354	-0.4405
C_{m_α}	-0.1441	-0.1383	-0.1376
$C_{m_{\delta_e}}$	-0.5520	-0.6318	-0.5731

The derivatives C_{Z_α}, C_{m_α} and $C_{m_{\delta_e}}$ have consistent values from different models. On the other hand, $C_{Z_{\delta_e}}$ could not be matched. This is acceptable because this derivative shows the change in lift due to elevator deflection. The dynamics of F-16 are also identified by Knapp et al. [44] using closed-loop data instead of open-loop data as done in this section. In their results, the derivative Z_{δ_e} has the highest insensitivity and Cramer-Rao bound among all the longitudinal state and control derivatives.

The same procedure is applied within the flight envelope given in Figure 4.12 for seven other trim conditions marked in the plot. The trim values of elevator deflection and angle of attack at these flight conditions are given in Table 4.5.

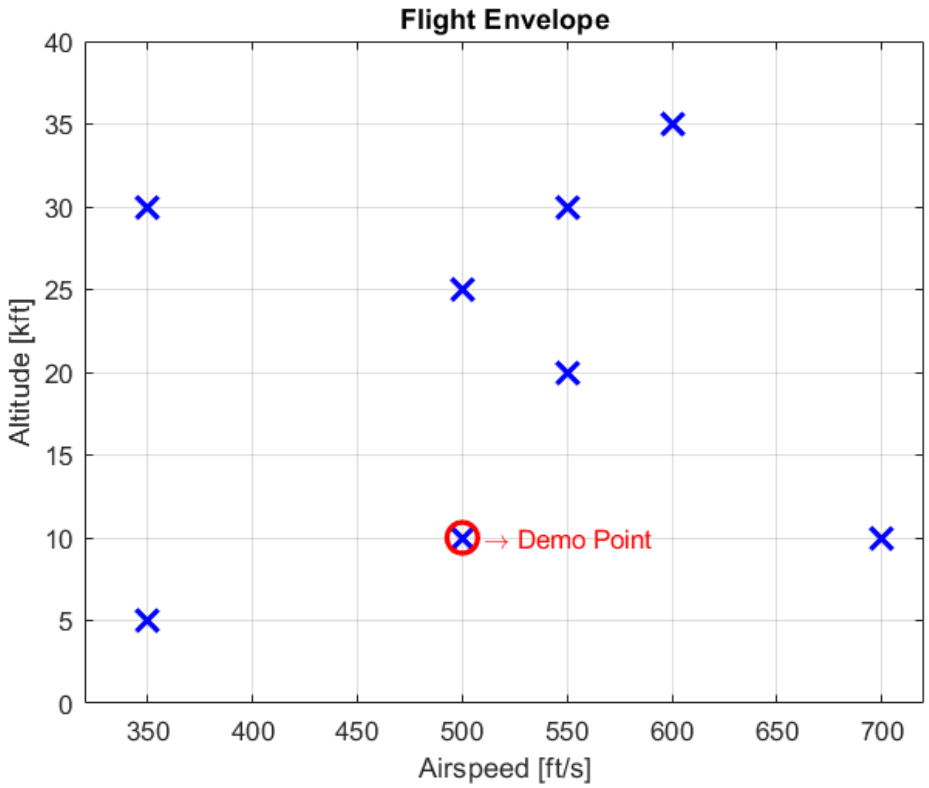

Figure 4.12: Map of Steady Flight Conditions Subjected to System Identification

Table 4.5: Trim Values of Flight Conditions Subjected to System Identification

Event Number	Altitude [kft]	V_T [ft/s]	$\alpha\,[deg]$	$\delta_e\,[deg]$
1	5	350	7.3679	-3.3723
2	10	700	1.1264	-1.6612
3	20	550	4.3223	-2.4262
4	25	500	6.8470	-3.2006
5	30	350	17.8036	-4.9558
6	30	550	6.7633	-3.1730
7	35	600	6.8837	-3.2127

In general, it is observed that time-domain match is more successful than aerodynamic parameter estimation within the envelope.

4.2 Results at Other Trim Points in the Flight Envelope

The results at various trim points are presented under related subsections, and they can be commented on as follows:

Event 1: High coherence for a great range of interval is captured, producing almost an identical match to the Linear SP transfer function. The lowest J_{rms} belongs to this event, and such a low time domain cost indicates that the identified model has high accuracy. On the other hand, the parameter accuracy is not the highest among other events.

Event 2: Coherence is almost one for even a broader frequency interval than Event 1, and a good match to the linear model is achieved in the Bode plot. This yields an excellent time-domain match, and parameter accuracy is slightly better.

Event 3: The coherence of this event has similar behaviour to Event 2. On the other hand, the magnitude plot of Figure 4.20 shows that the accuracy of the identified transfer functions at lower frequencies is lower than at higher frequencies, but only a slight increase in J_{rms} is observed because the response is dominated by short-period mode occurs at higher frequencies where the match is good. The accuracy level of the parameter estimation is similar to Event 2.

Event 4: In this event, the coherence of the angle of attack has a local dip around the natural frequency, but the values are well above the suggested boundary. Bode plots and time-domain comparison show that identified transfer function is accurate. The identified derivatives are also very close to the derivatives calculated from Linear SP model, but it is desired to obtain the key derivatives C_{m_q} and C_{Z_α} more accurately.

Event 5: The nature of the coherence function is similar to Event 4, but there are notable offsets at both channels in Bode plots given in Figure 4.26. Therefore, J_{rms} is also higher than other events. Event 2 also has similar J_{rms} values, but it is seen that the mismatch at moderate frequencies in Bode plots resulted in a considerably high offset in C_{m_q}, which affects the overall character of the response very significantly.

Event 6: A great match in the frequency domain is obtained. Even though the time-domain cost is similar to Event 5, the identified model of this event is more successful in representing the nonlinear model's characteristics. This can be related to the higher accuracy in C_{m_q}, $C_{m_{\delta e}}$.

Event 7: The match in Bode plots and parameter accuracies are similar to Event 6, which has a lower time-domain cost. Although having a comparable level of accuracies, Event 6 having a lower J_{rms} value is reasonable because the perturbation of angle of attack and pitch rate are higher in Event 6.

Overall, the results show that the accuracy of the identified models is satisfactory in both time and frequency domains, not only for a single flight condition but for various flight conditions, which indicates that the application in this study is successful.

4.2.1 Event 1

Bode plots and transfer function estimation range:

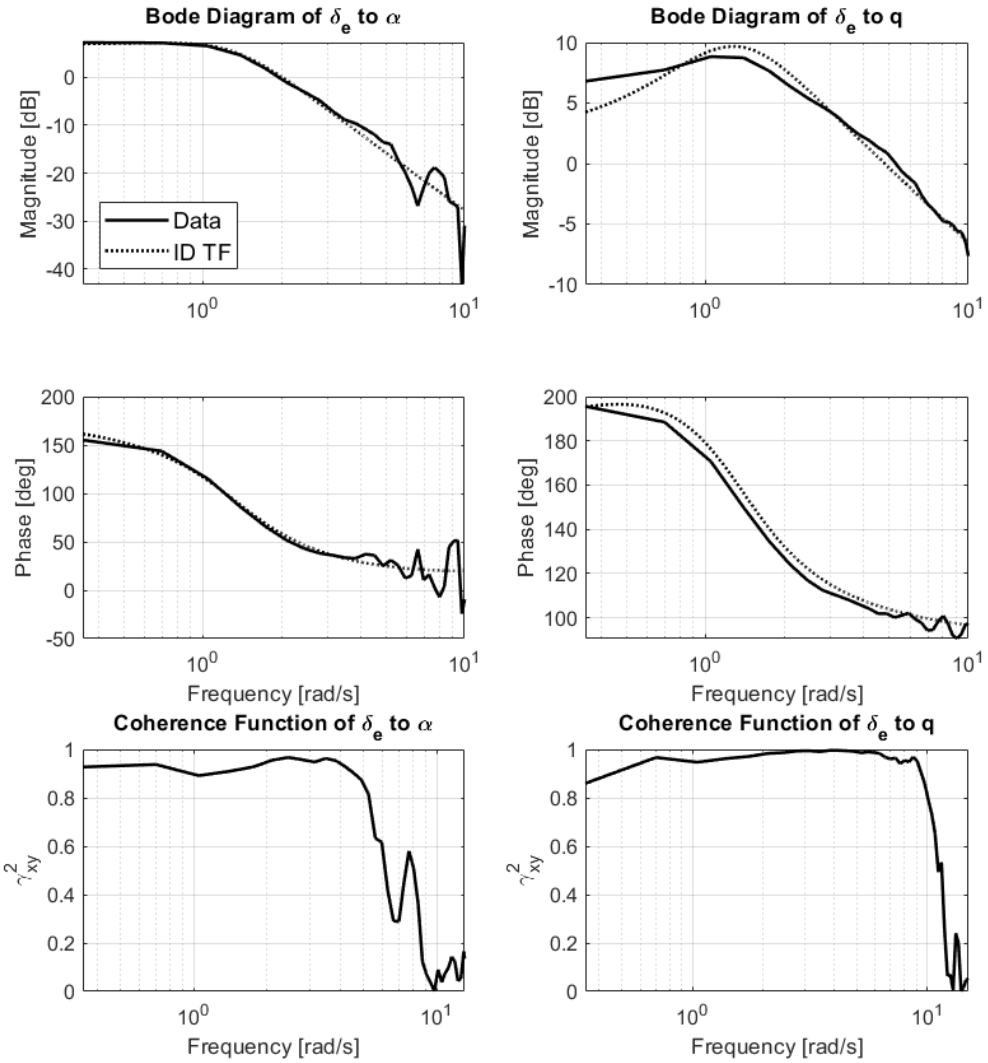

Figure 4.13: Frequency-Response and Coherence Plots of Event 1

Table 4.6: Frequency Interval with Reliable Coherence of Event 1

Frequency Response	ω_{min} [rad/s]	ω_{max} [rad/s]
$\frac{\alpha}{\delta_e}$	0.3491	5.2360
$\frac{q}{\delta_e}$	0.3491	9.7738

Identified transfer functions and natural frequency and damping of the short period mode:

$$\frac{\alpha}{\delta_e} = \frac{-0.07491s - 4.021}{s^2 + 1.652s + 1.809} \tag{4.11}$$

$$\frac{q}{\delta_e} = \frac{-4.696s - 2.404}{s^2 + 1.652s + 1.809} \tag{4.12}$$

$$\omega_n = 1.3451\ rad/s \qquad \zeta = 0.6141 \tag{4.13}$$

Bode plot comparison:

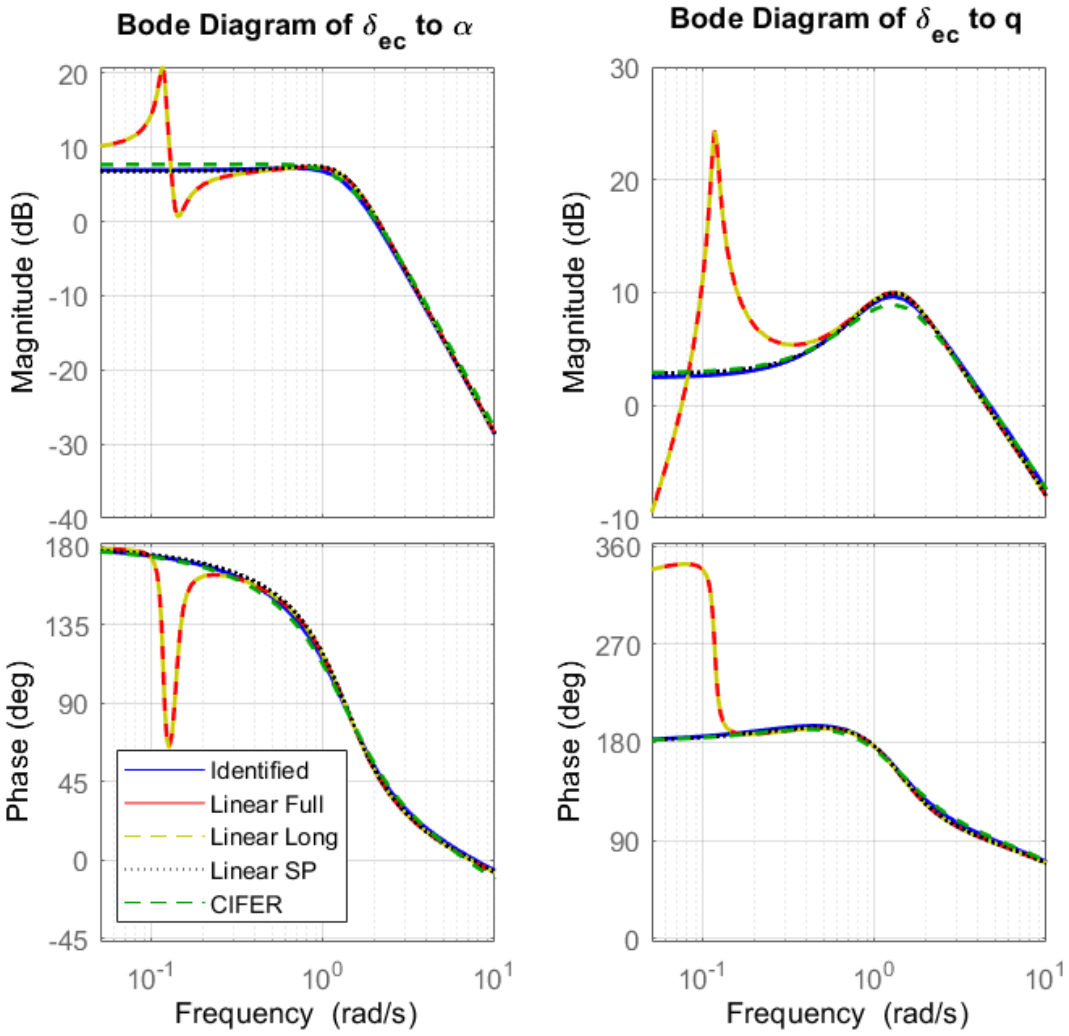

Figure 4.14: Bode Plot Comparison of Event 1

Time-domain comparison:

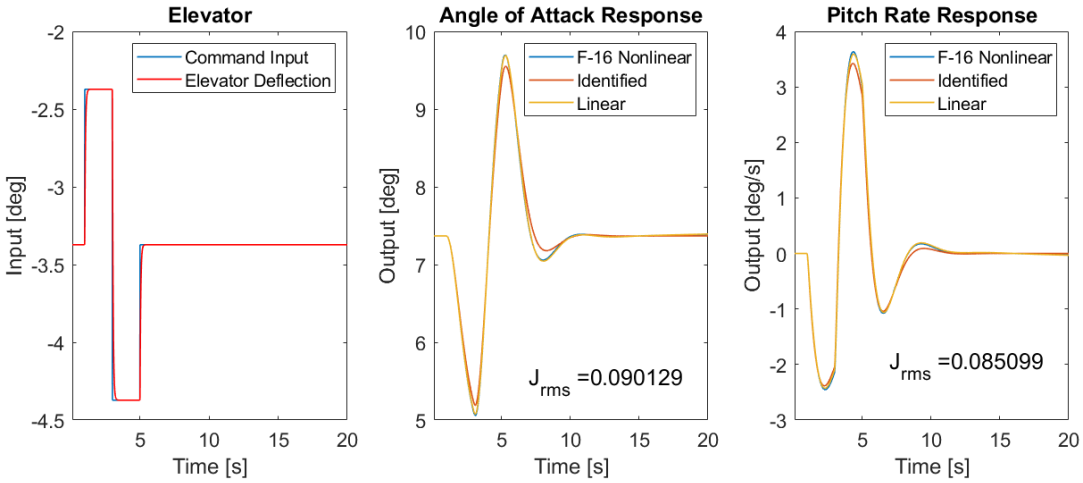

Figure 4.15: Time-Domain Comparison of Event 1

Comparison of non-dimensional derivatives:

Table 4.7: Comparison of the Derivatives C_{Z_q} and C_{m_q} of Event 1

Derivative	Identified	F-16 Database	Polynomial	Linear SP Model
C_{Z_q}	-59.1104	-30.8789	-32.0092	-31.2492
C_{m_q}	-9.0413	-5.7199	-5.8376	-7.2252

Table 4.8: Comparison of the Derivatives C_{Z_α}, $C_{Z_{\delta_e}}$, C_{m_α} and $C_{m_{\delta_e}}$ of Event 1

Derivative	Identified	Polynomial	Linear SP Model
C_{Z_α}	-3.1640	-3.4209	-3.6311
$C_{Z_{\delta_e}}$	-0.4431	-0.4354	-0.4417
C_{m_α}	-0.1891	-0.1258	-0.1886
$C_{m_{\delta_e}}$	-0.6145	-0.6346	-0.5729

4.2.2 Event 2

Bode plots and transfer function estimation range:

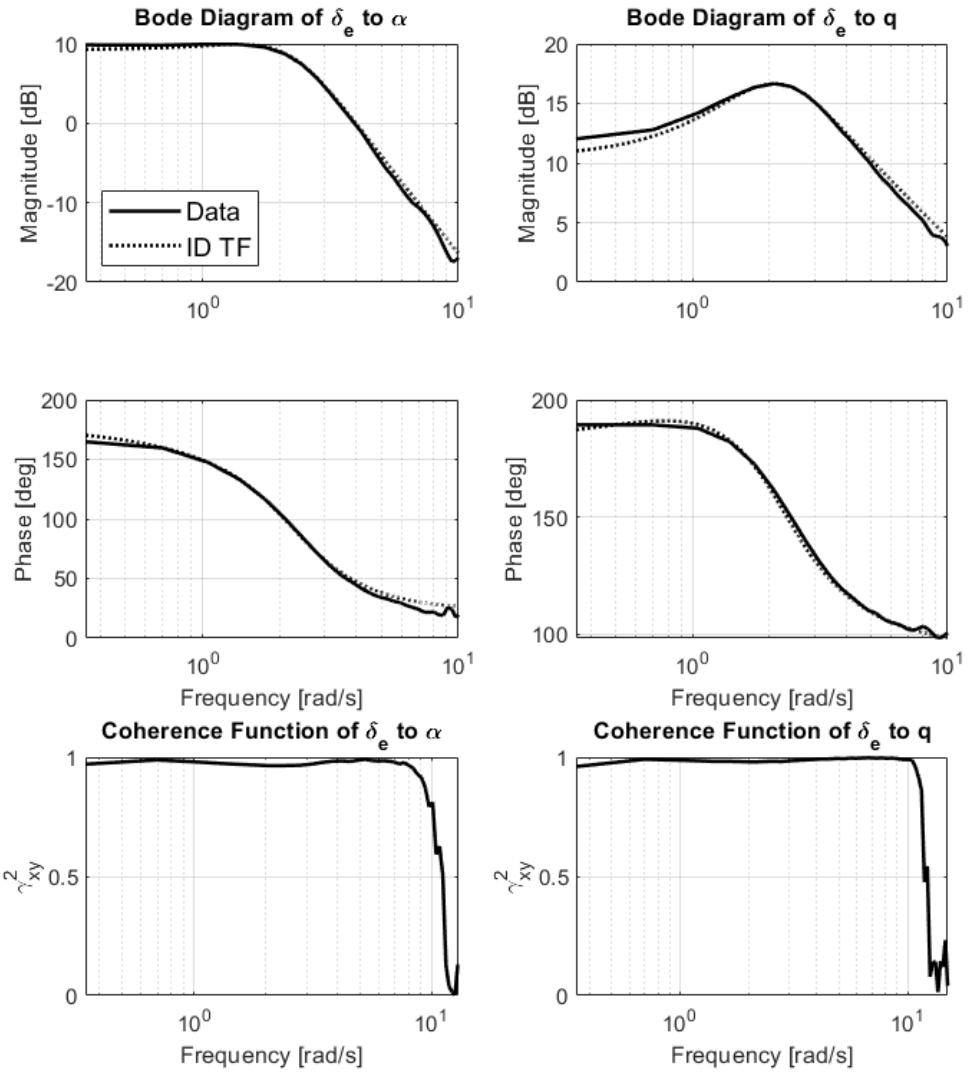

Figure 4.16: Frequency-Response and Coherence Plots of Event 2

Table 4.9: Frequency Interval with Reliable Coherence of Event 2

Frequency Response	ω_{min} [rad/s]	ω_{max} [rad/s]
$\frac{\alpha}{\delta_e}$	0.6981	9.7738
$\frac{q}{\delta_e}$	0.6981	11.8682

Identified transfer functions and natural frequency and damping of the short period mode:

$$\frac{\alpha}{\delta_e} = \frac{-0.3166s - 14.58}{s^2 + 2.498s + 5.03} \tag{4.14}$$

$$\frac{q}{\delta_e} = \frac{-15.1s - 16.93}{s^2 + 2.498s + 5.03} \tag{4.15}$$

$$\omega_n = 2.2428\ rad/s \qquad \zeta = 0.5568 \tag{4.16}$$

Bode plot comparison:

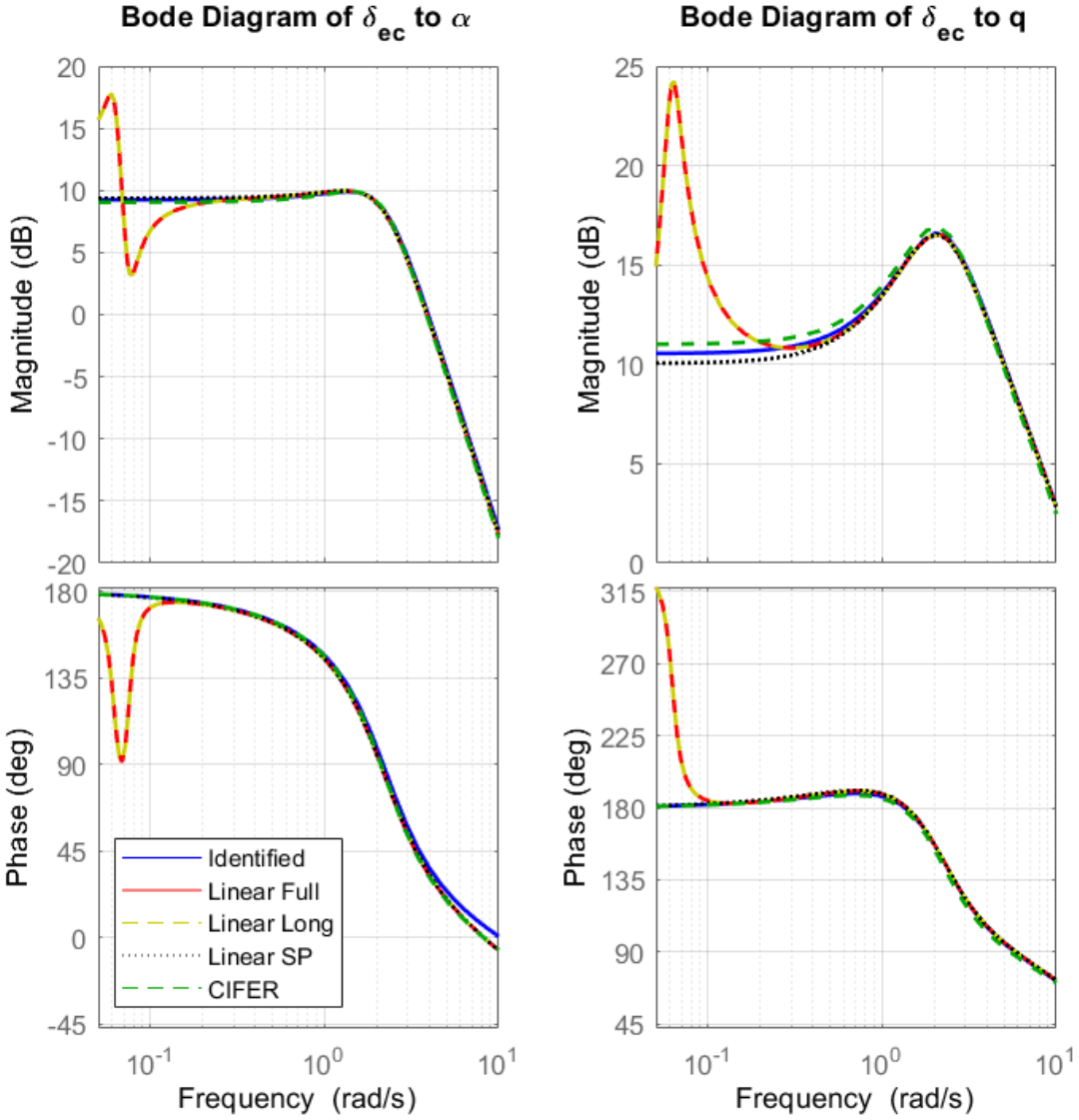

Figure 4.17: Bode Plot Comparison of Event 2

Time-domain comparison:

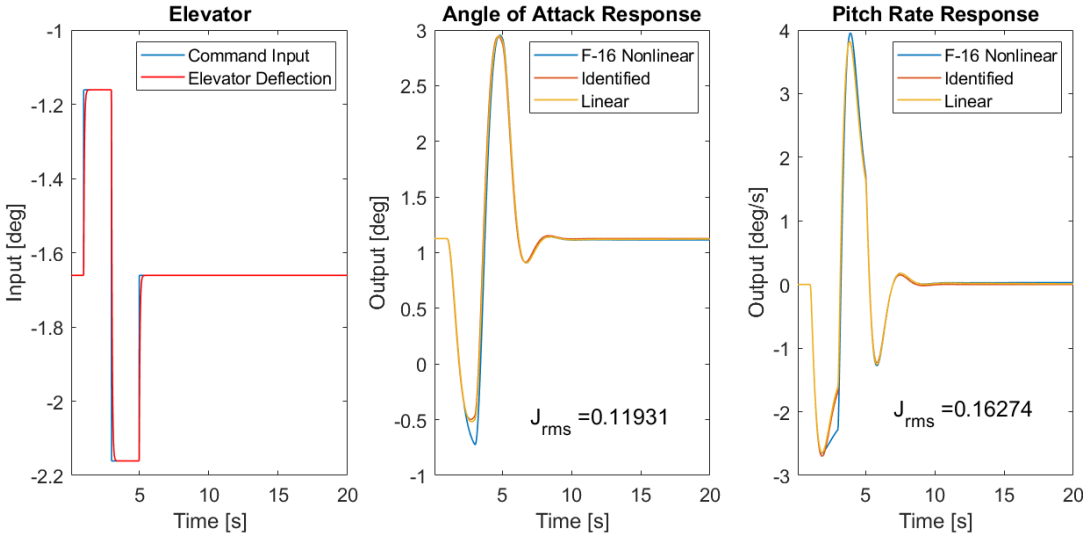

Figure 4.18: Time-Domain Comparison of Event 2

Comparison of non-dimensional derivatives:

Table 4.10: Comparison of the Derivatives C_{Z_q} and C_{m_q} of Event 1

Derivative	Identified	F-16 Database	Polynomial	Linear SP Model
C_{Z_q}	-26.4965	-29.7253	-31.2398	-29.5140
C_{m_q}	-6.1422	-5.4732	-5.2413	-6.7211

Table 4.11: Comparison of the Derivatives C_{Z_α}, $C_{Z_{\delta_e}}$, C_{m_α} and $C_{m_{\delta_e}}$ of Event 1

Derivative	Identified	Polynomial	Linear SP Model
C_{Z_α}	-4.1419	-4.0353	-3.6296
$C_{Z_{\delta_e}}$	-1.0940	-0.4354	-0.4377
C_{m_α}	-0.1415	-0.1530	-0.1370
$C_{m_{\delta_e}}$	-0.5772	-0.6281	-0.5755

4.2.3 Event 3

Bode plots and transfer function estimation range:

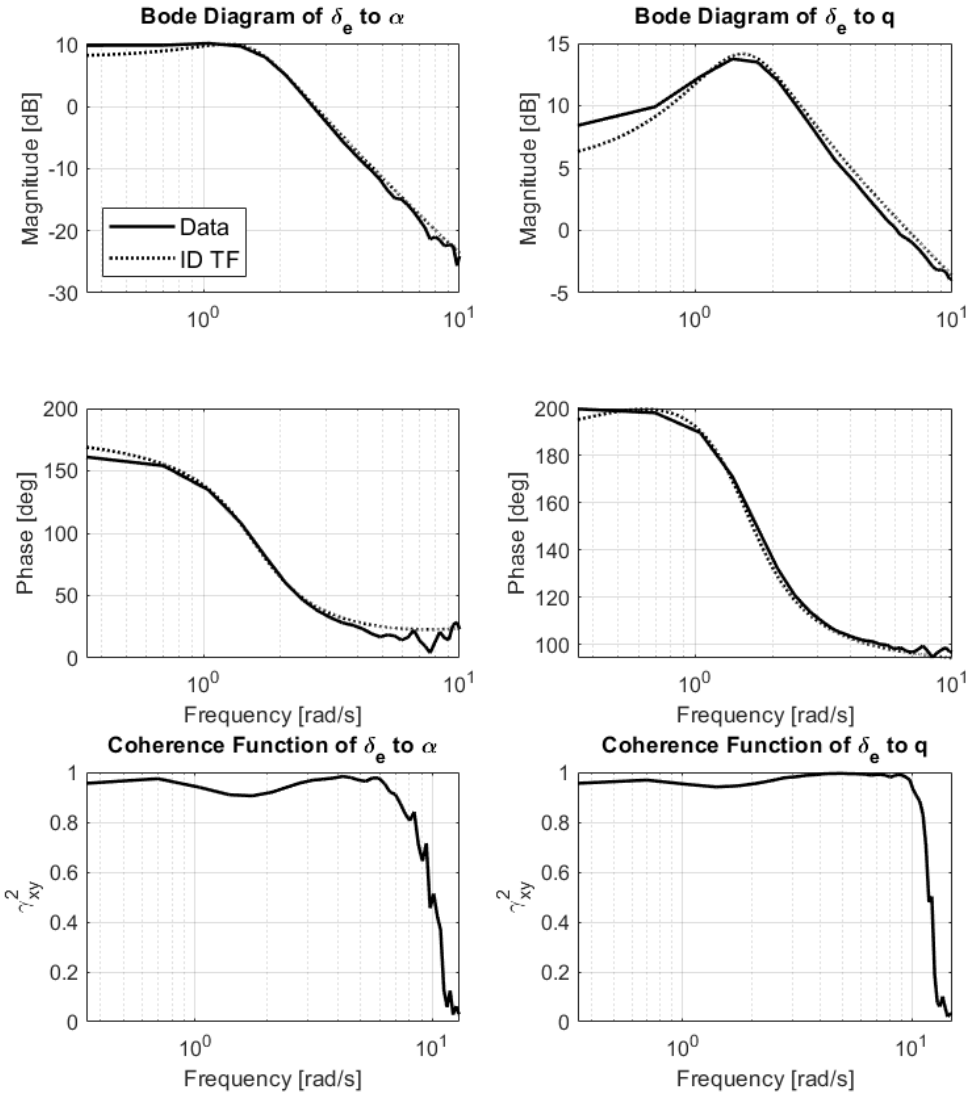

Figure 4.19: Frequency-Response and Coherence Plots of Event 3

Table 4.12: Frequency Interval with Reliable Coherence of Event 3

Frequency Response	ω_{min} [rad/s]	ω_{max} [rad/s]
$\frac{\alpha}{\delta_e}$	1.0472	8.3776
$\frac{q}{\delta_e}$	0.6981	10.4720

Identified transfer functions and natural frequency and damping of the short period mode:

$$\frac{\alpha}{\delta_e} = \frac{-0.07491s - 4.021}{s^2 + 1.652s + 1.809} \tag{4.17}$$

$$\frac{q}{\delta_e} = \frac{-4.696s - 2.404}{s^2 + 1.652s + 1.809} \tag{4.18}$$

$$\omega_n = 1.5771\ rad/s \qquad \zeta = 0.4405 \tag{4.19}$$

Bode plot comparison:

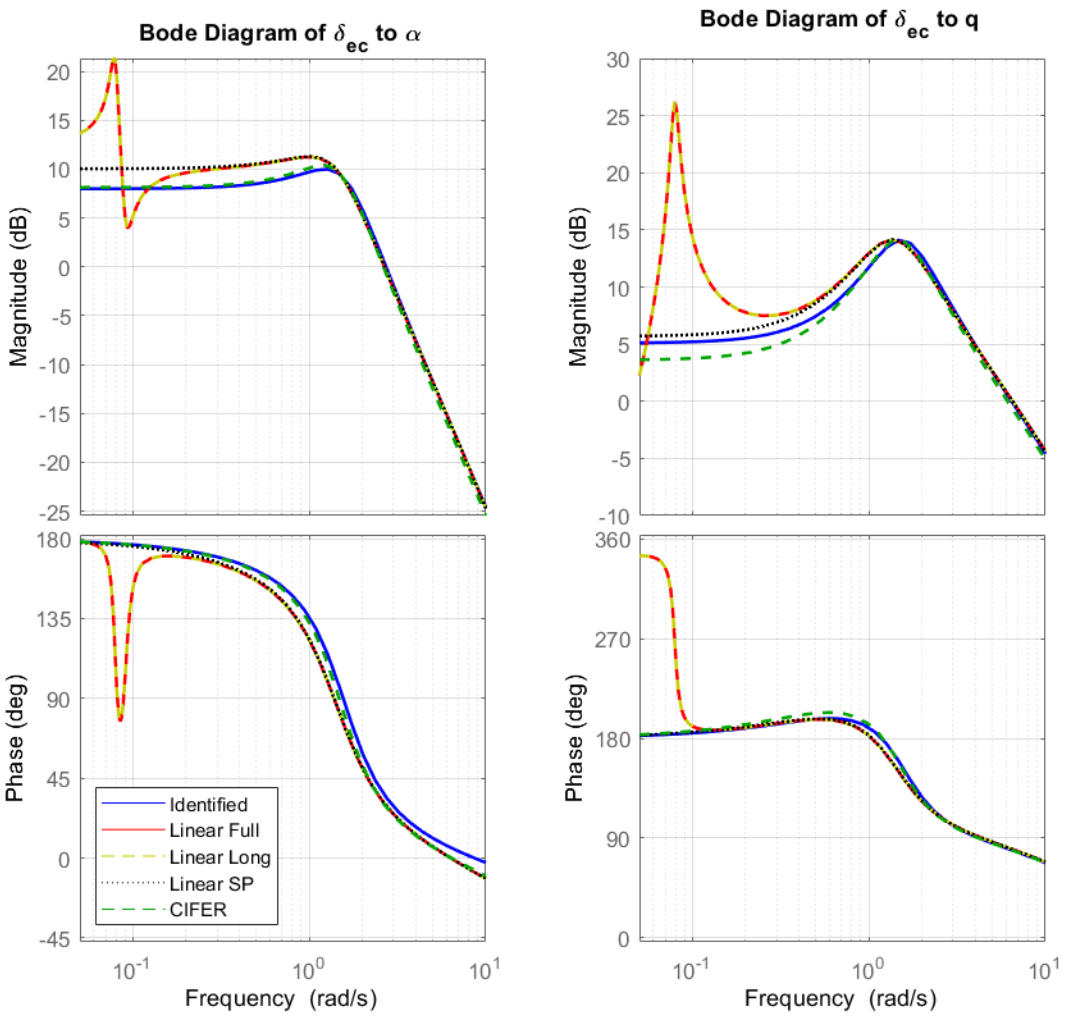

Figure 4.20: Bode Plot Comparison of Event 3

Time-domain comparison:

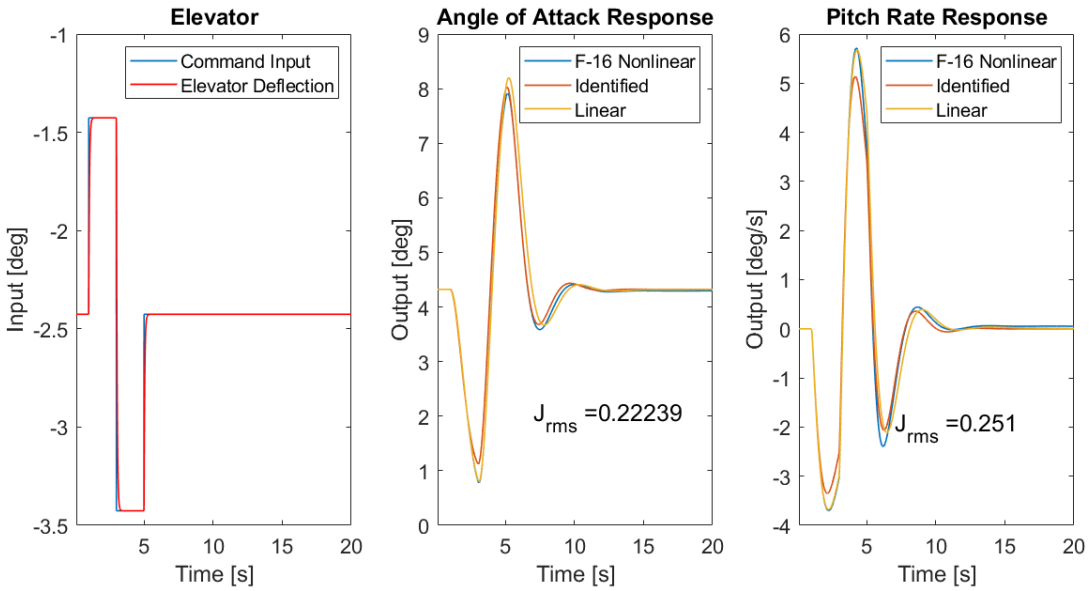

Figure 4.21: Time-Domain Comparison of Event 3

Comparison of non-dimensional derivatives:

Table 4.13: Comparison of the Derivatives C_{Z_q} and C_{m_q} of Event 3

Derivative	Identified	F-16 Database	Polynomial	Linear SP Model
C_{Z_q}	-32.4028	-30.3645	-32.0738	-31.1399
C_{m_q}	-5.3549	-5.4541	-5.5484	-6.8265

Table 4.14: Comparison of the Derivatives C_{Z_α}, $C_{Z_{\delta_e}}$, C_{m_α} and $C_{m_{\delta_e}}$ of Event 3

Derivative	Identified	Polynomial	Linear SP Model
C_{Z_α}	-4.5562	-3.6517	-3.6344
$C_{Z_{\delta_e}}$	-1.0697	-0.4354	-0.4415
C_{m_α}	-0.1822	-0.1350	-0.1379
$C_{m_{\delta_e}}$	-0.5560	-0.6325	-0.5729

4.2.4 Event 4

Bode plots and transfer function estimation range:

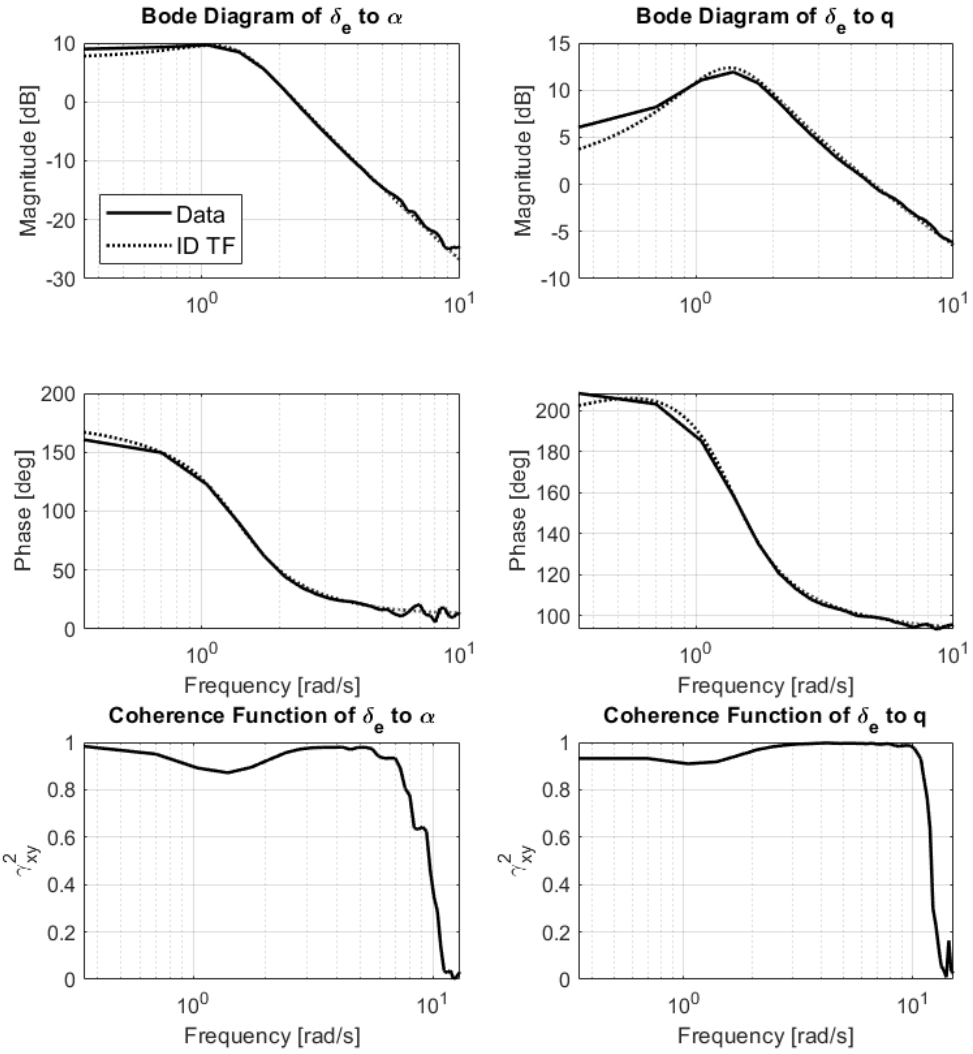

Figure 4.22: Frequency-Response and Coherence Plots of Event 4

Table 4.15: Frequency Interval with Reliable Coherence of Event 4

Frequency Response	ω_{min} [rad/s]	ω_{max} [rad/s]
$\frac{\alpha}{\delta_e}$	1.0472	6.9813
$\frac{q}{\delta_e}$	0.3491	9.7738

Identified transfer functions and natural frequency and damping of the short period mode:

$$\frac{\alpha}{\delta_e} = \frac{-0.05542s - 4.464}{s^2 + 1.193s + 1.895} \tag{4.20}$$

$$\frac{q}{\delta_e} = \frac{-4.661s - 2.285}{s^2 + 1.193s + 1.895} \tag{4.21}$$

$$\omega_n = 1.3767\ rad/s \qquad \zeta = 0.4334 \tag{4.22}$$

Bode plot comparison:

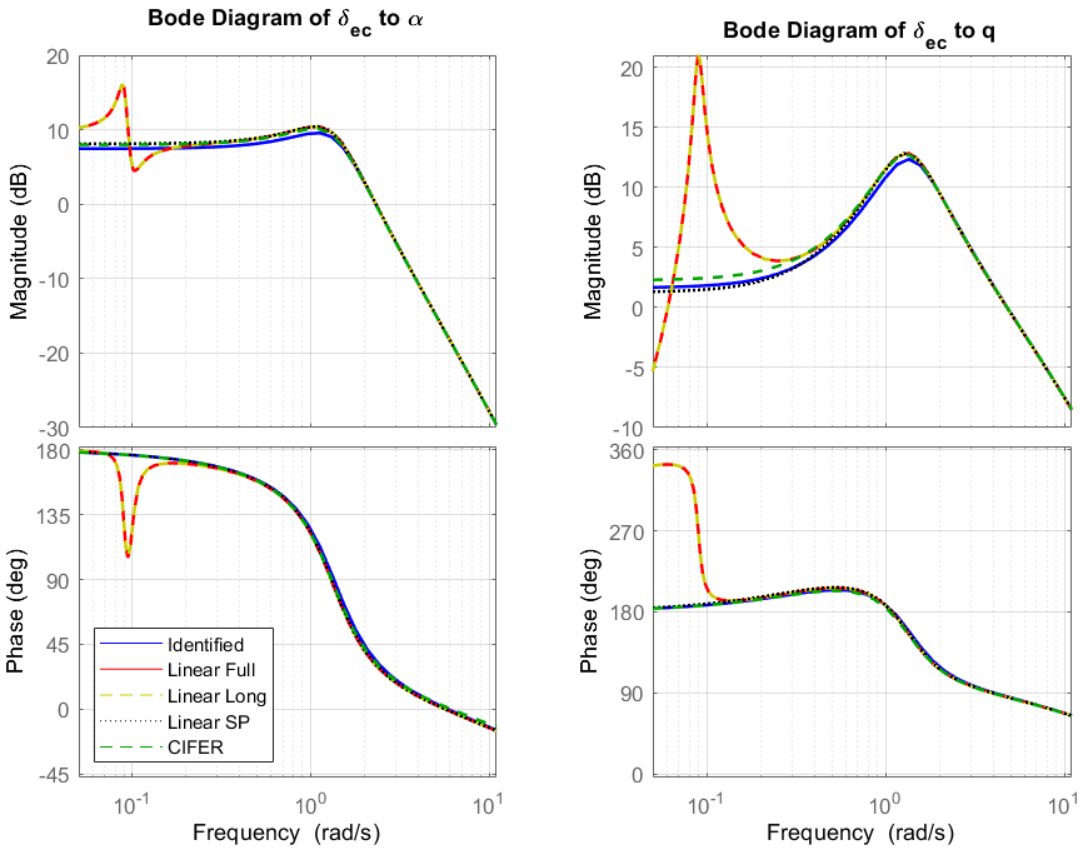

Figure 4.23: Bode Plot Comparison of Event 4

Time-domain comparison:

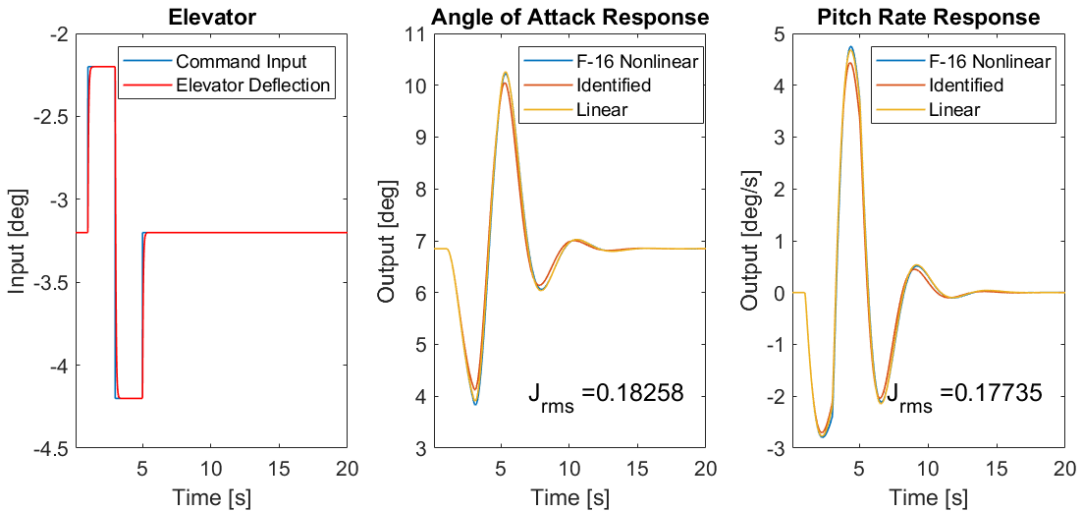

Figure 4.24: Time-Domain Comparison of Event 4

Comparison of non-dimensional derivatives:

Table 4.16: Comparison of the Derivatives C_{Z_q} and C_{m_q} of Event 4

Derivative	Identified	F-16 Database	Polynomial	Linear SP Model
C_{Z_q}	-35.5089	-28.7543	-31.8708	-31.3791
C_{m_q}	-7.4596	-6.1337	-5.7924	-7.1602

Table 4.17: Comparison of the Derivatives C_{Z_α}, $C_{Z_{\delta_e}}$, C_{m_α} and $C_{m_{\delta_e}}$ of Event 4

Derivative	Identified	Polynomial	Linear SP Model
C_{Z_α}	-4.0626	-3.4524	-3.6428
$C_{Z_{\delta_e}}$	-0.4419	-0.4354	-0.4430
C_{m_α}	-0.2011	-0.1269	-0.1894
$C_{m_{\delta_e}}$	-0.5755	-0.6344	-0.5742

4.2.5 Event 5

Bode plots and transfer function estimation range:

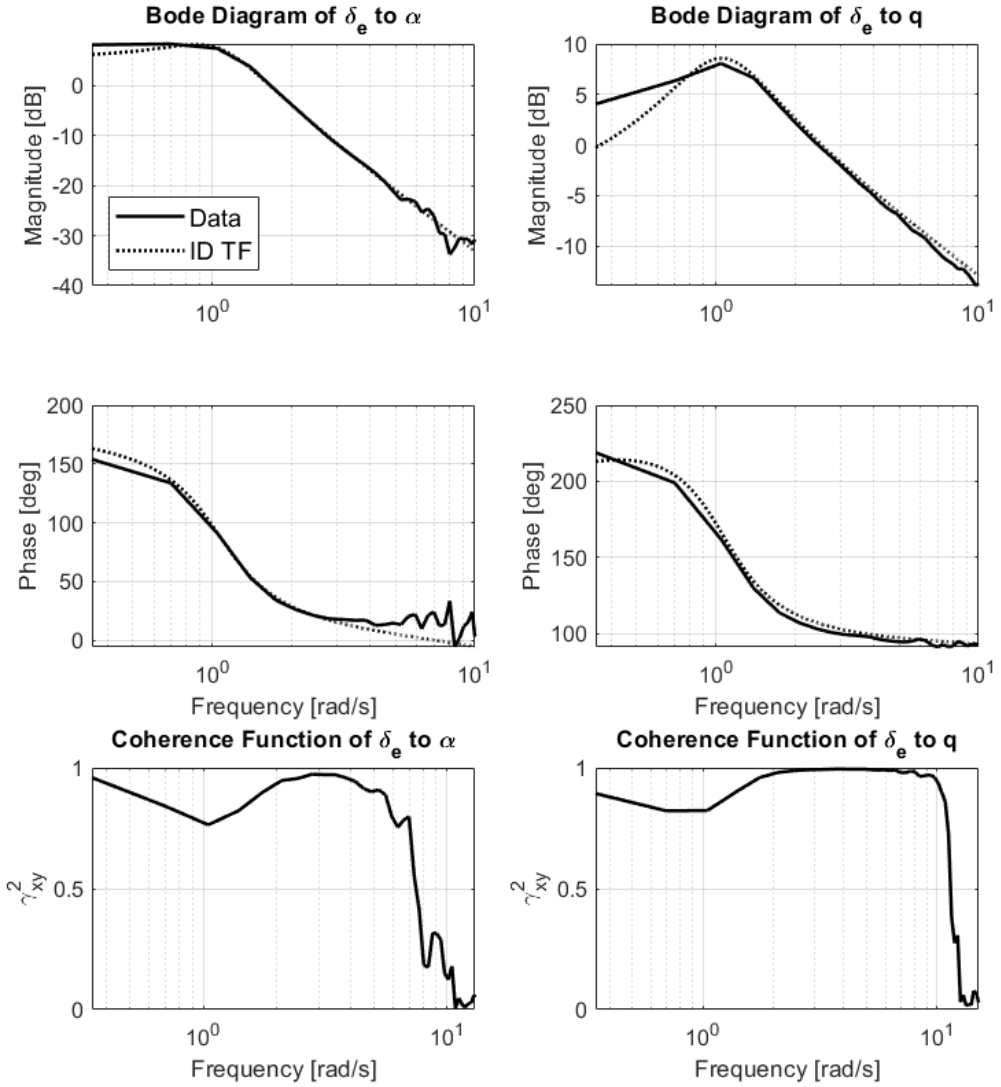

Figure 4.25: Frequency-Response and Coherence Plots of Event 5

Table 4.18: Frequency Interval with Reliable Coherence of Event 5

Frequency Response	ω_{min} [rad/s]	ω_{max} [rad/s]
$\frac{\alpha}{\delta_e}$	1.0472	6.9813
$\frac{q}{\delta_e}$	0.3491	10.4720

Identified transfer functions and natural frequency and damping of the short period mode:

$$\frac{\alpha}{\delta_e} = \frac{0.03835s - 2.167}{s^2 + 0.8669s + 1.137} \tag{4.23}$$

$$\frac{q}{\delta_e} = \frac{-2.243s - 0.6682}{s^2 + 0.8669s + 1.137} \tag{4.24}$$

$$\omega_n = 1.0664\ rad/s \qquad \zeta = 0.4065 \tag{4.25}$$

Bode plot comparison:

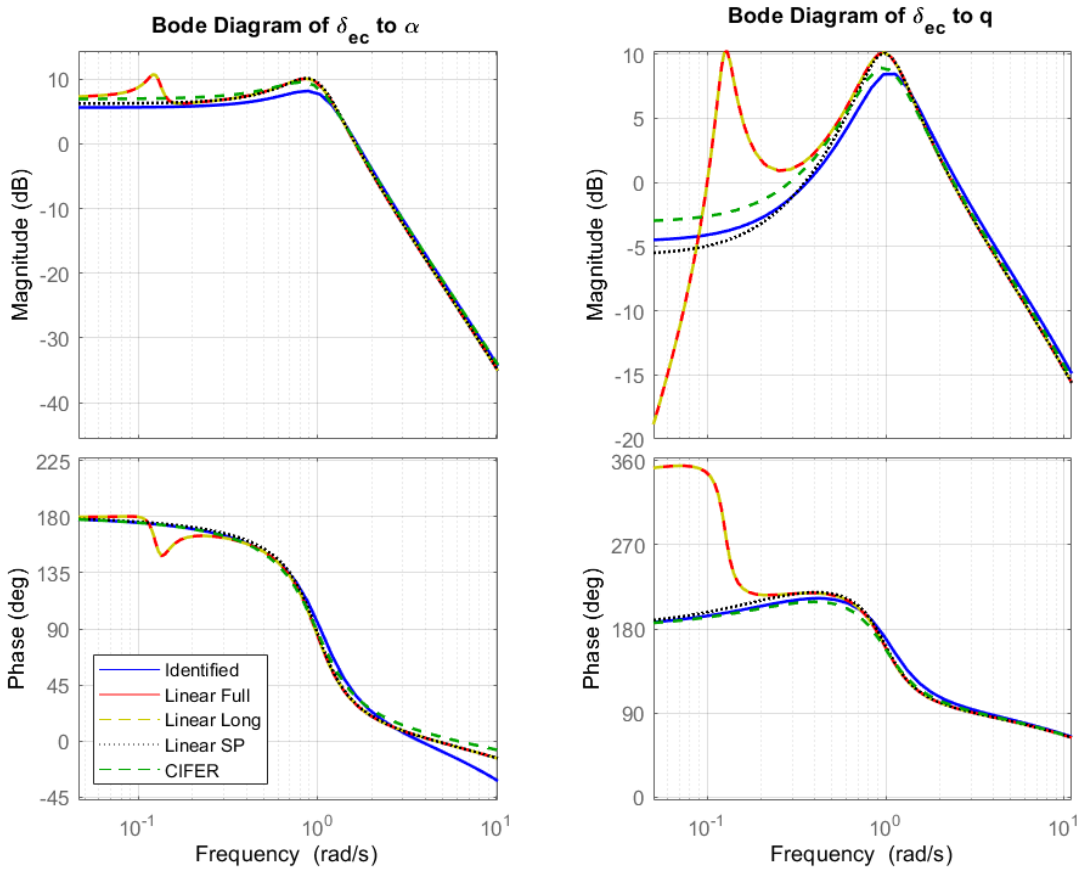

Figure 4.26: Bode Plot Comparison of Event 5

Time-domain comparison:

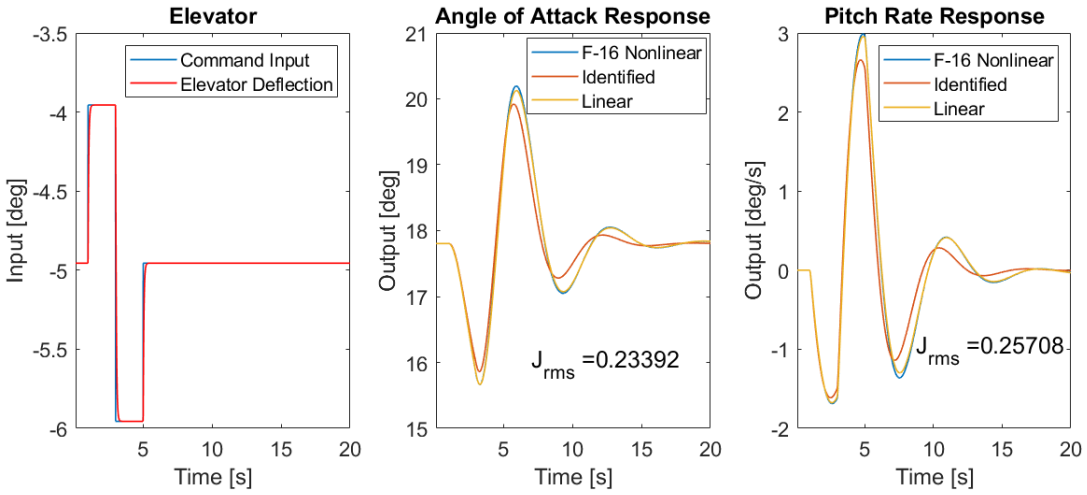

Figure 4.27: Time-Domain Comparison of Event 5

Comparison of non-dimensional derivatives:

Table 4.19: Comparison of the Derivatives C_{Z_q} and C_{m_q} of Event 5

Derivative	Identified	F-16 Database	Polynomial	Linear SP Model
C_{Z_q}	-20.1830	-28.7543	-28.3386	-28.5695
C_{m_q}	-10.9375	-6.1337	-6.1304	-7.5795

Table 4.20: Comparison of the Derivatives C_{Z_α}, $C_{Z_{\delta_e}}$, C_{m_α} and $C_{m_{\delta_e}}$ of Event 5

Derivative	Identified	Polynomial	Linear SP Model
C_{Z_α}	-3.8312	-3.2083	-3.5578
$C_{Z_{\delta_e}}$	0.5233	-0.4354	-0.4236
C_{m_α}	-0.3007	-0.1306	-0.2732
$C_{m_{\delta_e}}$	-0.6770	-0.6224	-0.6222

4.2.6 Event 6

Bode plots and transfer function estimation range:

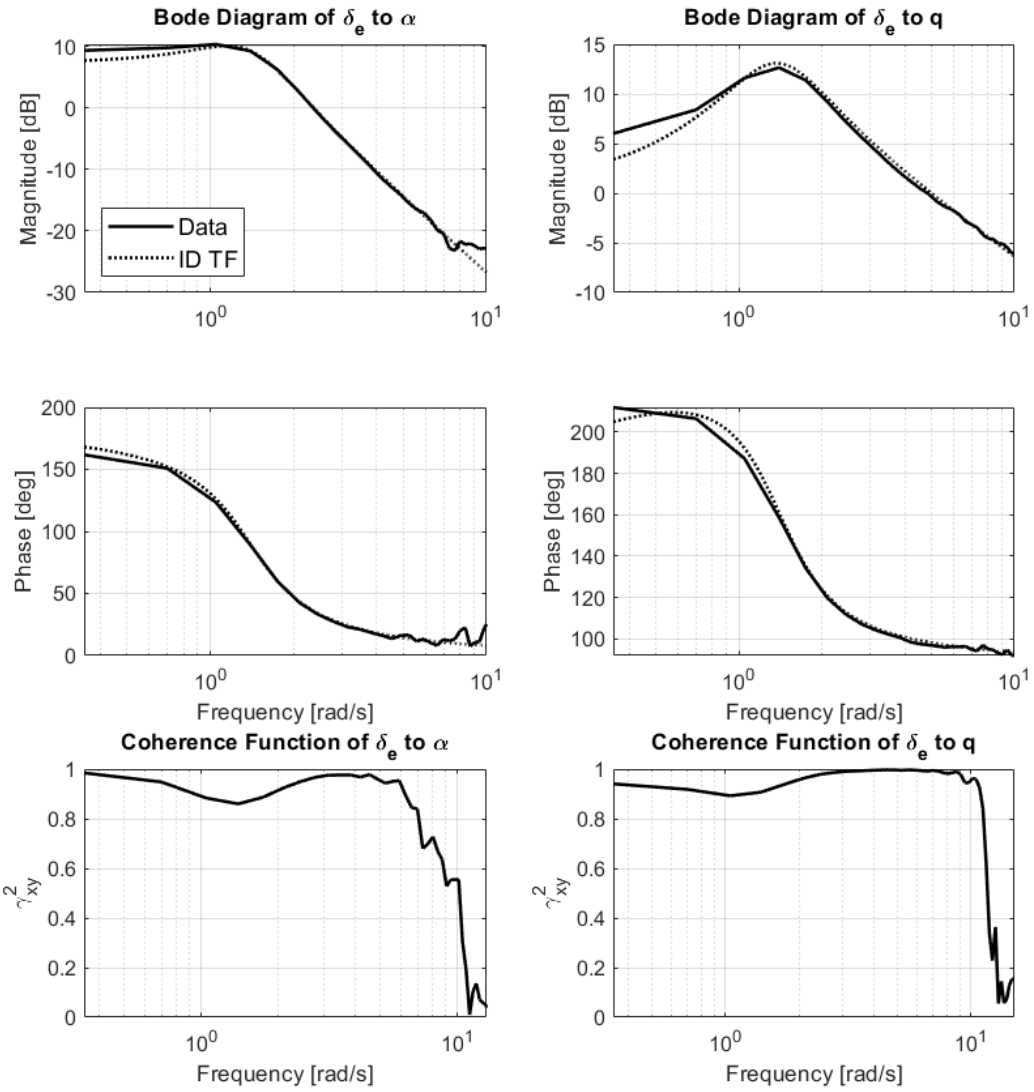

Figure 4.28: Frequency-Response and Coherence Plots of Event 6

Table 4.21: Frequency Interval with Reliable Coherence of Event 6

Frequency Response	ω_{min} [rad/s]	ω_{max} [rad/s]
$\frac{\alpha}{\delta_e}$	1.3963	6.9813
$\frac{q}{\delta_e}$	0.3491	9.7738

Identified transfer functions and natural frequency and damping of the short period mode:

$$\frac{\alpha}{\delta_e} = \frac{-0.01356s - 4.523}{s^2 + 1.103s + 1.935} \tag{4.26}$$

$$\frac{q}{\delta_e} = \frac{-4.727s - 2.191}{s^2 + 1.103s + 1.935} \tag{4.27}$$

$$\omega_n = 1.3912\ rad/s \qquad \zeta = 0.3966 \tag{4.28}$$

Bode plot comparison:

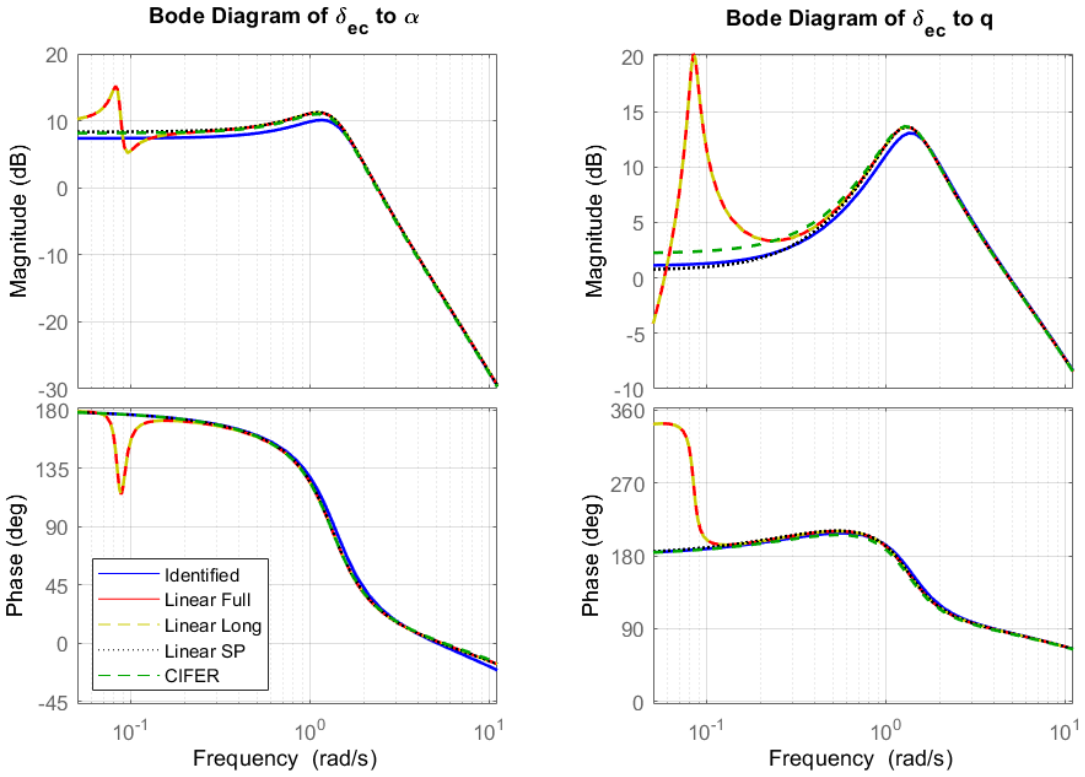

Figure 4.29: Bode Plot Comparison of Event 6

Time-domain comparison:

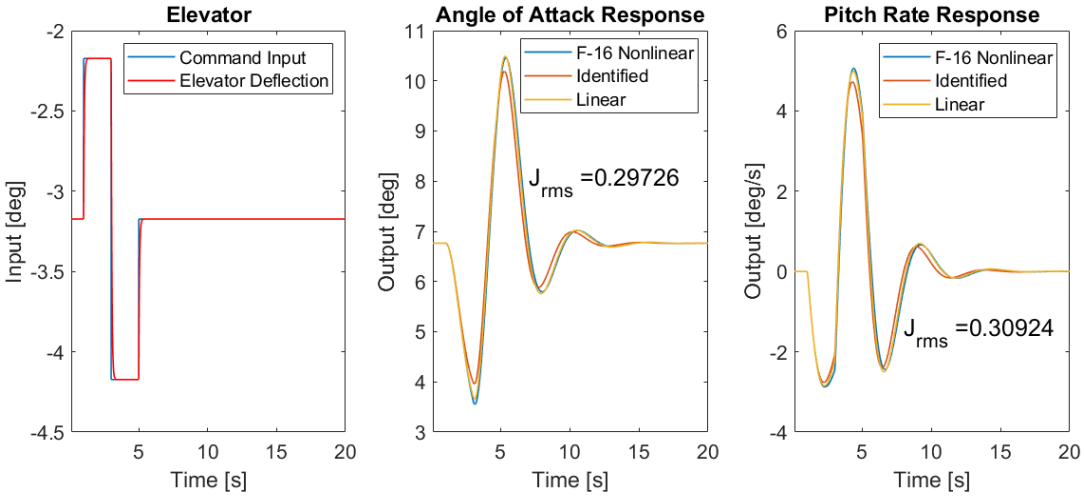

Figure 4.30: Time-Domain Comparison of Event 6

Comparison of non-dimensional derivatives:

Table 4.22: Comparison of the Derivatives C_{Z_q} and C_{m_q} of Event 6

Derivative	Identified	F-16 Database	Polynomial	Linear SP Model
C_{Z_q}	-37.8864	-30.7821	-31.8864	-31.3849
C_{m_q}	-7.5425	-5.6510	-5.7850	-7.1463

Table 4.23: Comparison of the Derivatives C_{Z_α}, $C_{Z_{\delta_e}}$, C_{m_α} and $C_{m_{\delta_e}}$ of Event 6

Derivative	Identified	Polynomial	Linear SP Model
C_{Z_α}	-4.0668	-3.4577	-3.6430
$C_{Z_{\delta_e}}$	-0.1178	-0.4354	-0.4429
C_{m_α}	-0.2096	-0.1271	-0.1894
$C_{m_{\delta_e}}$	-0.5776	-0.6344	-0.5741

4.2.7 Event 7

Bode plots and transfer function estimation range:

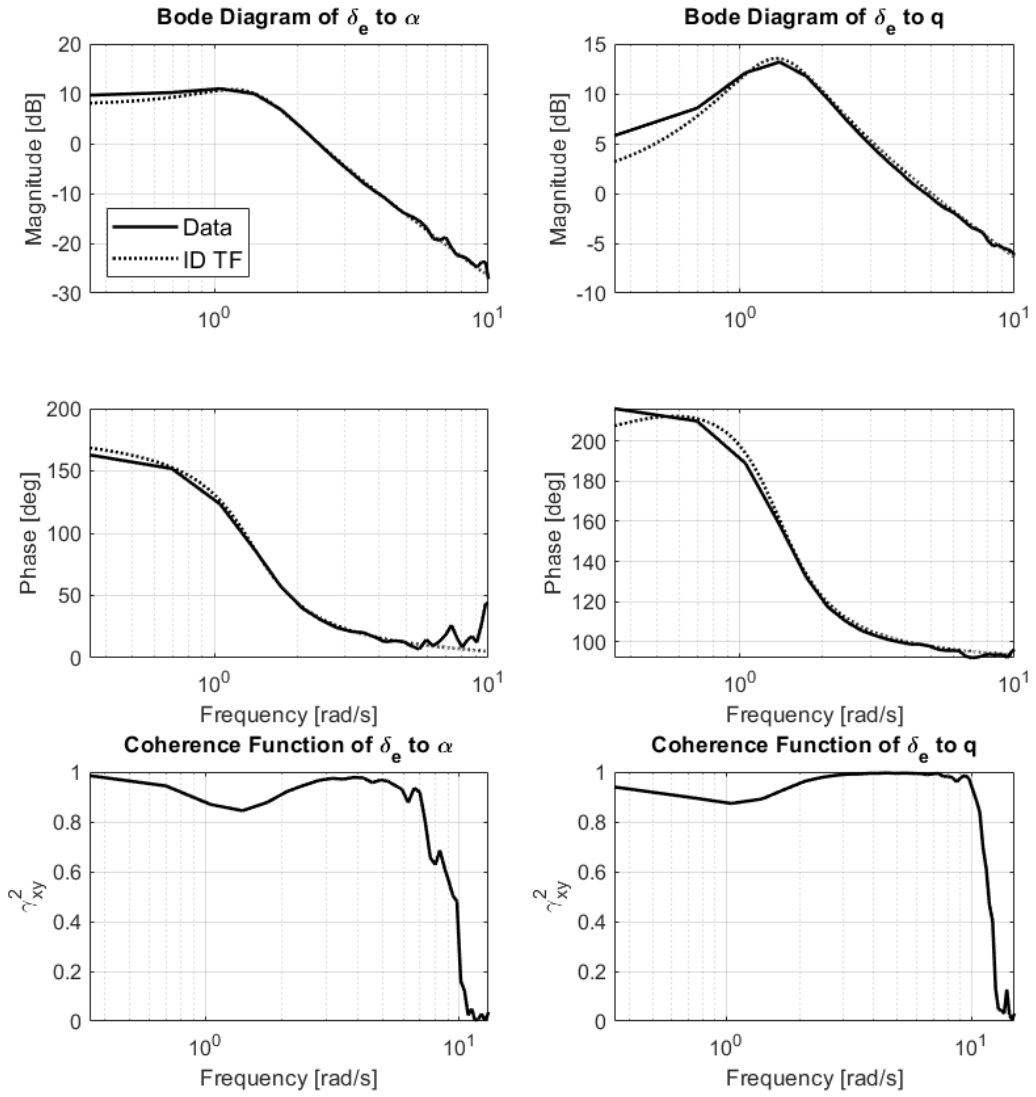

Figure 4.31: Frequency-Response and Coherence Plots of Event 7

Table 4.24: Frequency Interval with Reliable Coherence of Event 7

Frequency Response	ω_{min} [rad/s]	ω_{max} [rad/s]
$\frac{\alpha}{\delta_e}$	1.3963	8.7266
$\frac{q}{\delta_e}$	0.3491	10.4720

Identified transfer functions and natural frequency and damping of the short period mode:

$$\frac{\alpha}{\delta_e} = \frac{0.005474s - 4.612}{s^2 + 1.037s + 1.895} \tag{4.29}$$

$$\frac{q}{\delta_e} = \frac{-4.706s - 2.026}{s^2 + 1.037s + 1.895} \tag{4.30}$$

$$\omega_n = 1.3766\ rad/s \qquad \zeta = 0.3767 \tag{4.31}$$

Bode plot comparison:

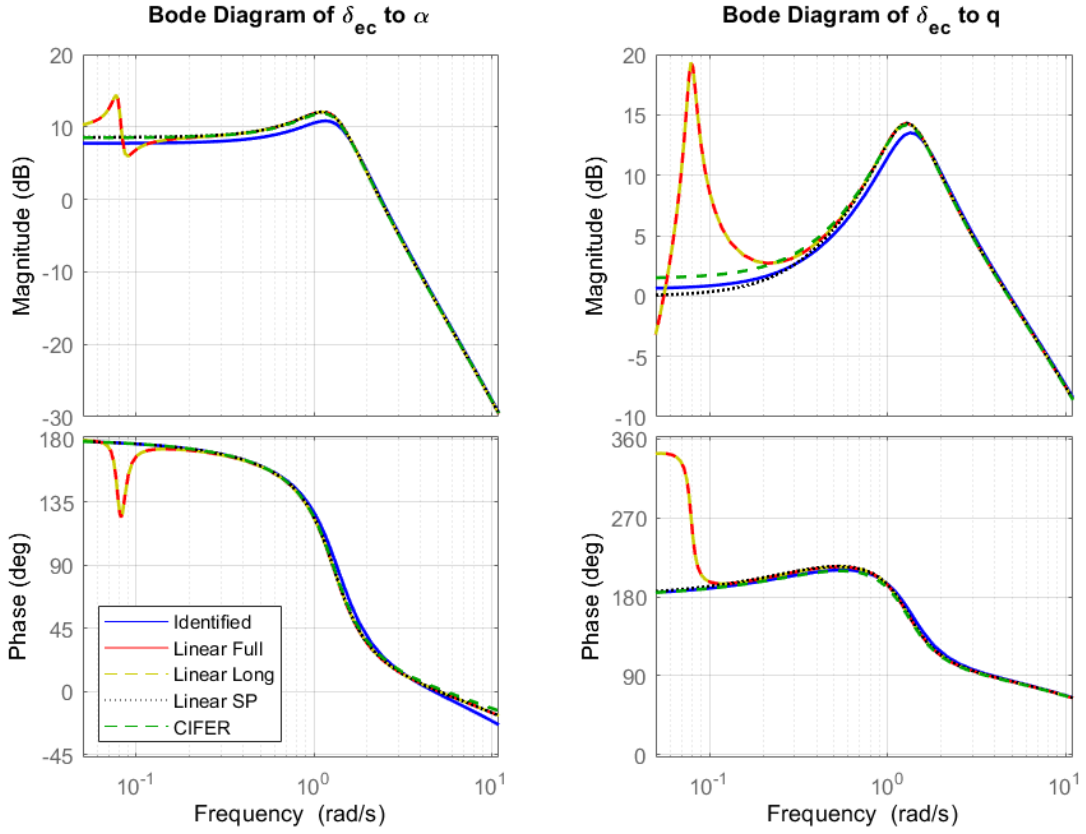

Figure 4.32: Bode Plot Comparison of Event 7

Time-domain comparison:

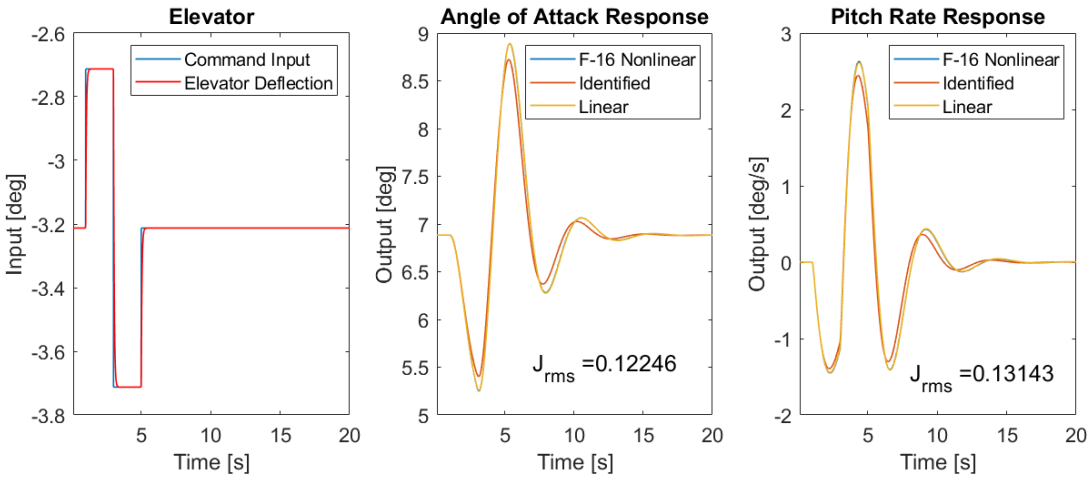

Figure 4.33: Time-Domain Comparison of Event 7

Comparison of non-dimensional derivatives:

Table 4.25: Comparison of the Derivatives C_{Z_q} and C_{m_q} of Event 7

Derivative	Identified	F-16 Database	Polynomial	Linear SP Model
C_{Z_q}	-19.5437	-30.8014	-31.8639	-31.3712
C_{m_q}	-7.9969	-5.6647	-5.7850	-7.1651

Table 4.26: Comparison of the Derivatives C_{Z_α}, $C_{Z_{\delta_e}}$, C_{m_α} and $C_{m_{\delta_e}}$ of Event 7

Derivative	Identified	Polynomial	Linear SP Model
C_{Z_α}	-4.1191	-3.4501	-3.6422
$C_{Z_{\delta_e}}$	0.0526	-0.4354	-0.4429
C_{m_α}	-0.2066	-0.1268	-0.1893
$C_{m_{\delta_e}}$	-0.5834	-0.6345	-0.5741

4.3 Case Studies

It is shown that the application of the frequency-response identification procedure has produced satisfactory results using open-loop data to identify short-period bare-airframe dynamics. Using the same method, two other cases are investigated. First, the consequences of neglecting the phugoid mode while identifying the short-period mode are investigated. The same open-loop data of the demo point is used for the analysis. The second case is the identification of short-period bare-airframe dynamics using closed-loop data.

4.3.1 Investigation of the Phugoid Mode Involvement

The goal was to identify the short-period dynamics of the aircraft by second-order transfer functions. As a result, the short-period and the phugoid mode, which occurs at lower frequencies, cannot be captured simultaneously by a second-order transfer function. Since elevator excitation also triggers the phugoid mode, a higher-order fit to the frequency-response data is attempted to see if a better model can be found when the phugoid mode is also included.

The transfer functions α/δ_e and θ/δ_e that include both modes are given by Roskam [45] in forth order form as follows:

$$\frac{\alpha}{\delta_e} = \frac{A_\alpha s^3 + B_\alpha s^2 + C_\alpha s + D_\alpha}{As^4 + Bs^3 + Cs^2 + Ds + E} \tag{4.32}$$

$$\frac{\theta}{\delta_e} = \frac{A_\theta s^2 + B_\theta s + C_\theta}{As^4 + Bs^3 + Cs^2 + Ds + E} \tag{4.33}$$

The transfer function q/δ_e can be written as $s\ \theta/\delta_e$. This requires the placement of a fixed zero at the origin while estimating the transfer function. However, this was not possible with the employed fitting algorithm, which reduces the accuracy of the fit. To overcome this problem, the frequency-response of θ is used instead of q and the estimated transfer function θ/δ_e is multiplied with s to obtain q/δ_e such that:

$$\frac{q}{\delta_e} = \frac{A_\theta s^3 + B_\theta s^2 + C_\theta s}{As^4 + Bs^3 + Cs^2 + Ds + E} \tag{4.34}$$

A good fit to phugoid mode requires data at lower frequencies, which a larger window size can achieve. Therefore, the window length is readjusted while using the same time-history data of the demo event. It should be noted that, in this case, a longer window length is no longer within the recommended bounds, but fitting a fourth-order transfer function while keeping the window length the same also did not yield a better model. Based on the Bode plots of the linearised system, it is decided that the window length should be equal to the recording time to capture the low frequencies where the phugoid model is observable. On the other hand, the coherence function becomes useless if one window is used. As already mentioned, coherence is a guide to evaluating data quality. Thus, the lack of coherence function is a significant drawback and requires a blind trial and error process while determining the fit frequency range. Experimenting with different frequency ranges, it is observed that even the best fit among all trials cannot correctly capture the nature of aircraft at the lower frequencies. Some good matches are achieved by two unrelated poles, not by complex conjugate pairs as desired. Although they may have a closer match, such estimations are not acceptable as they lack the phugoid mode's physical sense. The final decision about the most suitable frequency interval for the fitting is given in Table 4.27 for the same demo point (10 kft trim altitude with 500 ft/s trim airspeed). The frequency-response data contain 72 and 101 data points in the selected frequency ranges.

Table 4.27: Frequency Interval with Reliable Coherence of the Phugoid Mode Investigation Case

Frequency Response	ω_{min} [rad/s]	ω_{max} [rad/s]
$\frac{\alpha}{\delta_e}$	0.1396	5.2360
$\frac{\theta}{\delta_e}$	0.2793	7.3304

The identified transfer functions with corresponding short-period and phugoid natural frequencies and damping ratios are found as follows:

$$\frac{\alpha}{\delta_e} = \frac{-0.47025(s+13.09)(s^2+0.04862s+0.0166)}{(s^2+0.00472s+0.02004)(s^2+1.487s+2.264)} \tag{4.35}$$

$$\frac{q}{\delta_e} = \frac{-7.9672s(s-0.7458)(s+0.2082)}{(s^2+0.00472s+0.02004)(s^2+1.487s+2.264)} \tag{4.36}$$

$$\omega_{n,sp} = 1.5047\ rad/s \qquad \zeta_{n,sp} = 0.4941 \tag{4.37}$$

$$\omega_{n,ph} = 0.1416\ rad/s \qquad \zeta_{n,ph} = 0.0167 \tag{4.38}$$

The comparison of the identified transfer functions with the linear model and the results of CIFER are given in Figure 4.34.

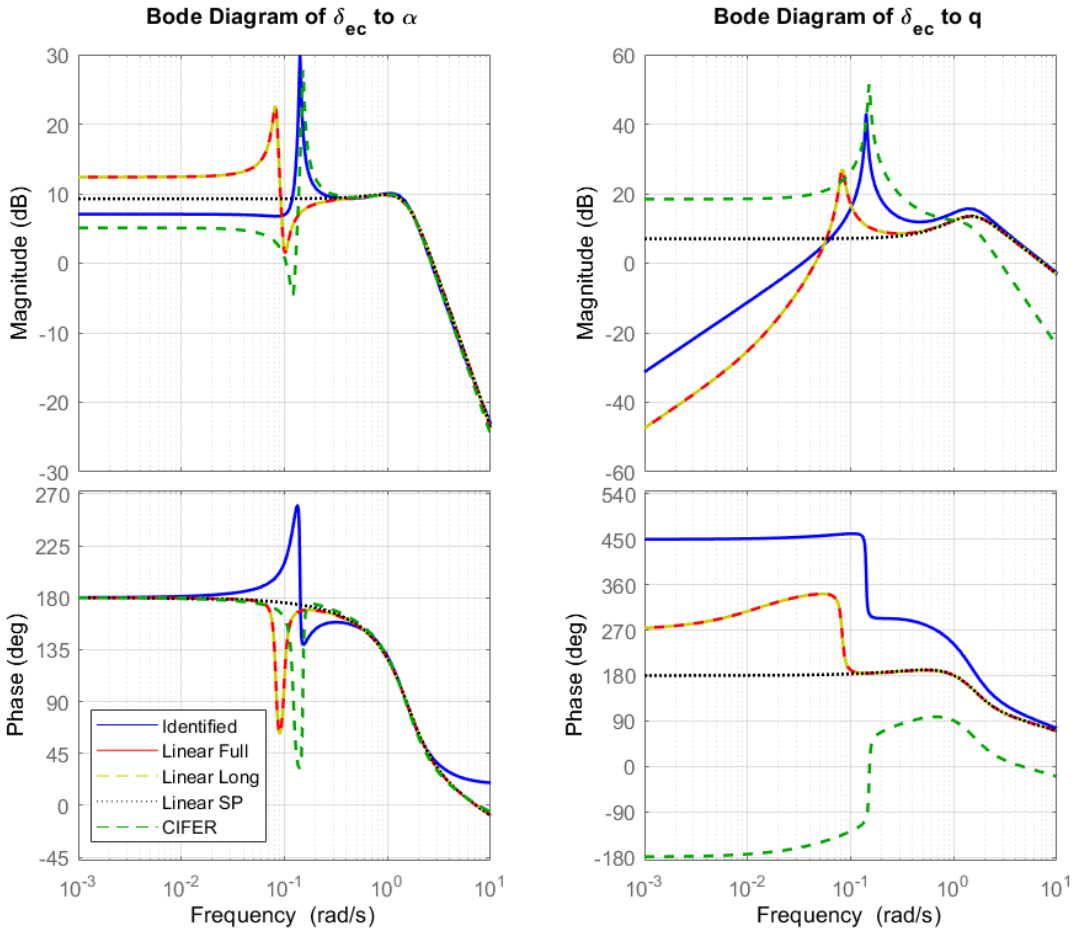

Figure 4.34: Bode Plot Comparison of Phugoid Mode Identification

The match of identified model and linear model is still great at the higher frequencies where the short-period mode is dominant. However, it is seen that the discrepancy at lower frequencies is unacceptable, which indicates that the data is insufficient to make any conclusion on the degree of involvement of the phugoid mode. In addition, CIFER also could not fit an acceptable model to the data. Since the coherence function is not available, it is difficult to judge if the amount and quality of data at lower

frequencies are sufficient to approximate the phugoid mode. In addition, adequate excitation of the mode is suspicious even though phugoid oscillations were visually observed in the θ response. Berger et al. [43] also note that phugoid mode identification is difficult due to the lack of good data at low frequencies, which require longer time-history records. This also causes the speed stability derivatives to be insensitive and hard to determine. To sum up, compensating for phugoid involvement in the response is not possible or credible when short-period identification is performed. Phugoid, if needed, must be separately identified using proper techniques and with inputs that can sufficiently excite the mode.

4.3.2 Bare-Airframe Identification Using Closed-Loop Data

To this point, bare-airframe identification was performed using open-loop (SCAS-off) data. Tischler and Remple [17] suggest that open-loop data should be preferred, if possible, as SCAS supresses low-frequency content, which may lead lower accuracy at that frequency range. Still, identification of bare-airframe dynamics is possible when SCAS is active. In this section, a controller is designed using the identified model of the demo point, and bare-airframe dynamics are identified from closed-loop data.

4.3.2.1 Controller Design

A classical pitch-rate demand system is designed, and the bare-airframe dynamics identified from open-loop data are used for the plant dynamics. The controller architecture is presented in Figure 4.35.

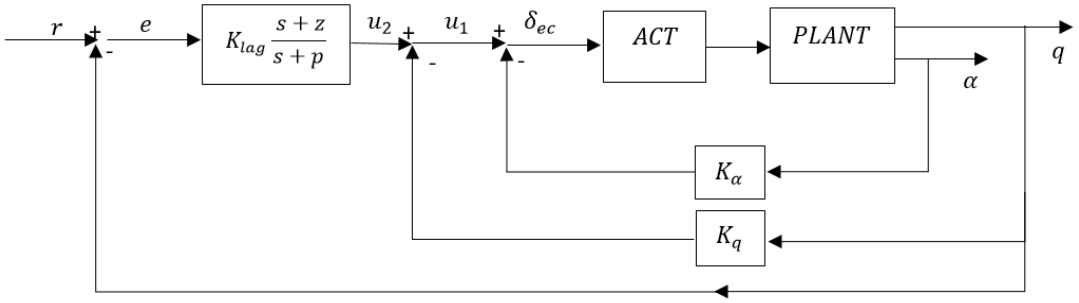

Figure 4.35: Architecture of the Controller

Angle of attack feedback and the pitch rate feedback at the inner loop improve pitch stiffness and pitch damping by augmenting C_{m_α} and C_{m_q} derivatives, respectively. The gain K_α is selected as -0.5, which yields poles to be located at ω_n = 2.46 rad/s and ζ = 0.34, where the stability margins are 28 dB and 70 degrees, as shown in Figure 4.36. Then, the gain K_q is taken as -0.5, which sufficiently damps the short-period poles with a slight increase in the natural frequency. As seen in Figure 4.37, the poles are now located at ω_n = 3.42 rad/s and ζ = 0.99, and the system has an infinite gain margin, and the phase margin is 96 degrees. The damping might seem unnecessarily high, but the integrator gain further reduces the damping. Hence, slightly higher

damping is targeted in the inner-loop design. The integrator is needed to achieve zero steady-state error; however, obtaining an ideal steady-state response with sufficient stability margins is not easy. Closing the inner loops, it is observed that the plant is challenging due to the left-hand plane zero near the origin. Because the zero is near the origin, a branch is formed that connects the integrator to the zero. The mode created along this branch is slow compared to the short period mode and is apparent in time response. The mode can be negated by increasing the integrator gain, which, in effect, moves this slow pole closer to zero, but the short period mode also moves toward the unstable plane. As a result, both damping and stability margins suffer. An alternative is to replace the integrator with a lag compensator at the cost of steady-state error. This design can potentially remove the slow mode by placing the compensator pole closer to the plant's zero. Therefore, a lag compensator is designed where the steady-state error of 10% is targeted, and the compensator zero is placed to provide a phase margin of 60 degrees, giving $K_{lag} = 0.7$, $z = 8$ and $p = 0.4$, as shown in Figure 4.38.

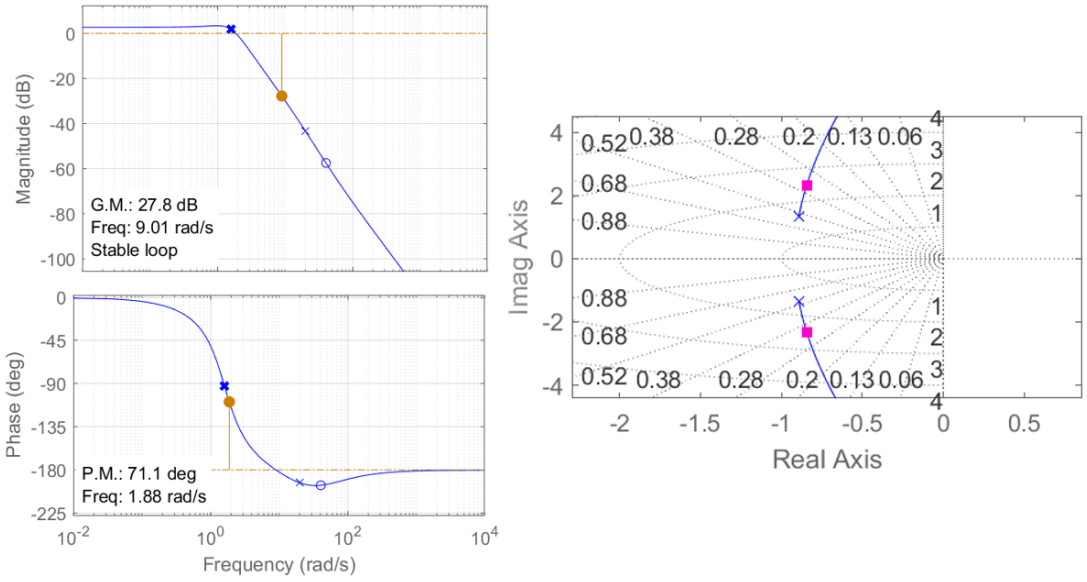

Figure 4.36: Angle of Attack Inner Loop Closure

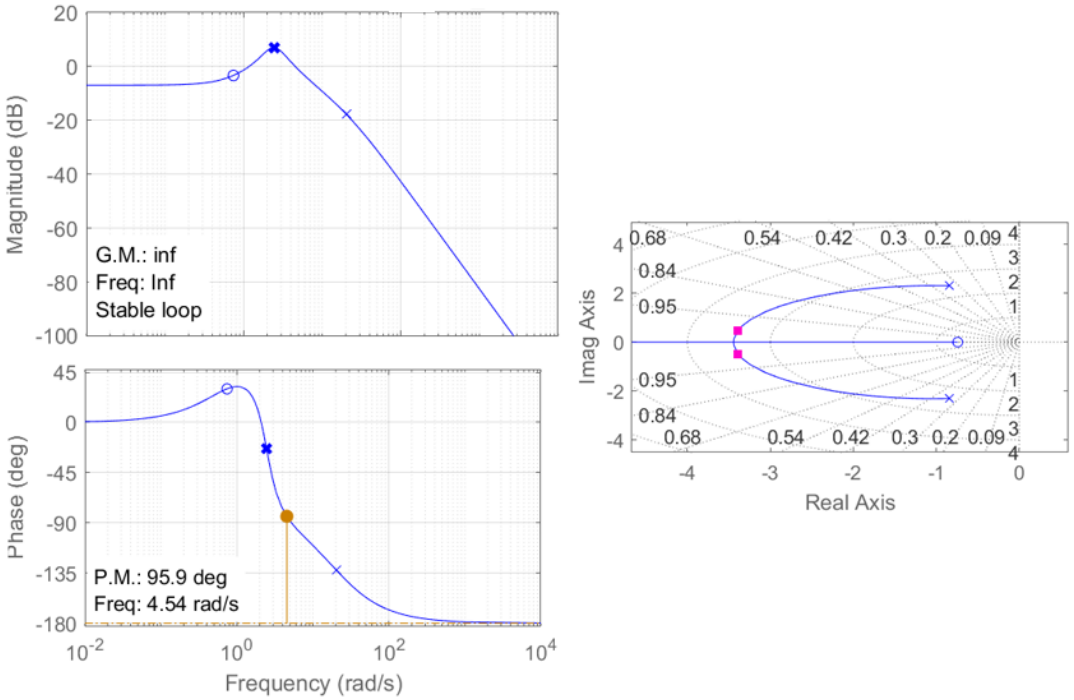

Figure 4.37: Pitch Rate Inner Loop Closure

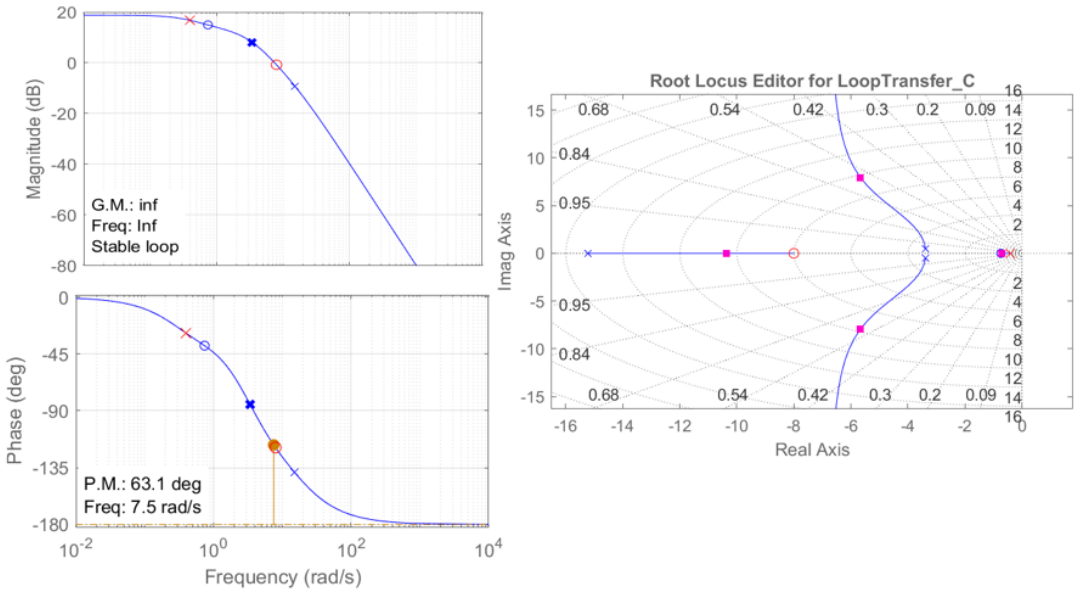

Figure 4.38: Lag Compensator Loop Closure

4.3.2.2 Identification and Results

Trimming the aircraft at demo point flight conditions, sweep input is given as q_{ref} input to the system. It is observed that the input design should be updated for closed-loop identification as the record length of 90 seconds is found to be too long to keep the aircraft at initial trim point. The airspeed deviation during the 90-second test was around 70 m/s, indicating that the aircraft drifts too far apart from the initial trim conditions. Such a large airspeed deviation is present when pitch rate response is around 5-10 deg/s. The time histories of this case are given in Figure 4.39.

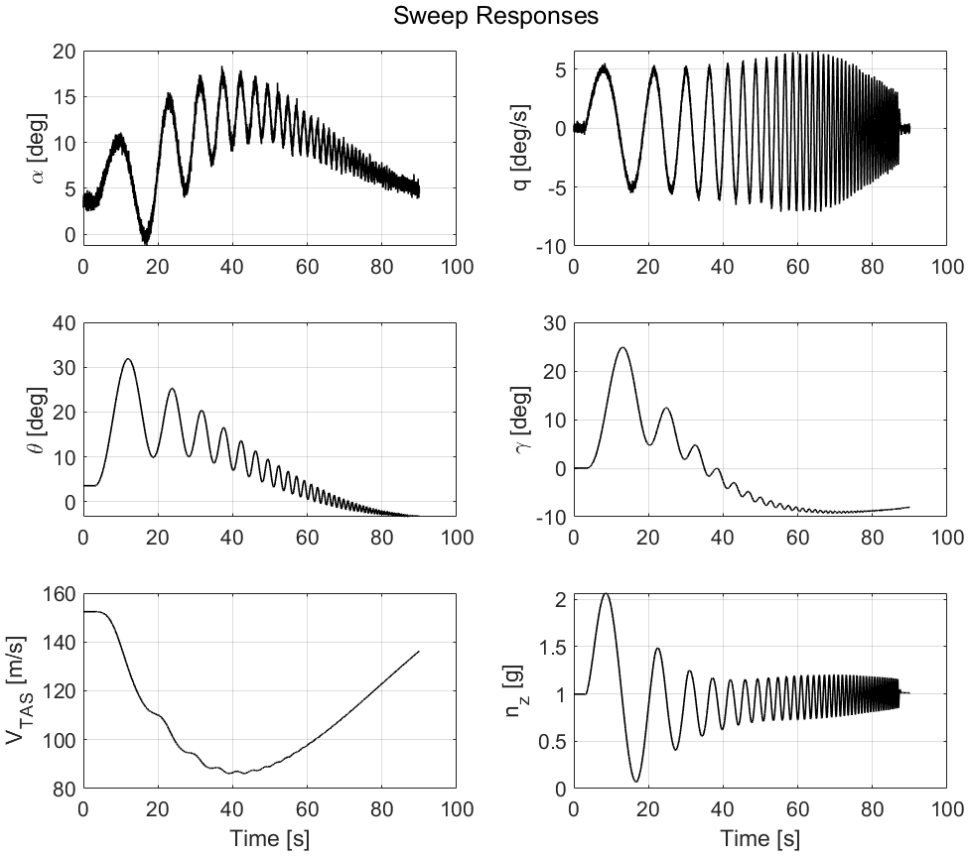

Figure 4.39: Response of Closed-Loop System to Long Sweep Input

The drift is much lower if the input amplitude is like a small perturbation but this is not possible in a real flight-test. As a result, shorter sweep input had to be designed to keep the deviation of airspeed at tolerable amount while keeping pitch rate output amplitude sufficiently high as desired. Grauer and Morelli [46] used the same F-16 model and excited the system with multisine inputs for 25 seconds which yielded an accurate identification. As a response to this work, Tischler et al. [47] also used 25 second of sweep inputs and obtained an excellent model even though the duration of the input is not optimal. The input and output amplitudes and noise levels are similar in both works. These works are taken as a base while designing the shorter sweep input for the closed-loop identification. The record time is limited to 30 seconds, ω_{min} is increased to 0.6 rad/s, and ω_{max} is adjusted to 14 rad/s. The first and last 2 seconds are spent in trim conditions. The pitch rate sweep input q_{ref} and resultant elevator command δ_{ec} are given in Figure 4.40, together with the outputs δ_e, q and α. The rate limit of the actuator is 60 deg/s, and rate saturation is observed at the very last instants at a tolerable amount. Then, as done in all cases, Gaussian white noise with standard deviations of 0.1 deg, 0.2 deg and 0.3 deg/s are added to the δ_e, q and α outputs. The same noise characteristics are used by Grauer and Morelli [46] for the outputs of similar amplitudes.

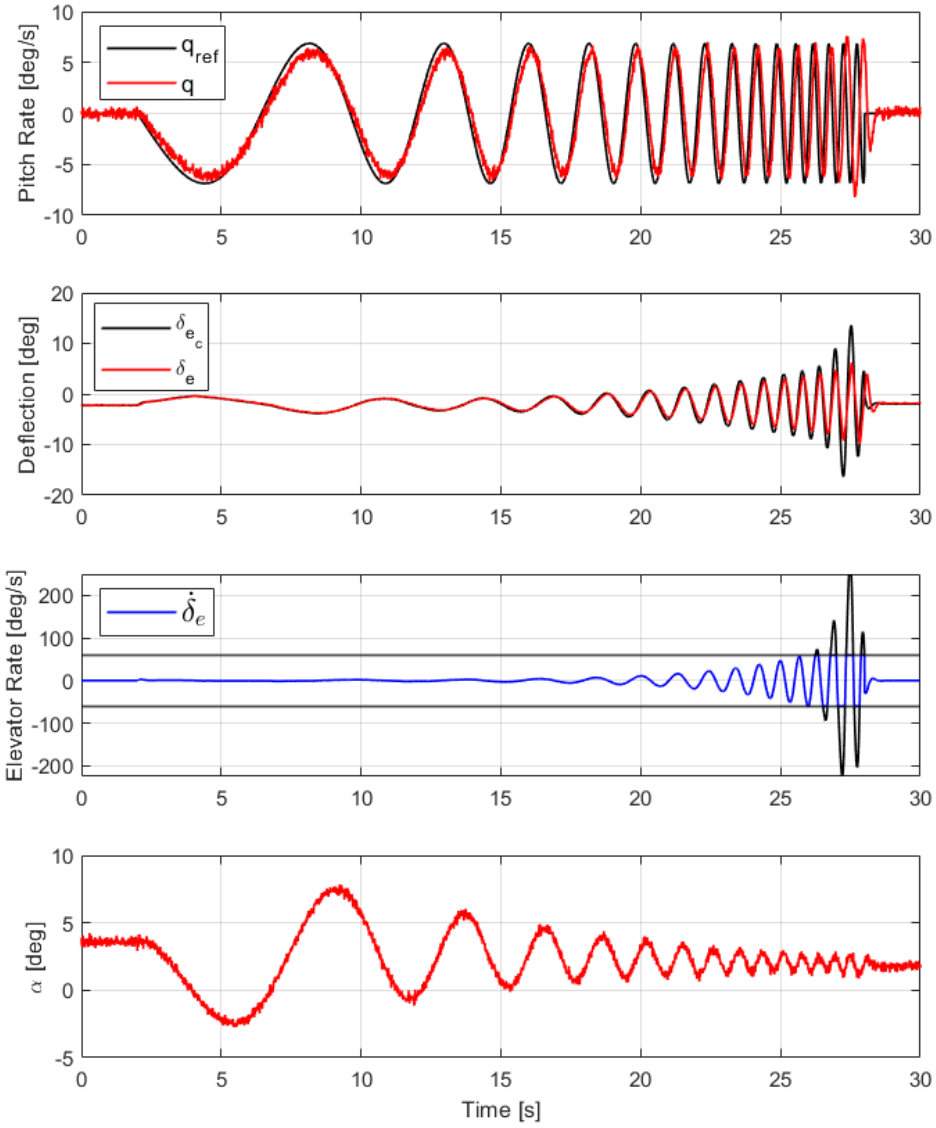

Figure 4.40: Time-Histories for SCAS-on Case

The responses of θ, V_{TAS} and n_z are also presented in Figure 4.41. The variation in airspeed is still considerable, and it will corrupt the quality of identification to some extent but the results showed that it is at a tolerable level.

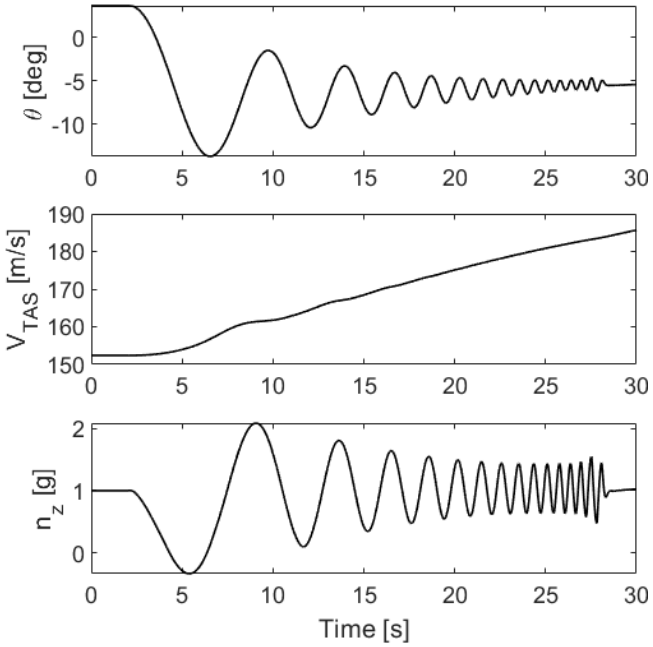

Figure 4.41: Time-Histories of Other Channels for SCAS-on Case

Collecting the time-histories of δ_e, α and q, the data is detrended and windowed as shown previously. The window length is adjusted to 18 seconds as done for the open-loop data. The number of windows for SCAS-on data was remarkably less than open-loop data since the record length is three times lower. This increases the random error because there are fewer points while taking the average. Then, the frequency-responses and coherences are obtained as shown in Figure 4.42. Results obtained from open-loop data from the previous section in Figure 4.7 and the results for the SCAS-on case are plotted together for comparison. Phase plots are very close, but a constant difference in magnitudes is observed. In addition, coherence is lower at the low frequencies for the SCAS-on case than in open-loop data in both channels. The effect is more obvious especially in the pitch-rate coherence plot. There can be two reasons; first, minimum frequency of the sweep input was higher at the closed-loop test and second, it is known that SCAS can supress low-frequency content. Moreover, coherence falls at later frequencies for the SCAS-on case as the maximum frequency of the input sweep used in the closed-loop test was higher than the open-loop sweep.

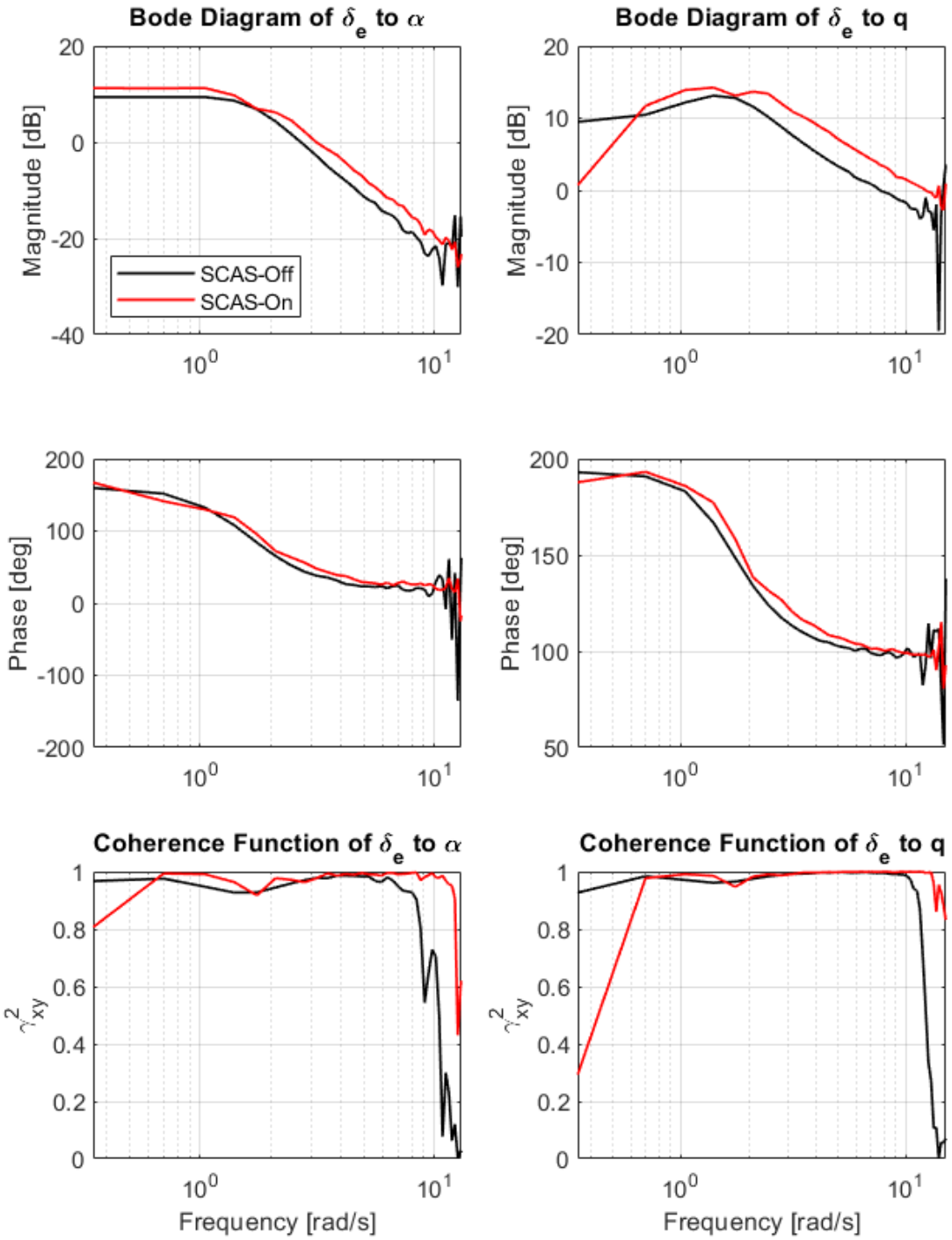

Figure 4.42: Bode Diagrams of the Frequency Responses and Coherences for the SCAS-on Case

The frequency range for the transfer function estimation in Table 4.28 is selected using the coherence plots.

Table 4.28: Frequency Interval with Reliable Coherence for the SCAS-on Case

Frequency Response	ω_{min} [rad/s]	ω_{max} [rad/s]
$\frac{\alpha}{\delta_e}$	0.3491	11.1701
$\frac{q}{\delta_e}$	0.6981	12.9154

The identified transfer functions are:

$$\frac{\alpha}{\delta_e} = \frac{-0.2309s - 11.04}{s^2 + 2.469s + 3.074} \tag{4.39}$$

$$\frac{q}{\delta_e} = \frac{-11.06s - 6.963}{s^2 + 2.469s + 3.074} \tag{4.40}$$

Bode diagrams of identified transfer functions are given together with Bode plots of linear model and the identified model from CIFER using the same closed-loop time-history data in Figure 4.43. Identified model very-well captured the phase at lower frequencies. On the other hand, there is a considerable offset in the mangitude of angle of attack and at high frequencies of pitch-rate Bode plot.

The time-domain comparison of the nonlinear model, linear model and the identified model using SCAS-on data is presented in Figure 4.44.

The identified model is acceptable as J_{rms} values for both channels are under the suggested values. Nonetheless, J_{rms} have increased notably compared to the values of the identified model using SCAS-off data. For the same amount of elevator disturbance, J_{rms} for the α and q channels were 0.11912 and 0.18556, respectively, as shown in Figure 4.11. Since number of windows is reduced, the increase in error is not surprising.

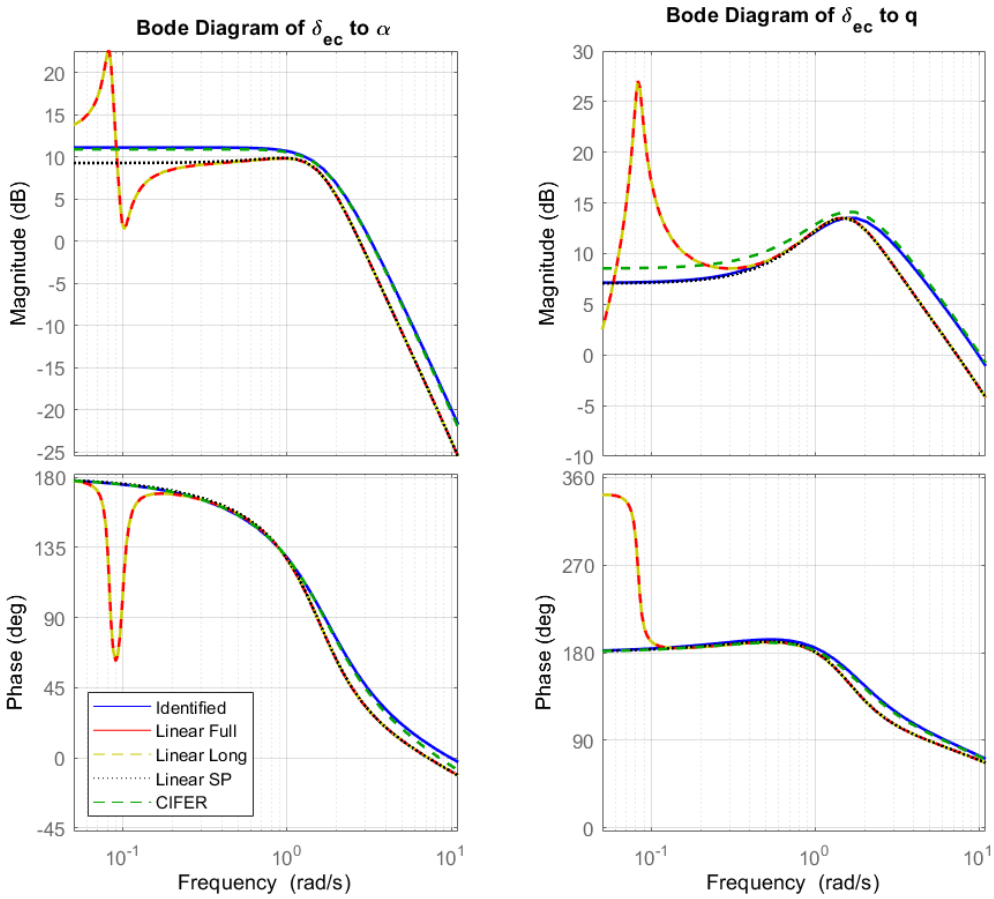

Figure 4.43: Bode Plot Comparison of SCAS-on Case

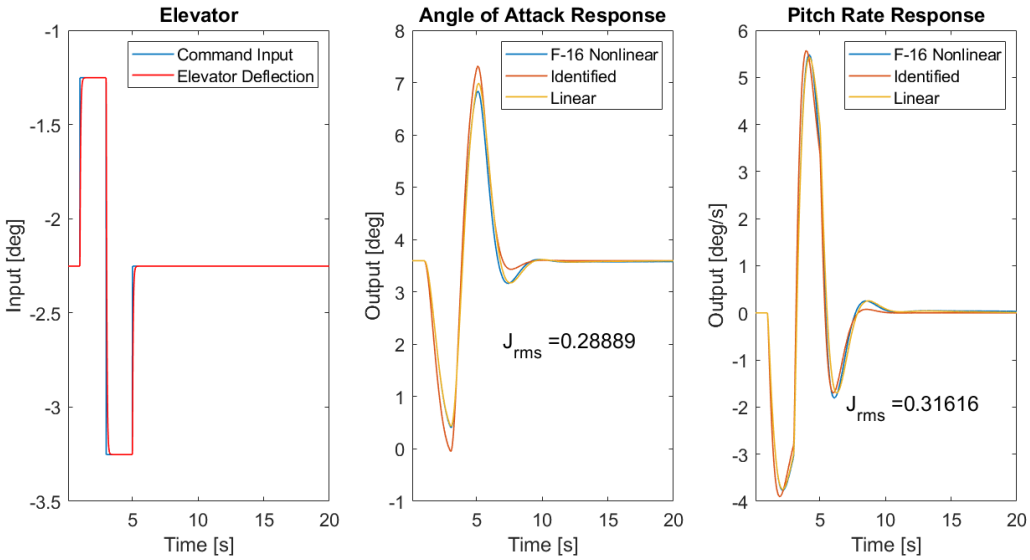

Figure 4.44: Time Domain Verification for SCAS-on Case

The identified values of non-dimensional derivatives are given in Table 4.29, and those of open-loop tested values, polynomial and Linear SP model, which are already presented in the previous section.

Table 4.29: Frequency Interval with Reliable Coherence for SCAS-on Case

Derivative	Open-Loop Data	Polynomial	**Closed-Loop Data**	Linear SP
C_{Z_q}	-30.0793	-32.0092	**-16.9221**	-30.7519
C_{m_q}	-6.5938	-5.4747	**-11.9090**	-6.7978
C_{Z_α}	-3.8068	-3.7248	**-3.2420**	-3.6317
$C_{Z_{\delta_e}}$	-0.8349	-0.4354	**-1.1173**	-0.4405
C_{m_α}	-0.1441	-0.1383	**-0.1457**	-0.1376
$C_{m_{\delta_e}}$	-0.5520	-0.6318	**-0.8287**	-0.5731

The accuracy of all the aerodynamic derivatives of the model identified from SCAS-on data seemed to be lower than the identified model using the open-loop data. The difference is very high, particularly for the pitch-rate damping derivative, which can be related to the constant offset in the magnitude at the pitch-rate Bode plot at mid-frequencies. Previosuly in Equation 4.5, the natural frequency and damping were calculated as 1.6063 rad/s and 0.5560, respectively, and they increased to 1.7533 rad/s and 0.7042. The jump in identified damping ratio is mainly due to the misprediction of the M_q derivative.

The overall performance of the identified model using SCAS-on data is acceptable, but its accuracy is observed to be lower than the identified model using open-loop data.

CHAPTER 5

CONCLUSIONS

The objective of this study was to apply frequency domain system identification techniques, particularly on the F-16 aircraft. Short-period mode identification by using frequency-response estimates of δ_e to α and q of F-16 is performed in this study. Flight-test data is collected from the nonlinear simulation of the aircraft and post-processed. Post-processing applications include detrending and windowing of the time domain data. Then, the processed time domain data is converted to the frequency domain using Fourier transformation by the FFT algorithm. The average of the rough spectrums is calculated across multiple windows, and smooth spectral estimates and frequency responses are obtained. The coherence function is used to determine the proper frequency range, where transfer functions will be estimated for the frequency responses. After performing the transfer function fit, the identified models are tested in the time domain.

Additionally, non-dimensional aerodynamic derivatives from the identified transfer functions are calculated. The open-loop identification results showed that the identified short-period model successfully reflects the nonlinear model's behaviour throughout the envelope. On the other hand, although great results are obtained in the time domain, aerodynamic parameter estimation is not as successful as in the time domain. It is also shown that quantifying phugoid involvement in time histories is difficult as requiring more data at lower frequencies, which was not possible with the current data. Bare-airframe dynamics are also identified from closed-loop data with great accuracy, although it is slightly less accurate than the model identified from open-loop data.

Although accurate results are obtained in this study, enhancements from several aspects are still possible. The main improvements can be the prevention of the aircraft departing from the initial trim condition and the development of a logic that can be used as a guide to predict the parameter estimation accuracy. Even though the time-domain comparison is performed to measure the accuracy of the identified model, another check for the parameter accuracy can be beneficial. Other improvements are also possible. For instance, the Fourier transform can be realised by chirp z-transform, which is expected to increase the frequency-response estimation accuracy further. There can be improvements in the windowing as well. The number of independent windows may increase, and a weighting function to the windows may be introduced while calculating the smooth frequency-response estimates. In addition, the transfer function fitting algorithm may be improved such that certain coefficients can be fixed or user-bounded.

REFERENCES

[1] L. T. Nguyen, *Simulator study of stall/post-stall characteristics of a fighter airplane with relaxed longitudinal static stability*, vol. 12854. National Aeronautics and Space Administration, 1979.

[2] R. S. Russell, "Non-linear f-16 simulation using simulink and matlab," *University of Minnesota, Tech. paper*, 2003.

[3] E. A. Morelli, "Global nonlinear parametric modelling with application to f-16 aerodynamics," in *Proceedings of the 1998 American Control Conference. ACC (IEEE Cat. No. 98CH36207)*, vol. 2, pp. 997–1001, IEEE, 1998.

[4] R. V. Jategaonkar, *Flight vehicle system identification: a time domain methodology*. American Institute of Aeronautics and Astronautics, 2006.

[5] S. R. Kulkarni, "Frequency domain and fourier transforms - princeton university," 1999.

[6] Siemens, "Window types: Hanning, flattop, uniform, tukey, and exponential," 2019.

[7] M. A. Kramer and U. T. Eden, *Case studies in neural data analysis: a guide for the practicing neuroscientist*. MIT Press, 2016.

[8] Siemens, "Windows and spectral leakage," 2019.

[9] M. Trethewey, "Window and overlap processing effects on power estimates from spectra," *Mechanical Systems and Signal Processing*, vol. 14, no. 2, pp. 267–278, 2000.

[10] W. Liu, *Introduction to hybrid vehicle system modeling and control*. John Wiley & Sons, 2013.

[11] L. Ljung, "Perspectives on system identification," *Annual Reviews in Control*, vol. 34, no. 1, pp. 1–12, 2010.

[12] E. A. Morelli and V. Klein, *Aircraft system identification: theory and practice*, vol. 2. Sunflyte Enterprises Williamsburg, VA, 2016.

[13] M. Mohamed, "Parameter identification of flexible aircraft using frequency domain output error approach," *IFAC Proceedings Volumes*, vol. 47, no. 1, pp. 1166–1171, 2014.

[14] E. A. Morelli and J. A. Grauer, "Practical aspects of frequency-domain approaches for aircraft system identification," *Journal of Aircraft*, vol. 57, no. 2, pp. 268–291, 2020.

[15] J. Schoukens, R. Pintelon, and Y. Rolain, "Time domain identification, frequency domain identification. equivalencies! differences?," in *Proceedings of the 2004 American Control Conference*, vol. 1, pp. 661–666, IEEE, 2004.

[16] J. Antoni and J. Schoukens, "Optimal settings for measuring frequency response functions with weighted overlapped segment averaging," *IEEE transactions on instrumentation and measurement*, vol. 58, no. 9, pp. 3276–3287, 2009.

[17] M. B. Tischler and R. K. Remple, *Aircraft and rotorcraft system identification*. American Institute of Aeronautics and Astronautics Reston, VA, 2012.

[18] P. Young and R. J. Patton, "Comparison of test signals for aircraft frequency domain identification," *Journal of Guidance, Control, and Dynamics*, vol. 13, no. 3, pp. 430–438, 1990.

[19] V. Klein, "Aircraft parameter estimation in frequency domain," in *4th Atmospheric Flight Mechanics Conference*, p. 1344, 1978.

[20] J. A. Grauer and M. J. Boucher, "Identification of aeroelastic models for the x-56a longitudinal dynamics using multisine inputs and output error in the frequency domain," *Aerospace*, vol. 6, no. 2, p. 24, 2019.

[21] E. A. Morelli, "Identification of low order equivalent system models from flight test data," tech. rep., 2000.

[22] J. A. Grauer and M. J. Boucher, "Aircraft system identification from multisine inputs and frequency responses," *Journal of Guidance, Control, and Dynamics*, vol. 43, no. 12, pp. 2391–2398, 2020.

[23] W. F. Milliken Jr, "Progress in dynamic stability and control research," *Journal of the Aeronautical Sciences*, vol. 14, no. 9, pp. 493–519, 1947.

[24] H. Greenberg, "A survey of methods for determining stability parameters of an airplane from dynamic flight measurements," tech. rep., 1951.

[25] M. Shinbrot, *A least squares curve fitting method with applications to the calculation of stability coefficients from transient-response data*. No. 2341, National Advisory Committee for Aeronautics, 1951.

[26] L. Ljung and K. Glover, "Frequency domain versus time domain methods in system identification," *Automatica*, vol. 17, no. 1, pp. 71–86, 1981.

[27] K.-J. Åström and B. Torsten, "Numerical identification of linear dynamic systems from normal operating records," *IFAC Proceedings Volumes*, vol. 2, no. 2, pp. 96–111, 1965.

[28] V. Klein, "Maximum likelihood method for estimating airplane stability and control parameters from flight data in frequency domain," tech. rep., 1980.

[29] J. Kaletka and K.-H. Fu, "Frequency-domain identification of unstable systems using x-31a aircraft flight test data," in *Flight Simulation and Technologies*, p. 3635, 1993.

[30] C. Sanathanan and J. Koerner, "Transfer function synthesis as a ratio of two complex polynomials," *IEEE transactions on automatic control*, vol. 8, no. 1, pp. 56–58, 1963.

[31] T. R. Twisdale and T. A. Ashurst Jr, "System identification from tracking (sift), a new technique for handling-qualities test and evaluation," *initial report), AFFTC-TR-77-27*, 1977.

[32] R. H. Hoh, D. G. Mitchell, I. L. Ashkenas, R. H. Klein, and R. K. Heffley, "Proposed mil standard and handbook-flying qualities of air vehicles. volume 2. proposed mil handbook," tech. rep., SYSTEMS TECHNOLOGY INC HAWTHORNE CA, 1982.

[33] L. Ljung, "Frequency domain versus time domain methods in system

identification–revisited," in *Control of Uncertain Systems: Modelling, Approximation, and Design*, pp. 277–291, Springer, 2006.

[34] A. Dorobantu, A. Murch, B. Mettler, and G. Balas, "System identification for small, low-cost, fixed-wing unmanned aircraft," *Journal of Aircraft*, vol. 50, no. 4, pp. 1117–1130, 2013.

[35] M. Mohajerani, *Frequency-Domain System Identification for Unmanned Helicopters from Flight Data*. PhD thesis, Concordia University, 2014.

[36] B. L. Stevens, F. L. Lewis, and E. N. Johnson, *Aircraft control and simulation: dynamics, controls design, and autonomous systems*. John Wiley & Sons, 2015.

[37] K. Ogata *et al.*, *Modern control engineering*, vol. 5. Prentice hall Upper Saddle River, NJ, 2010.

[38] F. J. Harris, "On the use of windows for harmonic analysis with the discrete fourier transform," *Proceedings of the IEEE*, vol. 66, no. 1, pp. 51–83, 1978.

[39] J. S. Bendat and A. G. Piersol, *Random data: analysis and measurement procedures*, vol. 729. John Wiley & Sons, 2011.

[40] H. A. Gaberson, "A comprehensive windows tutorial," *Sound and Vibration*, vol. 40, no. 3, pp. 14–23, 2006.

[41] A. A. Ozdemir and S. Gumussoy, "Transfer function estimation in system identification toolbox via vector fitting," *IFAC-PapersOnLine*, vol. 50, no. 1, pp. 6232–6237, 2017.

[42] MathWorks, "tfest."

[43] T. Berger, M. B. Tischler, S. G. Hagerott, M. Christopher Cotting, and W. R. Gray, "Identification of a full-envelope learjet-25 simulation model using a stitching architecture," *Journal of Guidance, Control, and Dynamics*, vol. 43, no. 11, pp. 2091–2111, 2020.

[44] M. Knapp, T. Berger, M. Tischler, M. Cotting, and A. Marcus, "Development of a full flight envelope f-16 vista simulation model from closed-loop flight data," *AIAA Paper*, vol. 525, p. 2018, 2018.

[45] J. Roskam, *Airplane flight dynamics and automatic flight controls*. DARcorporation, 1995.

[46] J. Grauer and E. Morelli, "Method for real-time frequency response and uncertainty estimation," *Journal of Guidance, Control, and Dynamics*, vol. 37, no. 1, pp. 336–344, 2014.

[47] M. B. Tischler, C. M. Ivler, and T. Berger, "Comment on "method for real-time frequency response and uncertainty estimation"," *Journal of Guidance, Control, and Dynamics*, vol. 38, no. 3, pp. 547–549, 2015.